AD-A014 649

CW PIN DISCHARGE LASER

WESTINGHOUSE RESEARCH LABORATORIES

PREPARED FOR
OFFICE OF NAVAL RESEARCH
ADVANCED RESEARCH PROJECTS AGENCY
DEFENSE CONTRACT ADMINISTRATION SERVICES DISTRICT

30 NOVEMBER 1974

CW PIN DISCHARGE LASER

Final Technical Report
November 30, 1974

Authors: S. A. Wutzke, L. H. Taylor,
J. L. Pack, T. V. George and
L. A. Weaver

Westinghouse Research Laboratories
PITTSBURGH, PENNSYLVANIA 15235

ARPA Order No. 1806
Program Code No. 3E90
Title: CW PIN DISCHARGE LASER
Name of Contractor: Westinghouse Research Laboratories
Amount of Contract: $249,975
Date of Report: 30 November 1974
Contract No.: N00014-73-C-0318
Effective Date of Contract: 15 March 1973
Contract Expiration Date: 30 September 1974
Principal Investigator: S. A. Wutzke
Phone No.: (412) 256-3252

Scientific Officer: Director, Physics Program
           Physical Sciences Division
           Office of Naval Research
           Department of Navy
           800 North Quincy Street
           Arlington, Virginia 22217

The views and conclusions contained in this document are those of the
authors and should not be interpreted as necessarily representing the
official policies, either expressed or implied, of the Advanced Research
Projects Agency or the U. S. Government.

SECURITY CLASSIFICATION OF THIS PAGE *(When Data Entered)*

REPORT DOCUMENTATION PAGE		READ INSTRUCTIONS BEFORE COMPLETING FORM
1. REPORT NUMBER None	2. GOVT ACCESSION NO.	3. RECIPIENT'S CATALOG NUMBER
4. TITLE *(and Subtitle)* CW PIN DISCHARGE LASER		5. TYPE OF REPORT & PERIOD COVERED Final Technical Report 15 March 73 - 30 Sept. 74
		6. PERFORMING ORG. REPORT NUMBER
7. AUTHOR(s) S. A. Wutzke, L. H. Taylor, J. L. Pack, T. V. George and L. A. Weaver		8. CONTRACT OR GRANT NUMBER(s) N00014-73-C-0318
9. PERFORMING ORGANIZATION NAME AND ADDRESS Westinghouse Electric Corporation Research Laboratories Pittsburgh, Pennsylvania 15235		10. PROGRAM ELEMENT, PROJECT, TASK AREA & WORK UNIT NUMBERS Program Code 3E90
11. CONTROLLING OFFICE NAME AND ADDRESS Procuring Contracting Officer Office of Naval Research Department of the Navy Arlington, Va. 22217		12. REPORT DATE November 30, 1974
		13. NUMBER OF PAGES 133
14. MONITORING AGENCY NAME & ADDRESS*(if different from Controlling Office)* Commander, Defense Contract Administration Services District 1610 S. Federal Bldg., 1000 Liberty Avenue Pittsburgh, Pa. 15222		15. SECURITY CLASS. *(of this report)* UNCLASSIFIED
		15a. DECLASSIFICATION/DOWNGRADING SCHEDULE NA

16. DISTRIBUTION STATEMENT *(of this Report)*

ONR Distribution List Attached

17. DISTRIBUTION STATEMENT *(of the abstract entered in Block 20, if different from Report)*

18. SUPPLEMENTARY NOTES

ARPA Order No. 1806, Amed. #9, dtd. 11-15-72

19. KEY WORDS *(Continue on reverse side if necessary and identify by block number)*

lasers, glow, scaling, breakdown, discharges, sparks, pins, kinetics

20. ABSTRACT *(Continue on reverse side if necessary and identify by block number)*

A Continuously Operating Fast Flow Electrically Excited (COFFEE) laser excitation concept was studied to determine the feasibility of scaling it to high-power levels. The concept uses a multipin-to-plane electrode configuration with transverse flow to produce a high-pressure self-sustained glow discharge. Simultaneous approaches involving both experimental measurements and theoretical analyses were employed to develop discharge scaling criteria and a laser kinetics model. The results demonstrate that the COFFEE

DD FORM 1473 1 JAN 73   EDITION OF 1 NOV 65 IS OBSOLETE.

1. SECURITY CLASSIFICATION OF THIS PAGE *(When Data Entered)*

laser is scalable to high-power levels and, in addition, exhibits many useful and unique features.

ia

TABLE OF CONTENTS

SUMMARY

A Continuously Operating Fast Flow Electrically Excited
(COFFEE) laser excitation concept was studied to determine the feasibility
of scaling it to high-power levels. The concept uses a multipin-to-plane
electrode configuration with transverse flow to produce a high-pressure,
self-sustained glow discharge. Simultaneous approaches involving both
experimental measurements and theoretical analyses were employed to
develop discharge scaling criteria and a laser kinetics model. The
results demonstrate that the COFFEE laser is scalable to high-power levels
and, in addition, exhibits many useful and unique features.

Experimental measurements were made of the glow behavior using
an electrode module (10 x 10 x 10 cm). Parametric studies determined the
influences of discharge current, gas velocity, pressure, mixture, electrode
gap, and cathode pin spacing on input power density, specific input energy,
discharge stability, and scale size. Measurements of the small-signal
gain distributions were also made for a number of parameter settings.
In addition the kinetic gas temperature was inferred from measurements
of the small-signal gain taken at various P and R-branch laser wavelengths.
The results included observations of specific input energies up to 140 kJ/lb
with input power densities up to 50 W/cm^3 of discharge volume. Maximum
input power was obtained at $\sim$300 Torr for a number of different operating
conditions. With an 8 cm gap a typical small-signal gain of 0.25%/cm
was obtained at 30 W/cm^3 input power and 150 m/sec gas velocity. The
corresponding gas mixture was $1CO_2:7N_2:20He:0.2H_2$ at 280 Torr. These
results were compared with the theoretical predictions of a glow discharge
model and a laser kinetics model.

The glow discharge was modeled by calculating the steady state
balance between electron generation and loss mechanisms under self-sustained
operating conditions. This model predicted the operating E/N in the

ic

upstream portion of the discharge to within 10% if one assumed that the electron loss rate is attachment dominated.

The laser kinetics were analyzed using a computer code developed for a six-temperature Boltzmann equilibrium model of $CO_2:N_2:He:H_2O$ gas mixtures. The model is quite general and can be applied to most CO_2 flowing gas laser systems of present interest. Gas temperature and E/N dependencies were included, along with all important sources of gas heating. Computer predictions of the small-signal gain distribution along the gas flow direction agree well with the measured values. Laser cavity optics were also included in the model, and parametric calculations were performed for various output couplings and operating pressures. An output power of 45 kW at an efficiency of 15% was predicted from an 8 x 11 x 140 cm cavity operating at 280 Torr.

The main conclusion of these studies is that multikilowatt COFFEE laser systems can easily be built and a solid technology base now exists for designing these systems.

1. INTRODUCTION

The approach in this study program is based on the use of a Continuously Operating Fast Flow Electrically Excited (COFFEE) laser concept. The COFFEE laser uses a new high-pressure (0.1 to 1 atm) direct current self-sustained glow discharge excitation scheme which is well suited for a continuous wave CO_2 laser. The continuous glow is produced with a multipin-to-plane electrode geometry and is stabilized by a gas flow transverse to the discharge and by a ballast resistor in series with each cathode pin. The excitation concept is illustrated in Fig. 1:1. A high-power CO_2 laser system using this excitation scheme would be relatively simple, rugged, compact, and inexpensive.

The objective of the program described herein has been the development of the high-pressure glow discharge scaling criteria for the multipin-to-plane electrode system. Particular emphasis has been placed on understanding the physics of the discharge as they relate to discharge scalability and laser excitation efficiency. Parallel, complementary approaches involving both experimental studies and theoretical modeling were pursued. Specific tasks included glow discharge experiments using an electrode module (10 x 10 x 10 cm) to measure the important glow discharge parameters. This module was constructed during Phase I of this study program as described earlier.[1] The results for Phase II, which was a continuation of the studies, are reported in Section 2 of this report. Small-signal gain measurements are also described. Section 3 contains the theoretical modeling developed to gain further understanding of the discharge characteristics and laser kinetics. Preparatory work for an envisioned Phase III to build a 25 kW proof of scalability laser is described in Section 4. Finally, Section 5 is devoted to suggestions for further work.
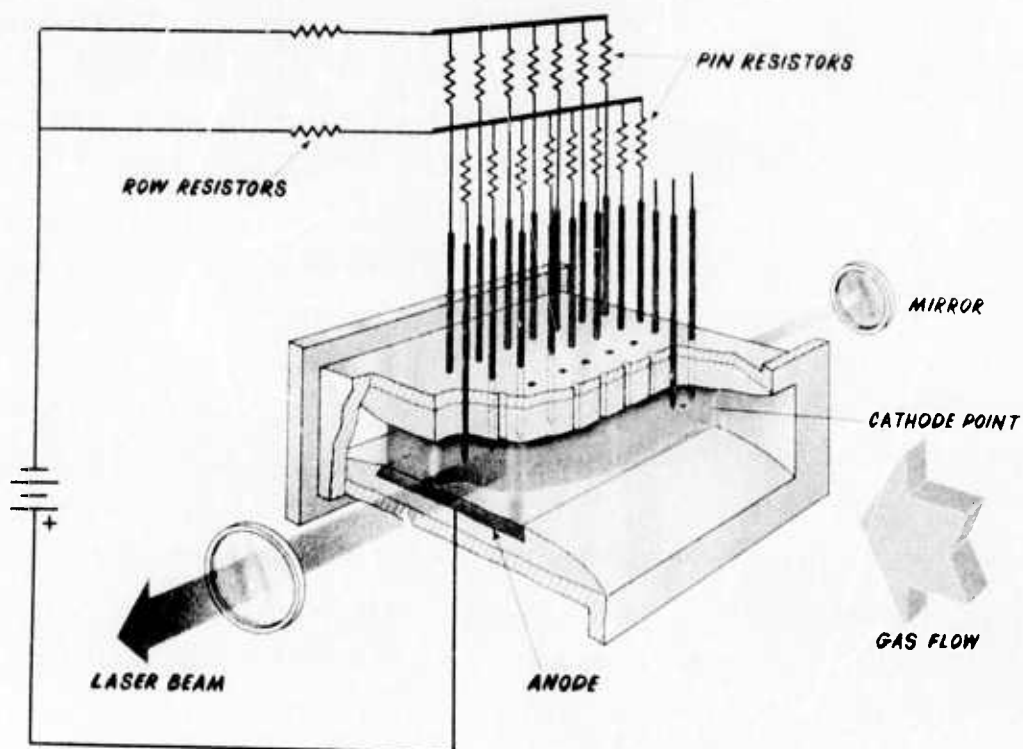
Fig. 1:1 Artist's conception of COFFEE laser.

2. GLOW DISCHARGE EXPERIMENTS

2.1 DESCRIPTION OF GLOW DISCHARGE SCHEME

The COFFEE laser concept uses a continuous, self-sustained glow discharge which is produced with a multipin-to-plane electrode geometry as shown in Fig. 1:1. The glow is stabilized at high pressures by a gas flow transverse to the discharge and by a ballast resistor in series with each cathode pin. Additional row ballast resistors are used to tailor the input power distribution as a function of downstream distance.

As part of the COFFEE laser study program, an electrode module (10 x 10 x 10 cm) was tested to determine the glow discharge scalability as a function of the important parameters. One purpose of the module experiments was to demonstrate that indeed it is feasible to build a large-scale laser device. In addition, parametric studies were made to determine the influence of the main parameters, such as discharge current, gas velocity, pressure, mixture, electrode gap, and cathode pin spacing. Small-signal gain measurements were made as a function of these variables to determine the uniformity and efficiency of the excitation. These experiments have also provided important information for the theoretical models of the glow discharge and laser kinetics.

The discharge module formed a two-dimensional flow nozzle (subsonic) which consisted of a planar anode on one side and a sheet of high-temperature dielectric on the other side. The two electrodes assemblies are shown in Figs. 2:1 and 2:2. The cathode consisted of a multipin array (110 pins) protruding approximately 0.6 cm through the insulating sheet with a pin density of 1 pin/cm^2. Looking along the 10 cm optical axis, transverse to the flow, one saw 11 rows of 10 pins. Each pin in a given row was connected through a separate 50 kΩ ballast resistor to a common row bus bar. As the laser gas mixture passes from row to row, the discharge impedance decreases due to gas heating. This was compensated in the present case by
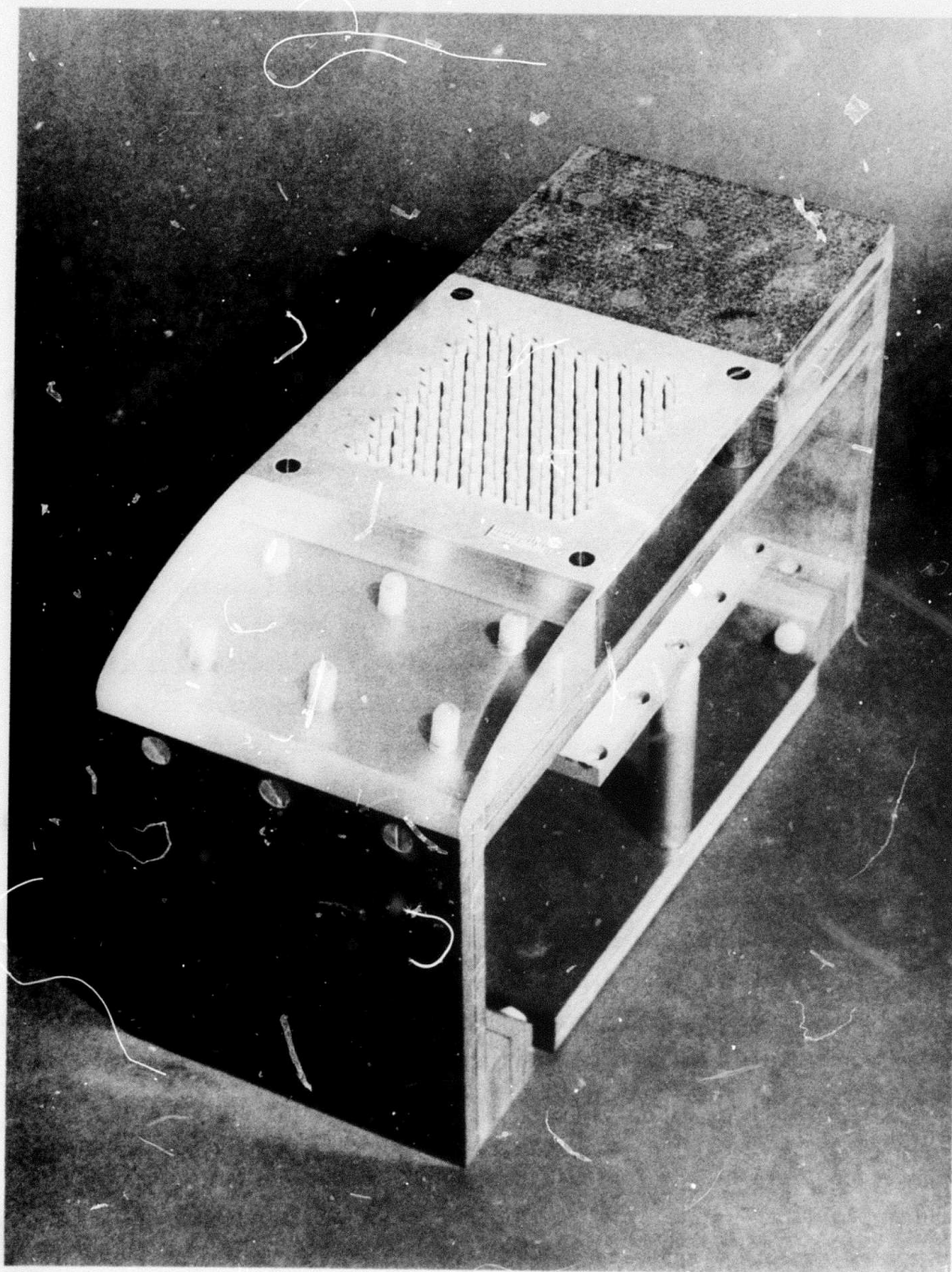
3

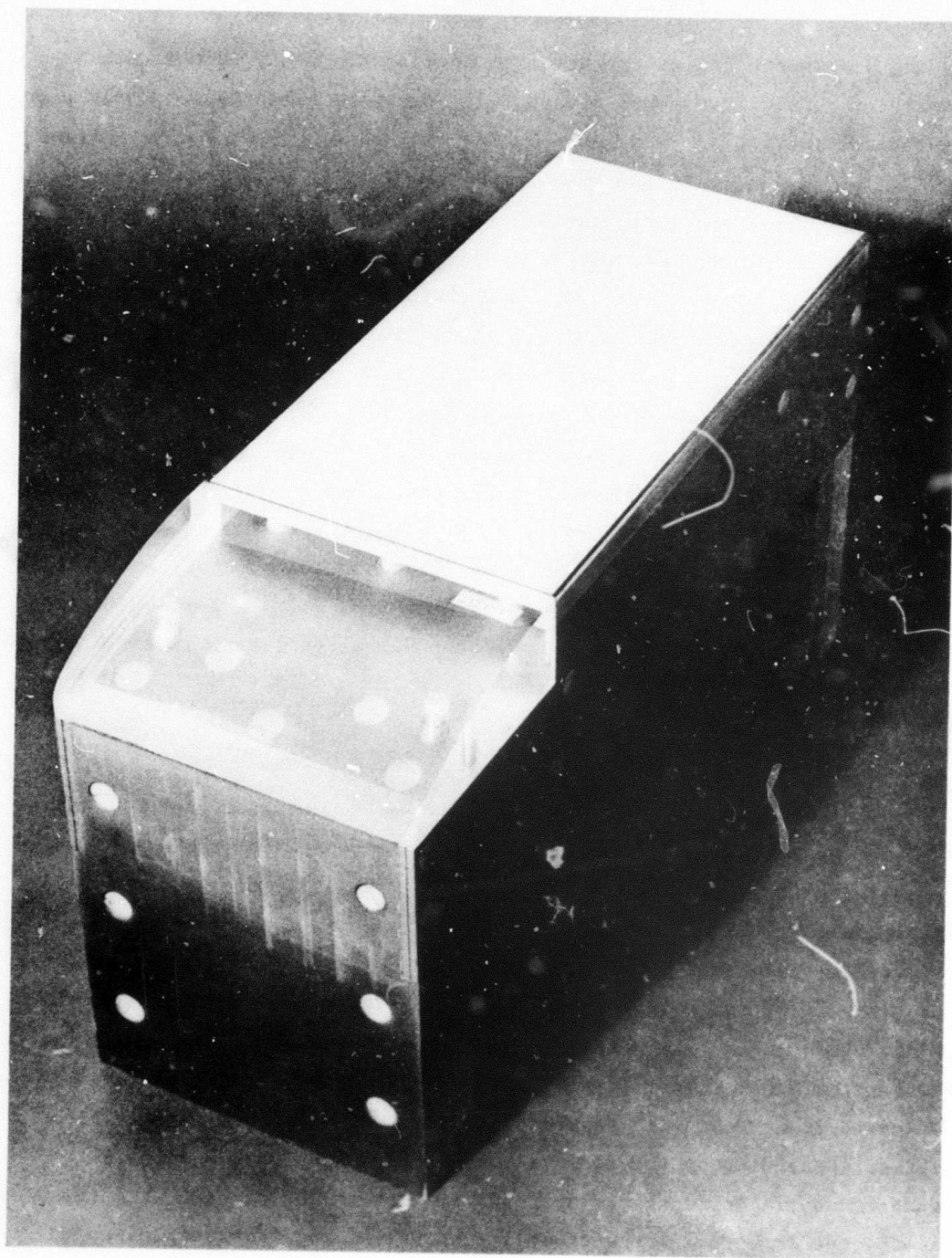Fig. 2:1 Multipin cathode assembly.

4

Fig. 2:2 Anode assembly.

5

adding a separate ballast resistor to each row in order to maintain a nearly constant input power density. A diverging flow channel could also have been used.

The electrode gap was varied from 2 to 10 cm. The distance between the first and last rows of cathode pins in the gas flow direction was 10 cm. Alternate rows were staggered so that the nearest pin in the gas flow direction was 2 cm away, minimizing the discharge interactions at the cathode. Tungsten pins with a 1 mm diameter and a sharp conical tip were used. The copper anode was 15 cm wide and approximately 30 cm long. An internally metalized glass tube was fitted around the perimeter of the anode (not shown) to act as guard ring for minimizing the field enhancement of the anode edges at large electrode spacings. The internal metal surface of this tube was connected electrically to the downstream end of the anode. The electrodes were fitted into a special vacuum-tight fiberglass test section housing as shown in Fig. 2:3. This test section was part of a closed-loop wind tunnel capable of operating at any pressure up to 1 atm with variable flow rates up to 170 m^3/min.

2.2 ELECTRODE MODULE (10 x 10 x 10 cm) PARAMETERIZATION

The high-pressure direct current self-sustained glow discharge has been successfully scaled to a 10 x 10 cm square aperture. A photograph of the glow discharge is shown in Fig. 2:4. Visually the glow appeared fairly uniform, although no direct correlation was found between the measured small-signal gain and the luminosity. The glow was less visible under the first two rows because the current to these rows was less than to the other rows. The upstream rows acted to "condition" or preionize the gas for the other rows. In addition, the glow discharge appeared to be deflected downstream with respect to the cathode by approximately 15-30 degrees, depending on the flow velocity. (See Section 2.3 on gain measurements). For spacings up to 10 cm there was no problem with the glow blowing out or becoming positionally unstable for gas velocities up to 150 m/sec. The discharge luminosity was observed to decrease again under the most downstream rows where the current density was the highest. This may be due to a slightly lower operating E/N, ratio of electric field
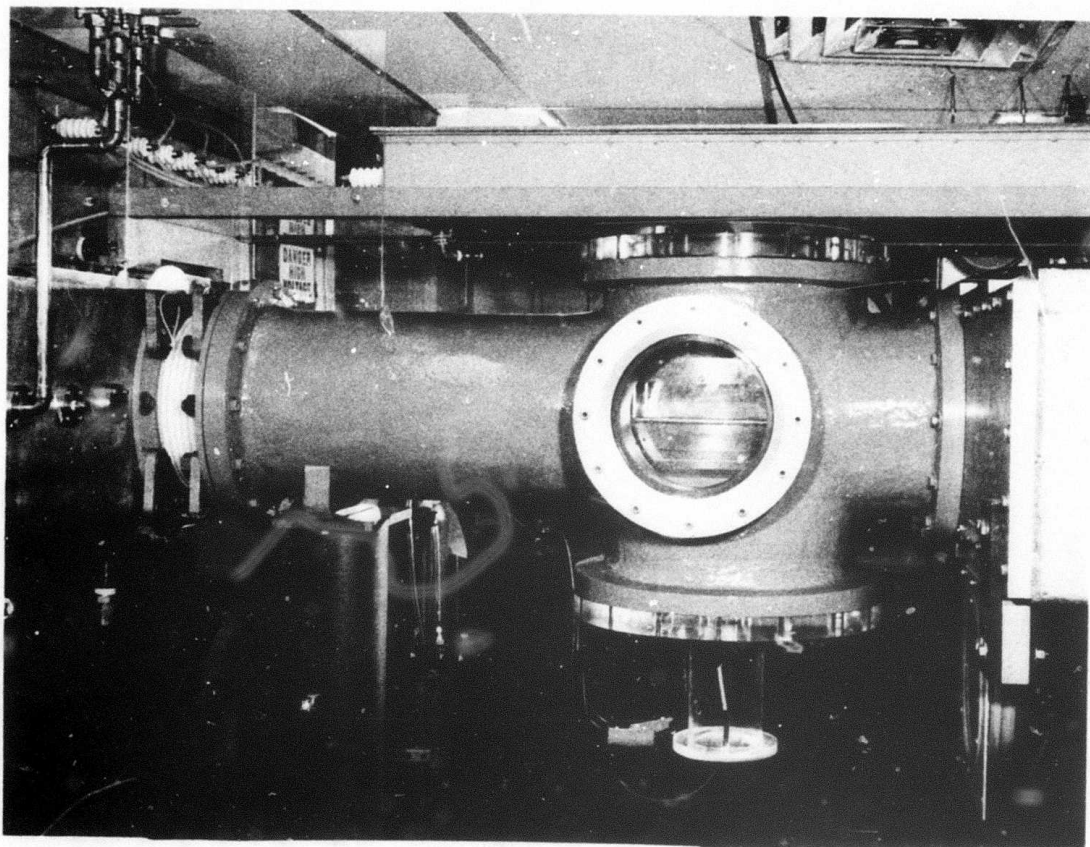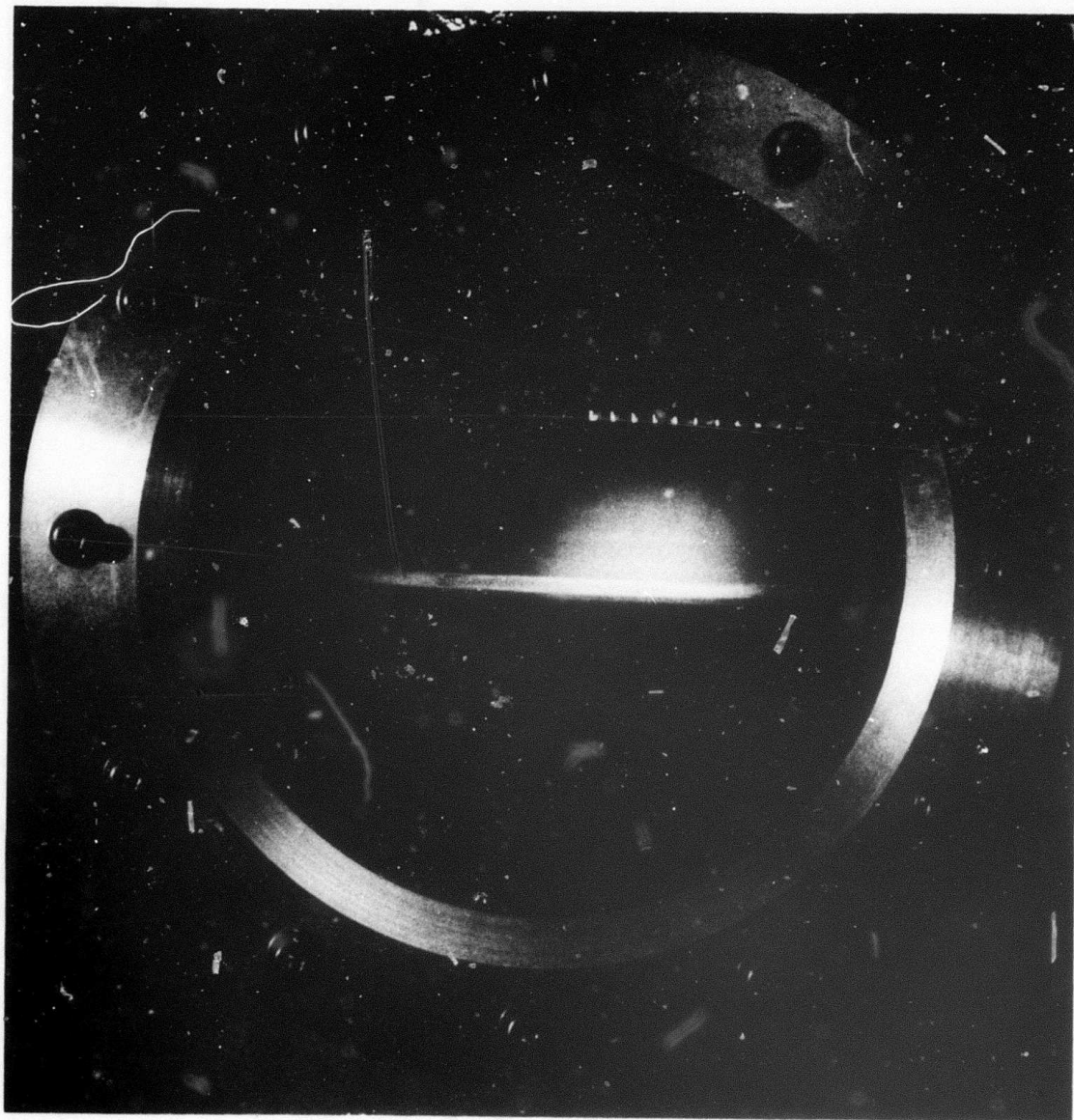
6

Fig. 2:3 Fiberglass test section housing with anode and
cathode assemblies installed.

← Flow 150 m/sec

Fig. 2:4   High-pressure DC glow discharge viewed along
optical axis of 10 x 10 x 10 cm module.   140 Torr;
$1CO_2:7N_2:20He$.

strength to gas density, in this region as described in detail in Section 3.2. Since the mechanisms which produce luminosity are different from those which produce laser gain, one should not expect an exact correlation between them.

Average input power densities up to 50 W/cm^3 of discharge volume were obtained with specific input energies up to 140 kJ/lb ($\sim$150 J/ℓ-atm). At large gaps, however, somewhat lower values were obtained. For example, with an 8 cm discharge gap, we obtained 30 W/cm^3 uniformly, except for the first two cathode rows, at 50 kJ/lb using a $1CO_2$:$7N_2$:$20He$ gas mixture at 286 Torr and 150 m/sec flow velocity. This result is shown in Fig. 2:5 for row ballast resistor configuration #1. The input power distribution can easily be varied over a wide range as demonstrated by the results for row ballast configuration #2. Both examples in Fig. 2:5 corresponded to operating conditions just below the glow-to-arc threshold, and the total input power turned out to be nearly the same in both cases. Therefore, no attempt was made to optimize the row ballast configuration for each test condition during the discharge parameterization studies. Rather, a near optimum configuration for uniform input power density at maximum total input power was chosen and then held constant during each specific test.

The influence of gas velocity on the maximum average input power density is illustrated in Fig. 2:6 for a typical set of operating conditions. In general, the higher velocities tend to inhibit the propagation of discharge streamers across the gap and, thereby, prevent the onset of arcing. The reason for the nearly linear dependence is poorly understood at this time. As described previously,[1] the glow-to-arc transition appears to be due to local thermal instabilities in the discharge rather than bulk thermal effects. Numerous investigators[2-4] have studied the phenomena and have concluded that the instability threshold appears to be related to many factors, such as gas residence time, input power density, gas turbulence level, and local field perturbations. However, the present theories are mainly qualitative and can only predict general trends. Much additional work is needed in this area. Since the highest performance was desired, most of the other
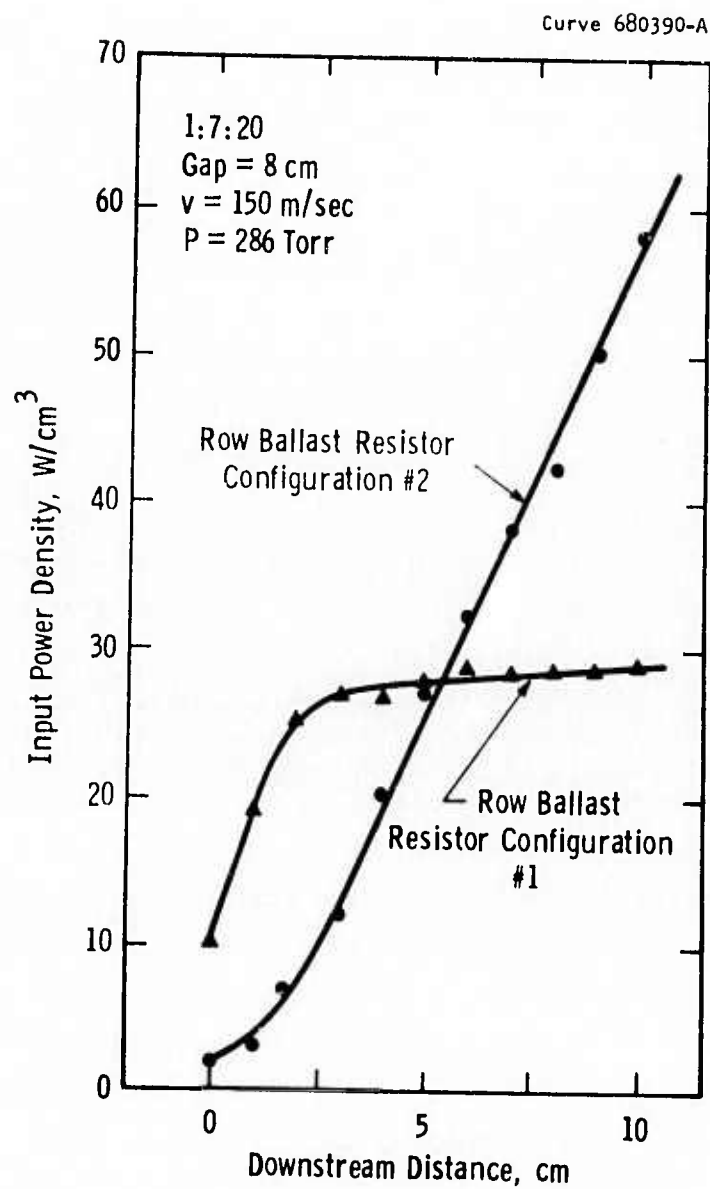
9

Fig. 2:5 Variation of input power density with downstream distance in the discharge for two row ballast resistor configurations.
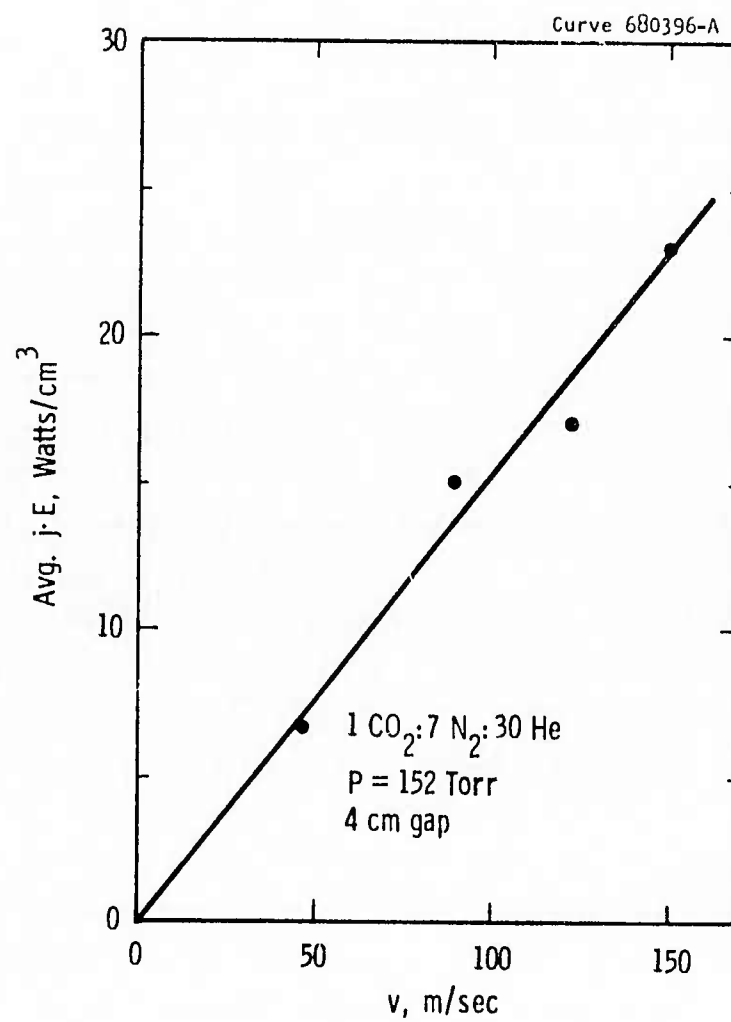
Curve 680396-A

Fig. 2:6 Average input power density versus entering gas
flow velocity.

11

parameterizations were done with ∿150 m/sec flow velocity which was the maximum achievable with the pressure head capability of our blower.

Figure 2:7 shows the maximum total input power to the discharge module that was obtained without arcing as a function of discharge gap for two operating pressures. The solid curves are straight line approximations of the experimental data. Higher input powers were obtained with the larger gaps. The scalability is further indicated by replotting this data in terms of the average input power density as shown in Fig. 2:8. The input power density was calculated on the basis of dividing the total input power by the discharge current area of 1 cm^2 per pin times 110 pins (from the cathode pin density) and the discharge gap (2 to 10 cm). The solid curve is a cross-plot of the straight line from Fig. 2:7. If the maximum input power increased linearly with gap, the maximum input power density would be independent of the discharge gap, which is a desirable scaling relationship. At larger gaps (5-10 cm) we see that the maximum input power density was fairly insensitive to gap. At small gaps (∿2 cm), however, it was possible to achieve almost double the input power density. The explanation for this behavior is rooted in the discharge instability phenomena. The discharges between real small gaps are probably more stable because the component of the electric field which presumably exists in the gas flow direction is considerably smaller in this situation. Nevertheless, the results of Fig. 2:7 indicate that gaps greater than 10 cm would be useful for obtaining even greater power levels.

The effect of gas pressure is shown most clearly in Fig. 2:9. The average input power densities were observed to increase linearly with discharge current for any given operating pressure as expected, because the V I characteristic for this glow discharge is nearly flat (slightly rising). For any given current setting the input power density is approximately proportional to the total gas pressure if the gas mixture is held constant. This occurs because the operating E/N for the discharge is to first order governed only by the gas mixture. The dashed curve in Fig. 2:9 represents the glow-to-arc limit on input power

12

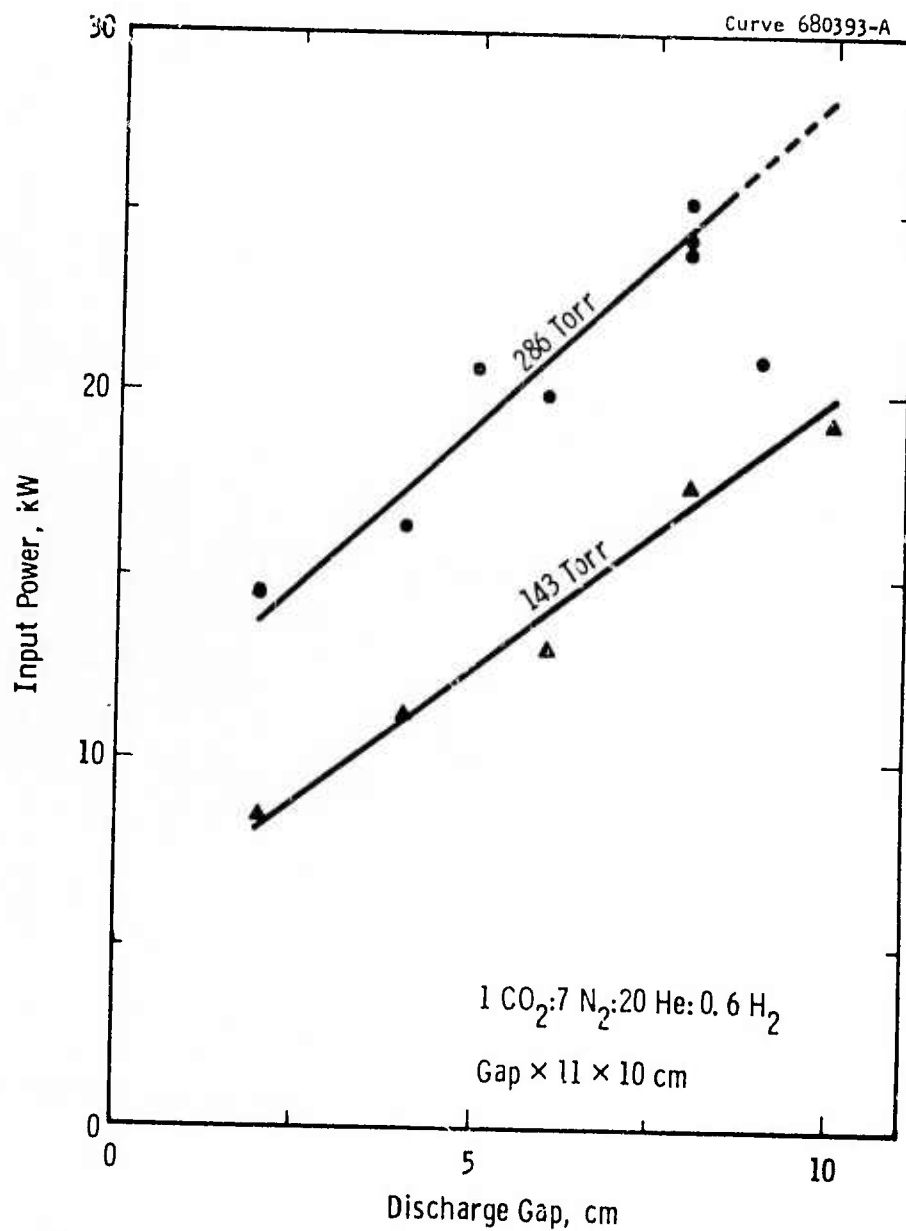1 CO_2:7 N_2:20 He: 0.6 H_2

Gap × 11 × 10 cm

Fig. 2:7 Maximum input power with stable discharge versus discharge gap.
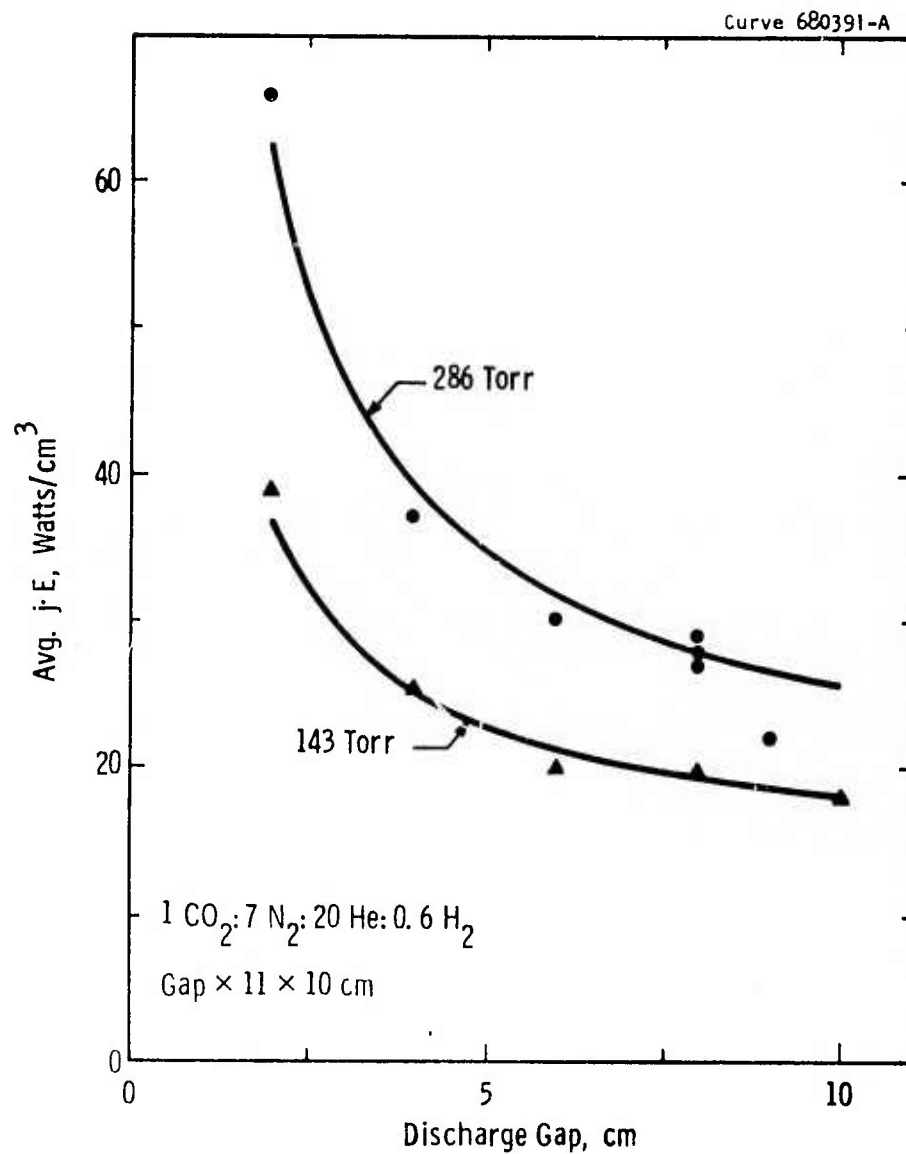
13

Curve 680391-A

Fig. 2:8 Maximum average input power density with stable discharge versus discharge gap.
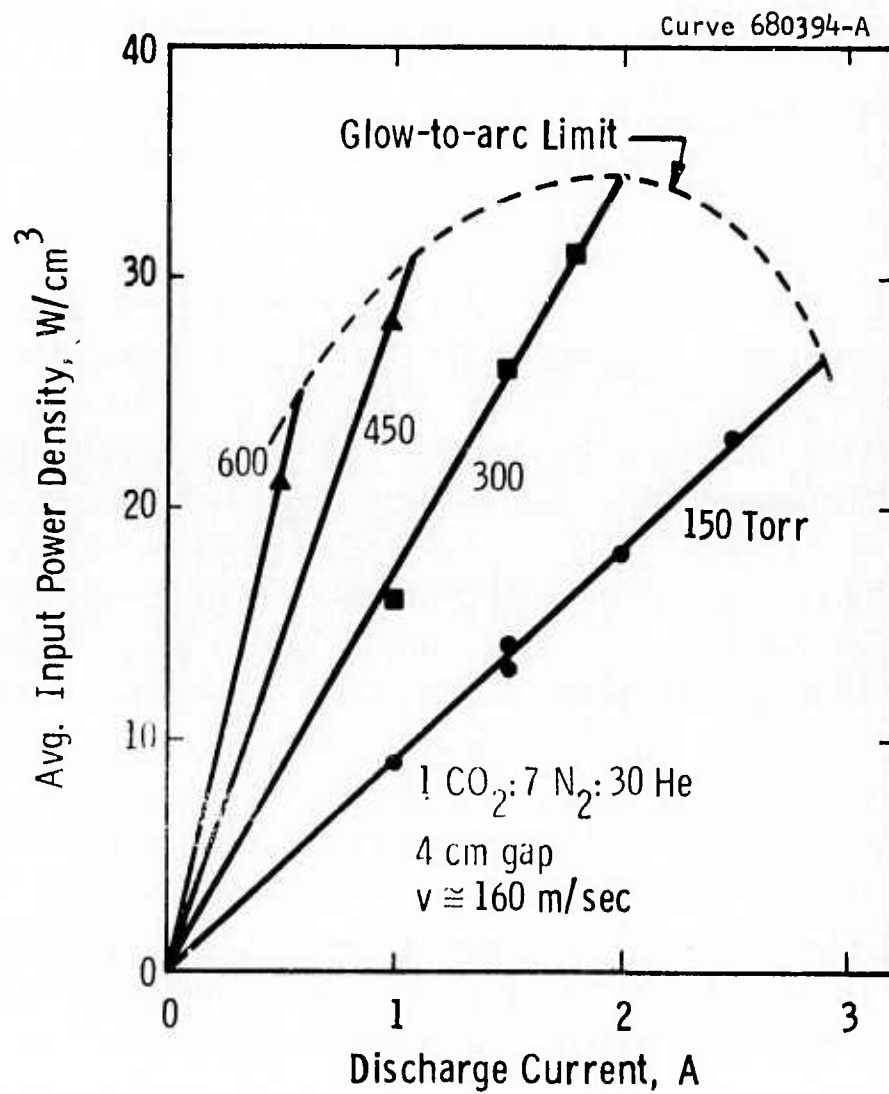
Fig. 2:9 Average input power density versus total discharge current to module.

15

density for the parameters shown. Although glow discharges have been operated up to atmospheric pressure, the optimum pressure for achieving maximum input power appears to be around 300 Torr. This same result was obtained at the larger gap settings. The optimum pressure was raised to higher pressures by increasing the relative amount of N_2 in the discharge; however, this parameterization was not optimized due to the limited time available. Any combination of operating parameters that falls below the dashed curve resulted in a stable discharge. Thus, we see that it is possible to design multi-kilowatt laser systems using the COFFEE laser excitation concept. Predicted laser performance capabilities are described in Section 3.

No systematic study of gas degradation effects was included in this program. However, it has been observed that there are no problems if arcing is avoided. As reported earlier,[1] the discharge has been run for over one hour in a closed-loop flow system without any make-up gas, and no significant changes, such as buildup of CO or NO_x and increased operating voltage, are observed. On the other hand, we found that the glow voltage does increase with time if the discharge is operated for an extended period of time just below the current limit for arcing. Furthermore, the current threshold for arcing gradually lowers. These results are believed to be caused by "partial arc-overs" which occur just below the current level which produces a complete glow-to-arc transition with collapse of the glow voltage. Since many of the tests described in this section required operation of the discharge near this condition in order to establish the stability limits, it was found desirable to add up to 2% H_2 to the laser gas mixture in order to achieve long term discharge stability and reproducibility of results for operating periods over 1 hour. The addition of H_2 does decrease the small-signal gain, however, as described in Section 2.3 and certain tradeoffs must be made in the design of practical laser systems. We believe the H_2 reduces the O_2 which is liberated during dissociation of the CO_2 when arcing occurs. One could also add CO to the gas mixture to purposely drive the reaction backwards. This latter technique was not used extensively in this study.

16

The maximum power input to the glow discharge without sparking was found to be proportional to the cathode pin array area. For example, with an 8 cm gap at 286 Torr of $1CO_2:7N_2:20He:0.6H_2$ mixture and flow velocity of 150 m/sec, it was possible to obtain 12.6 kW input using only the 5 upstream rows of cathode pins. With all 11 rows of cathode pins connected, the maximum arc-free input power was 22.9 kW (~ 30 W/cc, see Fig. 2:5). A "quicky" experiment demonstrated that it is possible to extend the discharge downstream to more than 20 cm by increasing the cathode array dimension in the flow direction. The only restriction, other than arcing, is that one must not overheat the gas to the point that lasing action stops as described in Section 3.

The pin density was varied from 0.25 to 1.00 pins/cm^2 with negligible affect on the glow stability maximum input power. This variation was accomplished by disconnecting intermediate rows of pins. The discharge was not as uniform in the vicinity of the cathode in these cases. The pin density was also constrained by the maximum current that can be drawn from a single pin. For example, at p = 280 Torr with a 1:7:20 gas mixture flowing at 150 m/sec, 100 mA was about the maximum single pin current that could be obtained with a 4 cm gap and upstream discharges. When only a single row of pins having the same 1 cm transverse spacing was inserted into this same gas flow field, 35 mA/pin was the maximum attainable current without arcing. This further indicates that the upstream discharges tend to favorably "condition" the gas for the downstream discharges.

If one increases the pin density, there is still an upper limit to the maximum current density, based on the area of the discharge column, which can be obtained before arcing occurs. Adding more cathode pins just lowers the current per pin required to achieve this threshold current density and makes the cathode more complex to build.

17

2.3 SMALL-SIGNAL GAIN MEASUREMENTS

2.3.1 Description of Gain Measurement Technique

The experimental setup is schematically shown in Fig. 2:10.
A tunable CO_2 probe laser was operated in the TEM fundamental mode to
obtain minimum beam divergence. An adjustable iris attenuated the beam
to intensity levels which avoided saturation of the detector. Germanium
beam splitters, placed along the path of the laser beam, directed samples
of the beam to a power meter, a spectrum analyzer and a UV illuminated
phosphor screen. The laser beam was then chopped with a polished stainless
steel blade so that the beam reflected off the chopper passed through
a variable attenuator and fell on a pyroelectric detector. The transmitted
beam was directed through the laser discharge by means of a set of beam
steering mirrors. Any region of the discharge along a path perpendicular
to the gas flow direction and parallel to the electrode surface could be
probed by moving these mirrors horizontally and vertically. A front
surface mirror was located on the other side of the discharge. Its
alignment was adjusted with micrometer screws so that the probing beam
was reflected almost back on itself. Thus, the returned beam also fell
on the same pyroelectric detector as shown in Fig. 2:10. The output of
the pyroelectric detector was fed into a lock-in amplifier. The reference
signal for the lock-in amplifier was generated by chopping a light
source with the same chopper mentioned above. It was detected by a
photodiode. The output of the lock-in amplifier was displayed on a
chart recorder.

The system was initialized by first observing output V_1 from
the lock-in amplifier when the beam reflected off the chopper was
temporarily fully attenuated. Care was taken to assure that the
pyroelectric detector was operated in its linear range. Then the
variable attenuator was readjusted until the lock-in amplifier output
was zero with the main CO_2 discharge turned off. Finally, the discharge
was turned on, and the amplification of the probe beam produced an output
V_2 from the lock-in amplifier. Thus, the total measured gain was given

18

Dwg. 6242A46
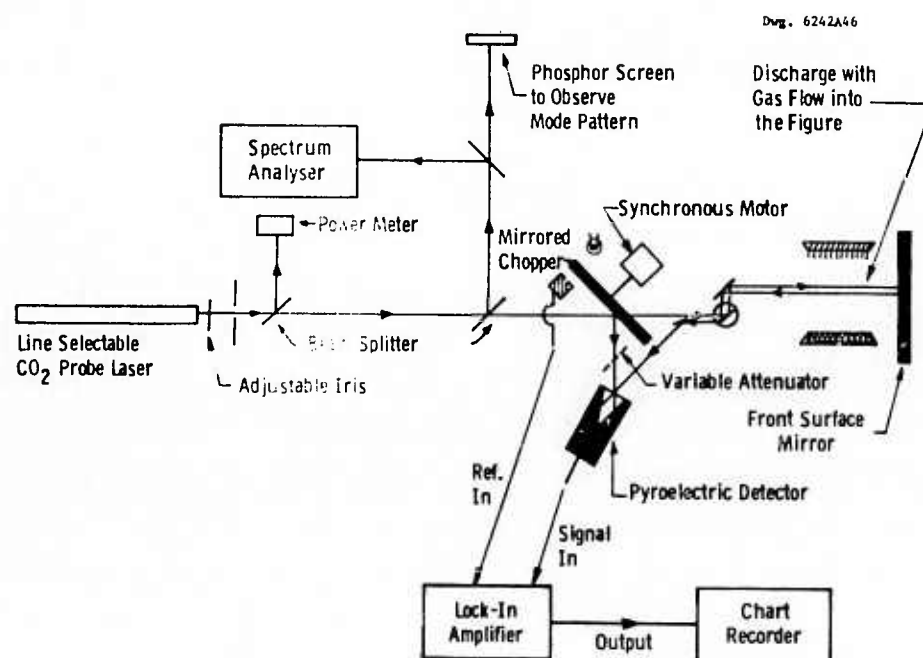
Schematic diagram of the system used to measure gain of CO_2 laser discharge

Fig. 2:10   Schematic diagram of the system used to measure
            gain of CO_2 laser discharge.

19

by V_2/V_1. Since the total active path length was 20 cm, the percent gain per centimeter was

$$g_o = \frac{1}{20} \left(\frac{V_2}{V_1}\right) \times 100 \qquad (2:1)$$

In principle, very accurate measurements can be obtained with this method because extremely small values of V_2 can be measured using this nulling technique and the high sensitivity scales of the lock-in amplifier. The main limitation is the stability of the reference signal V_1. In the present case the probe laser had an inherent drift which limited the useful sensitivity enhancement to a factor of ten. This permitted the measurement of gain as low as 0.01%/cm.

2.3.2 Experimental Results

The integrated small-signal gain over a 20 cm path perpendicular to both the gas flow direction and the electric field was investigated for a cathode-to-anode spacing of 8 cm. The variation of the gain in the gas flow direction (horizontal), midway between the cathode and the anode was measured. A vertical scan of the gain was also made between the electrodes at the position where maximum gain was observed in the horizontal scan. The dependence of the gain at the P_{22} transition upon gas pressure, discharge current, and hydrogen partial pressure were studied at the mid-plane. The gain variation with J-values of both the P-branch and the R-branch were also studied for a fixed gas composition and pressure. The small-signal laser gain for the P_{22} transition as a function of down-stream distance from the first row of cathode pins is shown in Figs. 2:11 and 2:12 for total discharge currents of 1.0 A and 1.5 A, respectively. The gas mixture was $1CO_2:7N_2:20He:0.2H_2$. The total gas pressure varied about 20% during the course of the measurements because some gas escaped out of the blower shaft seal. Hence, the gain was normalized to 280 Torr using the pressure dependence shown in Fig. 2:14. The gas flow velocity was 150 m/sec, and the specific electrical energy input to the discharge at 1.5 A was 50 kJ/lb. The row ballast resistors were adjusted to give nearly constant power input per unit volume (see Fig. 3:10). At 1.5 A
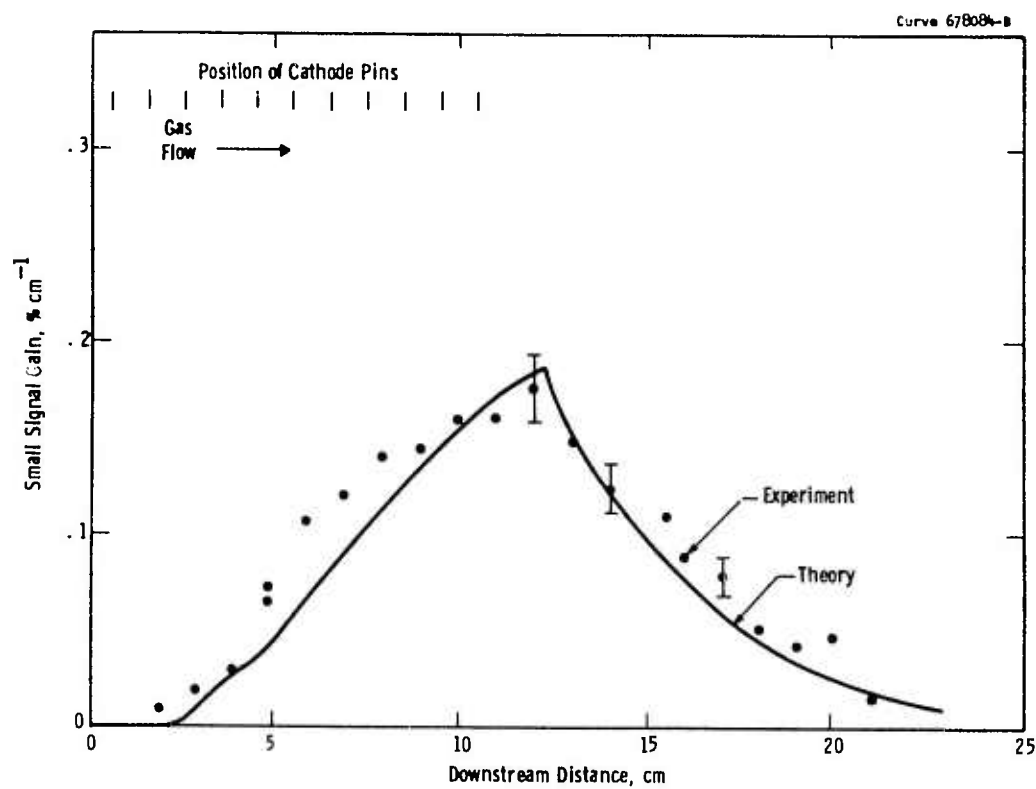
20

Fig. 2:11 Variation of small signal gain along the flow
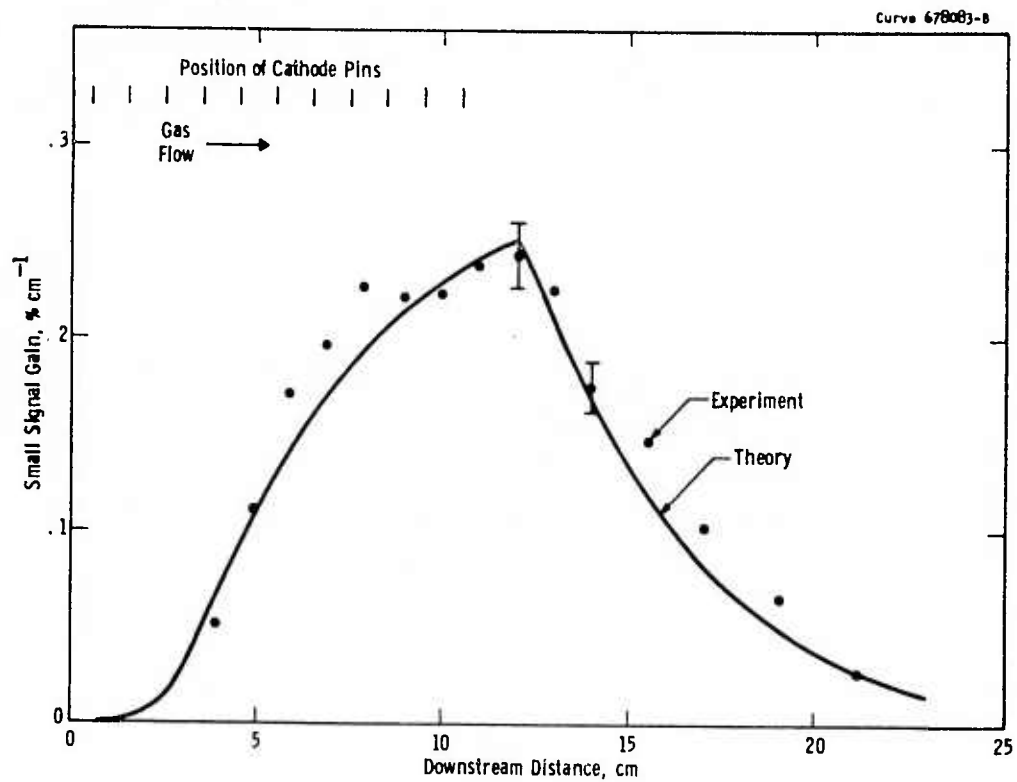direction for I = 1 Amp.

21

Fig. 2:12 Variation of small signal gain along the flow
direction for current = 1.5 Amp.

22

the discharge was operating just below the sparking limit. The variation of power input per unit volume in the flow direction is further described in Sections 2.2 and 3.2.4. In Figs. 2:11 and 2:12, the dots are the experimental measurements and the solid curves are the theoretical predictions based on computer calculations with various assumed values of water vapor content as explained in Section 3.2.4. The theoretical curves for the assumed value of 0.25% water content agrees with both the maximum gain and the shape of the gain curve within the scatter of the experimental data.

In order to match the position where the experimental and theoretical curves peaked, the theoretical curve was displaced downstream by 1.5 cm. This shift is qualitatively consistent with a displacement of the current distribution arising from the gas flow. The drift velocity of positive ions in the discharge is given by $\overline{W} = \mu_+ \cdot \overline{E}$ cm/sec where μ_+ is the mobility of positive ions in the mixture and E the electric field in volts/cm. The positive ion mobility in the $CO_2:N_2$:He mixture used is about 7.1 cm^2/volt-sec and the E/p under the last row of cathode pins was 6.1 volts/cm-Torr. This yields a positive ion drift velocity of 3.3×10^4 cm/sec. The gas flow velocity here was 1.6×10^4 cm/sec. The current path appears to be deflected downstream with respect to the cathode pins, which anchor the discharge, by an angle which is proportional to the ratio of gas to ion drift velocities. Thus, the expected displacement of current distribution at the mid-plane (4 cm below the cathode) was approximately 2 cm, which is in agreement with the displacement required to match theory with experiment.

Figures 2:11 and 2:12 show that the small-signal gain increased (by integration) as the laser gas passed through the discharge. Beyond the discharge region, the gain fell off exponentially with a decay time of about 260 μsec. This relatively long decay time is due to the nitrogen acting as an energy reservoir. The shape of the gain profile in the discharge is governed by both the pumping rate and the deactivation rate. The details of these processes are discussed in Section 3. However, it should be pointed out that the shape of the gain profile in the downstream direction will be completely different in the presence of stimulated emission during lasing.

23

A vertical scan of the small-signal gain for the P_{18} line at 1.5 cm downstream from the last row of cathode pins is shown in Fig. 2:13. The gain expressed in percent per centimeter is plotted against distance measured from the cathode. Several measurements were taken at 1.0 and 1.5 A at each vertical position and were normalized to a total pressure of 280 Torr using a $1CO_2:7N_2:20He:0.2H_2$ gas mixture. Averages of these measurements for 1.0 A are indicated by dots and those for 1.5 A are indicated by triangles. The error bars correspond to the standard deviation of the data taken at each position. The results indicate that within the accuracy of the measurements the gain was quite uniform across the 8 cm interelectrode spacing, except perhaps for a slight fall-off near the cathode. The pressure dependence of the small-signal gain at the P_{22} line, for a discharge current of 1.0 A and for a fixed gas composition of $1CO_2:7N_2:20He:0.2H_2$ in the pressure range of 70 to 280 Torr is shown in Fig. 2:14. The measurements were made midway between the cathode and the anode and 1 cm downstream from the last row of cathode pins. The gas flow velocity at the entrance to the discharge region was 150 m/sec. The log-log plot of the variation of the gain with pressure P shows that the gain varies asymptotically as $P^{-.74}$ for large pressures. A similar pressure dependence was also observed for a 1.5 A discharge.

Introduction of a small amount of hydrogen into the laser gas mixture improved the long term discharge stability conditions. However, it also resulted in reduced gain. Fig. 2:15 shows the variation of measured small-signal gain with total discharge current for various amounts of hydrogen added to a fixed $1CO_2:7N_2:20He$ composition at a total pressure of $\sim$280 Torr. The measurements were made at the midplane 1 cm downstream from the last row of cathode pins. The solid curves are straight lines fitted through the data points. The gain varies linearly with current for a fixed gas composition as expected. The 1.5 A data are replotted in Fig. 2:16 as a function of hydrogen concentration. In general, the small-signal gain was reduced approximately 40% with the addition of 1% H_2 to the 1:7:20 gas mixture at 280 Torr. The gain decreased exponentially with further addition of H_2. The dashed line represents the theoretical predictions for various assumed values of water vapor content. Unfortunately,

24
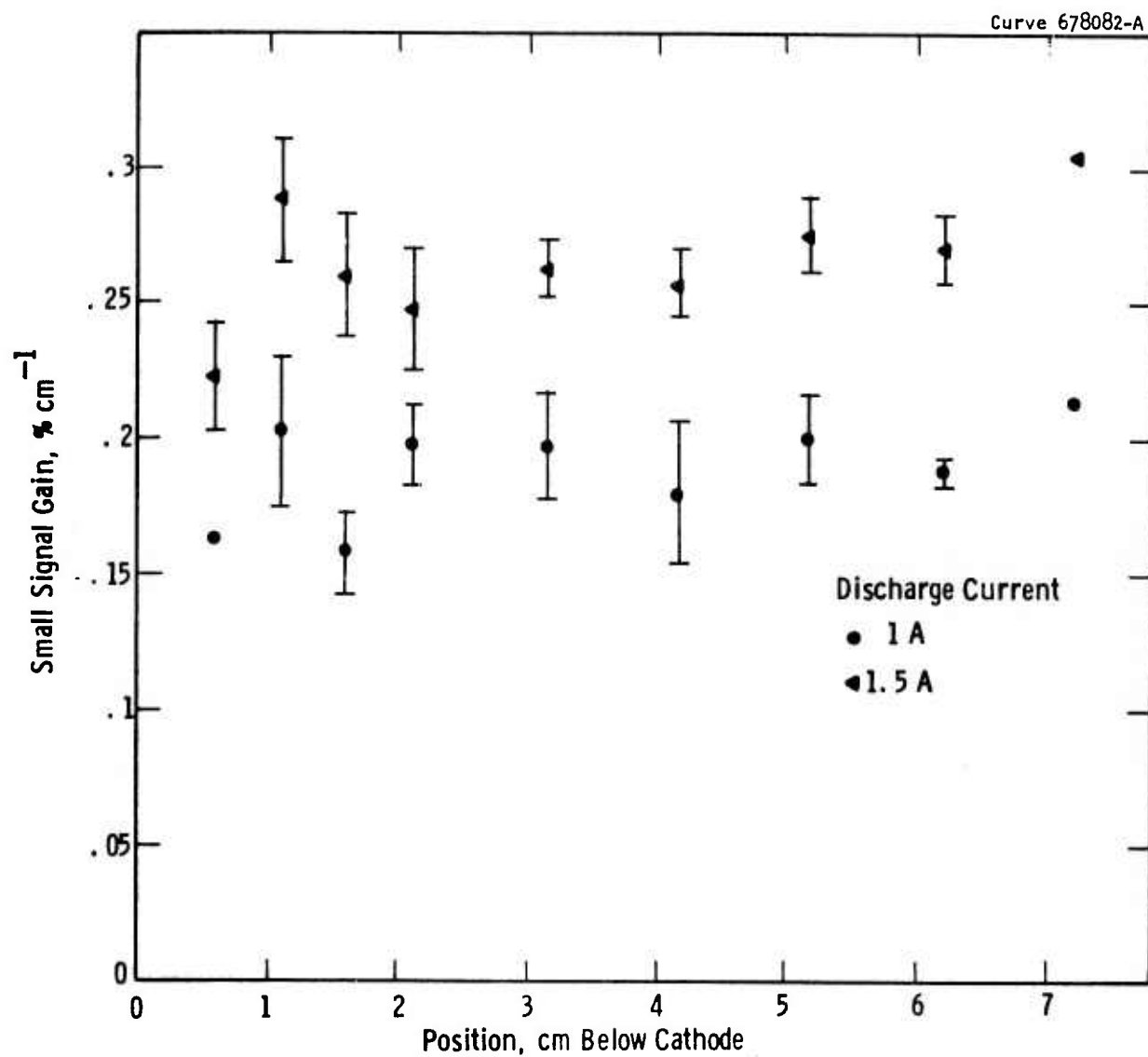
Fig. 2:13 Small-signal gain on P18 line versus position below cathode pins 1.5 cm downstream of 11th row at a total pressure of 280 Torr.

25

Curve 678080-A
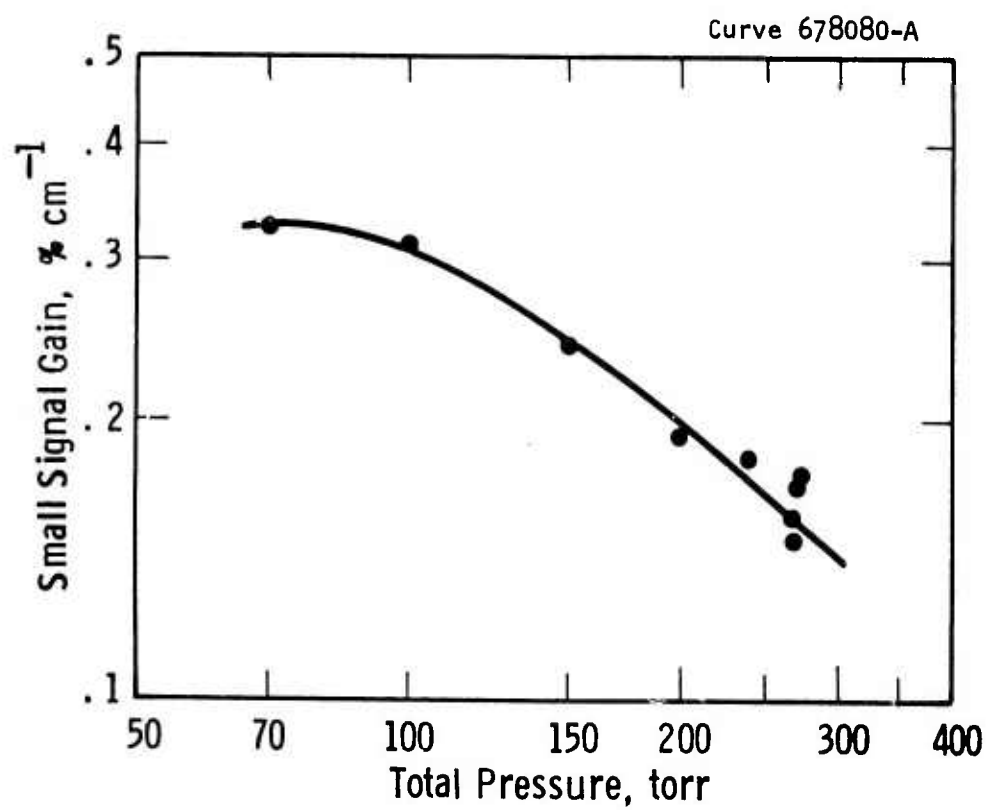
Fig. 2:14   Small-signal gain as a function of total pressure for a $1CO_2$:$7N_2$:$20He$:$0.2H_2$ mixture at 1 A discharge current.

26

Curve 678085-B
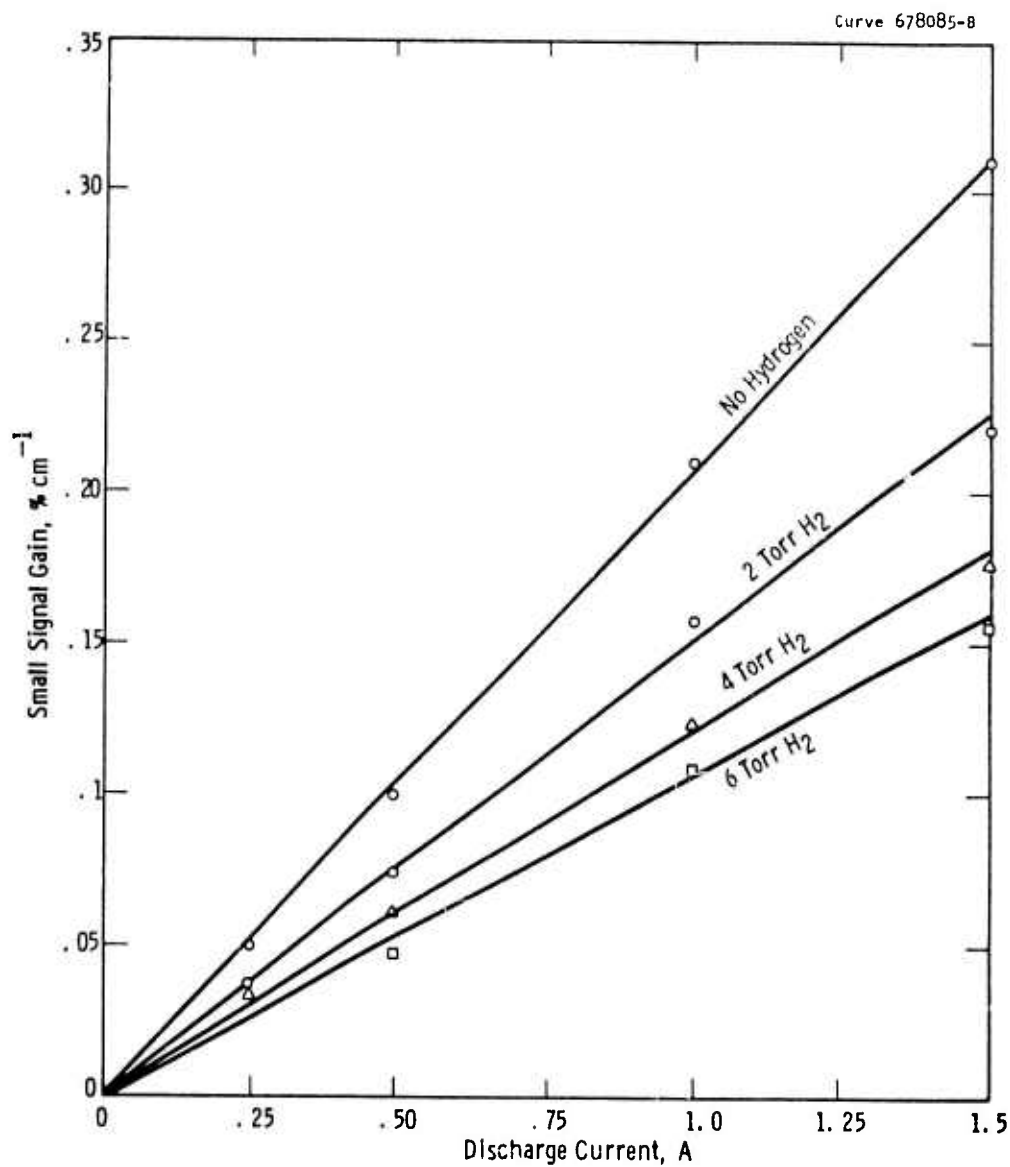
Fig. 2:15 Variation of gain with discharge current in
$1CO_2:7N_2:20He:xH_2$ mixture at 280 Torr.

27

Curve 678081-A
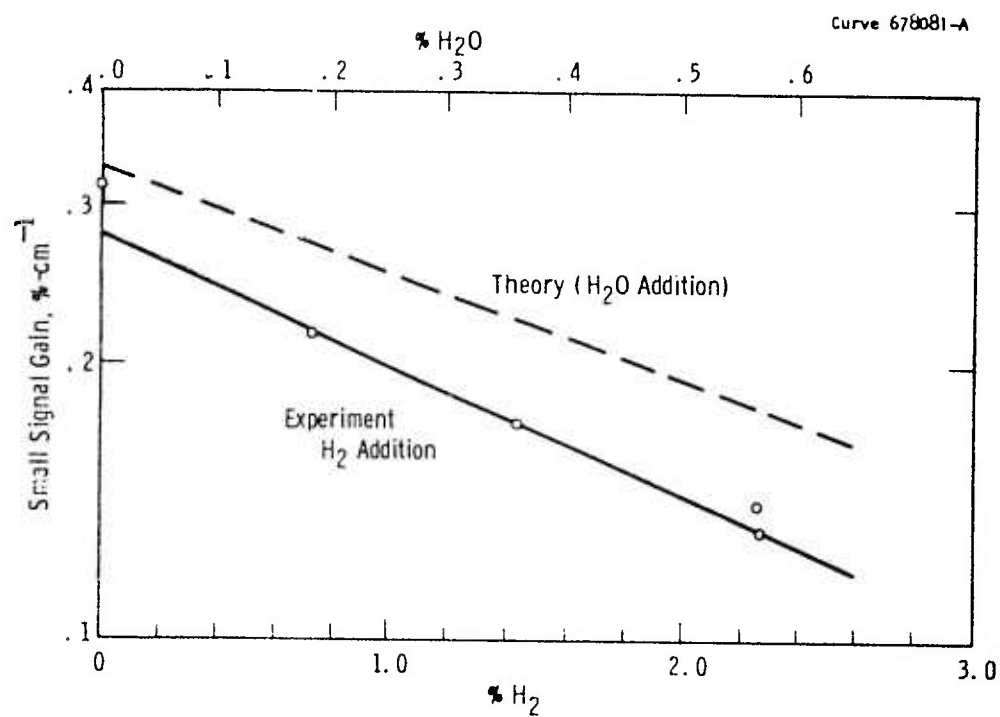
Fig. 2:16 Small-signal gain as a function of hydrogen
and water vapor concentration at 280 Torr gas
pressure and 1.5 amp discharge current.

28

no measurements were made with H_2O added in place of H_2. A linear extrapolation of the H_2 data back to zero H_2 concentration gives a gain equivalent to that predicted by a 0.15% H_2O content. One might reasonably expect a flow system background water vapor concentration of this magnitude since commercial grade gases were used and the system was not bakable under vacuum. The reduction in gain caused by the addition of H_2 was 1/3 times that predicted for H_2O. This large reduction in the measured gain implied that in the presence of the discharge, chemical reactions occurred which led to the formation of additional water vapor. A more detailed comparison of the two curves is given in Section 3.2.4.

2.4 GAS TEMPERATURE MEASUREMENTS

The kinetic temperature in molecular gas laser media such as CO_2 can be inferred from measurements of the small-signal gain taken at various P and R-branch laser wavelengths. This technique has been applied by Avizonis, Dean and Grotbeck[5] using P-branch gain measurements performed upon CO_2 gas dynamic lasers. More recently, the gain formulations have been modified at Westinghouse and applied to P and R-branch gain measurements in UV-initiated, pulsed $CO_2:N_2:He$ laser discharges.[6] These gain techniques have the advantage that the gas temperature is determined at the site and time of the laser population inversion, and the method does not perturb the gain medium. For the COFFEE laser discharges studied here, P and R-branch gain measurements were performed in the interelectrode midplane 1.0 cm downstream from the eleventh row of pins for total currents of 1.0 and 1.5 A.

The small-signal gain relationship at line center can be expressed as[7]

$$\frac{\alpha(J)\lambda(J)}{J\ F(v,J)} = K_c B_{v'} n_{v'} \exp\left[-J(J \pm 1)\theta_{v'}/T_r\right]$$

$$- K_c B_{v''} n_{v''} \exp\left[-J(J \mp 1)\theta_{v''}/T_r\right] \qquad (2:2)$$

29

for a vibrational-rotational transition from the (v',J') level to the (v'',J'') level. The lower signs are selected for P-branch gain with the rotational quantum number $J = J''$ designated by the lower-lying level. The R-branch gain is obtained by selecting the upper signs with $J = J'$ designated by the higher-lying level.[*] The terms $\alpha(J)$, $\lambda(J)$ and $F(v,J)$ are the measured small-signal gain, the wavelength corresponding to the particular transition, and the vibrational-rotational interaction factor, respectively. The quantities B_v and n_v are the rotational constant and the population density, respectively, for the vth vibrational level. The characteristic rotational temperature θ_v is defined in terms of the rotational constant B_v as

$$\theta_v = hcB_v/k, \qquad (2:3)$$

where h, c and k are Planck's constant, the velocity of light and Boltzmann's constant, respectively.

The equilibrium rotational temperature T_r is assumed to be identical for both the upper and the lower laser levels, and T_r is further assumed to be equal to the gas kinetic temperature T. These assumptions are well-founded for the CO_2 lasers considered here, since rotational thermalization and equilibrium with the gas kinetic reservoir occur in times on the order of 1 nsec. Thus, a determination of the rotational temperature T_r from gain measurements provides an excellent estimate of the gas temperature based upon the assumption that $T \approx T_r$.

The collisional constant K_c applies for collisional broadening of the vibrational-rotational transition, and is given by

$$K_c = 16\pi^3 \sigma c \, S_{v'v''}/3kT_r \, \nu_c \qquad (2:4)$$

---

[*] Note: This definition of J for the R-branch simplifies the equations in this section; however, the equations in Appendix E of Section 3.1 are similarly simplified by taking the alternate convention of setting $J = J''$ for the R-branch.

where σ is the molecular symmetry number ($\sigma = 2$ for CO_2), and $S_{v'v''}$ is the square of the vibrational transition moment. The collision frequency ν_c for optical broadening can be expressed as

$$\nu_c = (8kT/M)^{1/2} \sum_j n_j \sigma_j (1 + M/M_j)^{1/2} \tag{2:5}$$

where M is the mass of the laser particle and n_j, σ_j and M_j are the number density, optical broadening cross section and mass, respectively, of the gas mixture constituents. The sum is taken over all gas species, including the laser species. Under the assumption that $T_r = T$, the collisional constant K_c is seen to vary as $T_r^{-3/2}$.

Inspection of Eq. (2:2) reveals that if the small-signal gain α is measured for various transitions $(v',J') \to (v'',J'')$, the only undetermined quantities are $n_{v'}$, $n_{v''}$ and T_r. Since $n_{v'}$ and $n_{v''}$ are not known a priori, further approximations to Eq. (2:2) are required in order to extract T_r from the gain measurements. This can be accomplished by removing the first term of Eq. (2:2) as a common factor and approximating the remaining term in $\exp[\pm 2J\theta/T_r]$ by unity with $B_{v'} = B_{v''} = B$ and $\theta_{v'} = \theta_{v''} = \theta$. For typical CO_2 values of J = 20 with $T_r = 300°K$, this exponential term differs from unity by only about 7%; thus the approximation does not introduce significant error into the gain formulation for typical CO_2 laser conditions. The resulting gain equation is considerably simplified, however:

$$\frac{\alpha(J) \; \lambda(J)}{J \; F(v,J)} \approx K_c B(n_{v'} - n_{v''}) \; \exp[-J(J \pm 1)\theta/T_r] \tag{2:6}$$

Taking natural logarithms of both sides of this equation yields a convenient linear relationship:

$$\ln[\alpha(J) \lambda(J)/J \; F(v,J)] = -J(J \pm 1) \frac{\theta}{T_r} + \ln[K_c B(n_{v'} - n_{v''})] \tag{2:7}$$

31

The left-hand side involves the measurable quantities $\alpha(J)$ and J, and the first term on the right-hand side involves the measurable quantity $J(J \pm 1)$. Thus a plot of $\ln[\alpha(J) \lambda(J)/J F(v,J)]$ as a function of $J(J \pm 1)$ will yield the same straight line for both P and R branch data. The slope of this line is $-\theta/T_r$, and the ordinate intercept is $\ln[K_c B(n_{v'} - n_{v''})]$. The gas temperature $T = T_r$ can be evaluated from the slope, and the population difference $(n_{v'} - n_{v''})$ can be calculated from the ordinate intercept value and T_r.

This method of determining the gas temperature has been programmed for automatic computer treatment of raw experimental gain data. The computer code GARED calculates the appropriate variables for Eq. (2:7), and performs a linear least squares fit of these values to a straight line. Both P-branch and R-branch gain data are considered separately, since the approximation $\exp[\pm 2J\theta/T_r] \approx 1$ provides a slightly different linear relationship for P and R-branches. The approximation causes an overestimation of T_r from the P-branch data, and an underestimation of T_r from the R-branch data. Thus separate fitting procedures applied to P and R-branch gain data should bracket the true value of T_r; in practice, the arithmetic average of these values is taken as the gas kinetic temperature.

The numerical constants employed in these computations were derived from the latest measured values reported in the scientific literature. Wavelengths for the various CO_2 P and R-branch transitions were taken from the measurements of Barker and Adel,[8] and the vibrational-rotational interaction factors $F(v,J)$ were deduced from the formulations given by Arie, Lacome and Rossetti.[9] Rotational constants $B_{00°1} = 0.3866$ cm^{-1} and $B_{10°0} = 0.3897$ cm^{-1} from Herzberg[10] were used for the CO_2 upper and lower laser levels, respectively. The molecular symmetry number $\sigma = 2$ for CO_2 was obtained from Herzberg.[11] The line strength $S_{v'v''}$ for the $(00°1) \rightarrow (10°0)$ laser transition in CO_2 was taken as 1.483×10^{-39} erg cm^3 from the recent measurements of Murray, Kruger and Mitchner,[12] and the CO_2 optical broadening cross sections for CO_2, N_2 and He were taken as 131, 114 and 48 $\overset{\circ}{A}{}^2$, respectively from this same reference.

32

Gain measurements were performed at a location 1.0 cm downstream from the eleventh row of pins in the COFFEE electrode array, midway between the anode and cathode. An 8 cm electrode gap was used. The laser gas mixture was $1CO_2:7N_2:20He:0.2H_2$ with a total pressure of 280 Torr. A fixed entering gas velocity of 150 m/sec was used. With a total discharge current of 1.0 A, small-signal gain measurements were performed at 8 P-branch and 7 R-branch transitions. At the 1.5 A discharge current, 8 P-branch and 10 R-branch gain measurements were made. The particular transitions probed were carefully chosen to avoid the anomalous CO_2 "hot bands" reported by Leonard[13] and by Singer.[14] Specifically, no gain measurements were attempted on the P(20), P(28) and R(15) transitions of the 10.4 μm CO_2 bands, since these transition wavelengths apparently overlap those corresponding to other CO_2 levels which can be highly populated at typical operating temperatures. Such "hot band" transitions can lead to anomalously high observed gain at these wavelengths, by as much as 10% in some cases. Since such anomalies could influence the rotational temperatures deduced from these measurements, the "hot band" wavelengths were not included in the data set.

The observed gains for the various P and R-branch CO_2 transitions are shown in Figs. 2:17 and 2:18. These values have been normalized to a constant background pressure of 280 Torr by employing the empirically-determined relationship

$$\alpha \propto p^{-0.7}, \tag{2:8}$$

where α is the observed gain and p is the measured total gas pressure. Since changes in background pressure were recorded over the 1 to 4 hour duration of a typical experimental run, this normalization procedure was deemed necessary to correct for an observable systematic error. Furthermore, each data point is the average of between 3 and 10 separate observations. Nonetheless, it can be seen that considerable scatter exists in the experimental gain data. This is attributed to instabilities in the output of the probe laser and the rather small signal-to-noise ratio
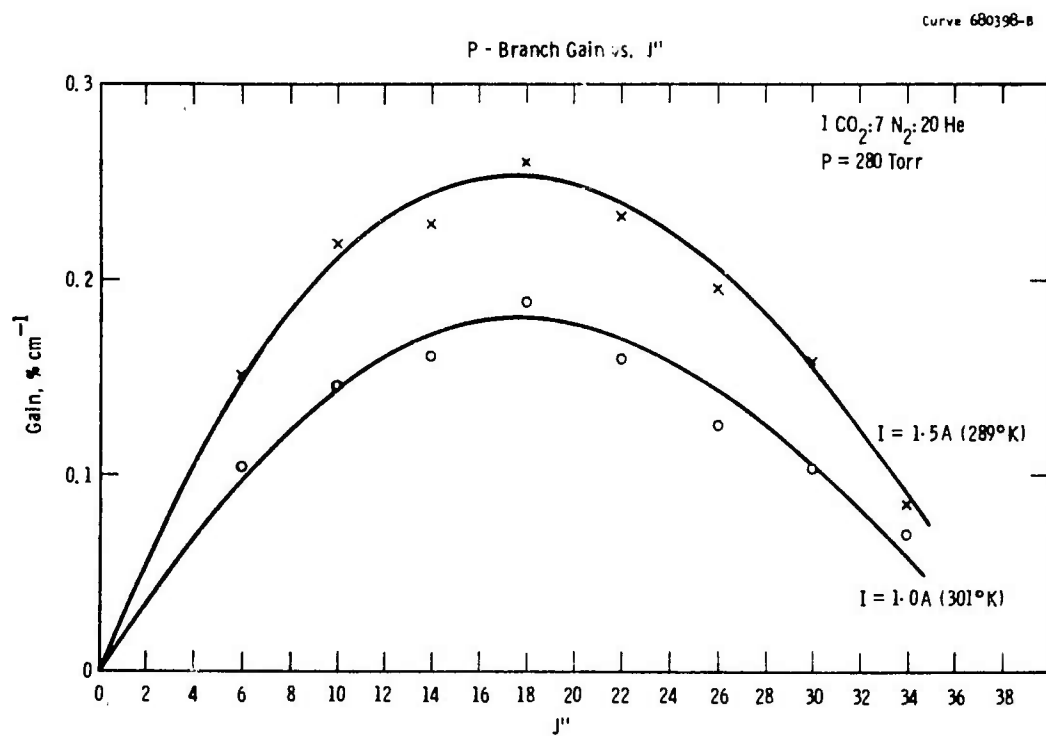
33

Fig. 2:17 P-branch gain versus J".

34
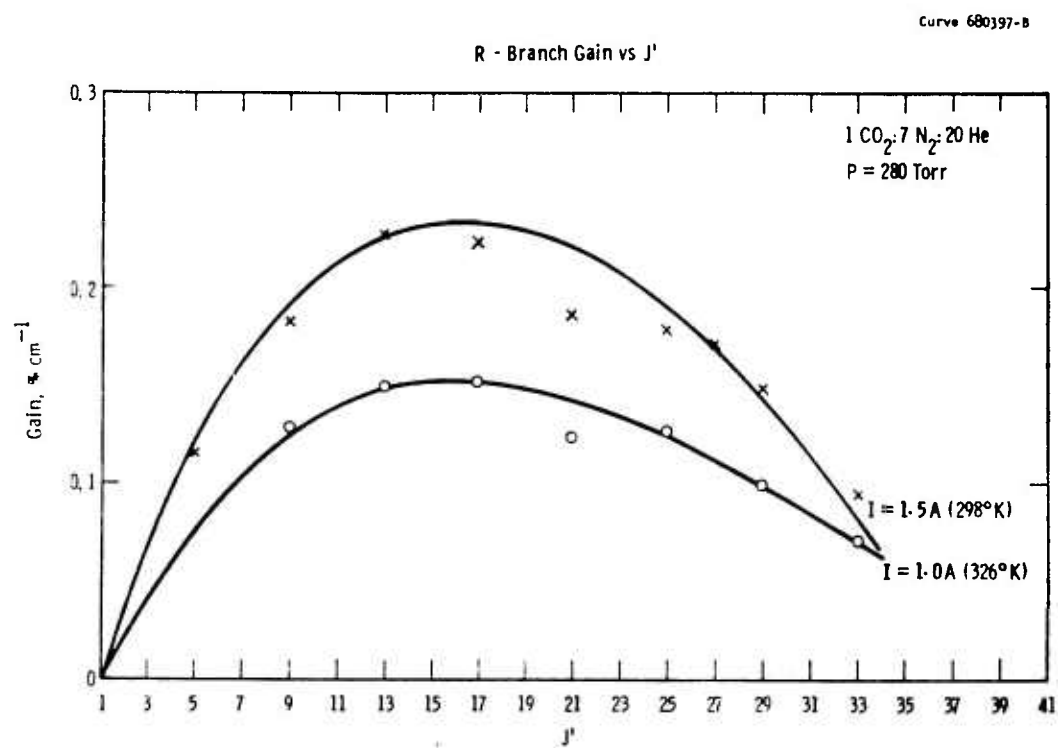
Fig. 2:18   R-branch gain versus J'.

obtained in the detection equipment. The computer least-squares fit to the data is indicated approximately by the solid curve drawn through the experimental points.

For the 1.0 A case, the P and R branch temperatures determined from the GARED program were 301°K and 326°K, respectively, to yield an average of 313°K. For the 1.5 A case, these values were 289°K and 298°K, respectively, for an average of 293°K. These results are anomalous in that the higher current case yields a temperature lower than the lower current case, and the 1.5 A data yields a temperature below the ~300°K inlet gas temperature. Consequently, we conclude that the scatter in the experimental data is sufficient to introduce significant errors into the temperature determination. Based upon error calculations performed previously for UV-initiated, pulsed CO_2 laser gain measurements, we estimate that the uncertainty in the derived temperatures is ~20°K for the 1.0 A data and ~40°K for the 1.5 A data. Clearly an improved gain measurement technique will be required to reduce errors in the gas temperature determination.

Despite these uncertainties, the gain reduction technique demonstrated that the gas temperature increased by ~30°K during traversal through the COFFEE excitation region. Furthermore, this result agreed with the laser kinetics prediction shown in Fig. 3:11. With this temperature rise, it is evident that the CO_2 laser kinetics were not affected seriously by the deleterious effects of elevated gas temperatures which occur beyond ~450°-500°K. Thus excitation regions extended even further in the downstream dimension should result in increased laser excitation and power output.

3.   THEORETICAL MODELING

3.1 LASER KINETICS MODEL

3.1.1 Introduction

In the COFFEE CO_2 laser kinetics model we have considered five general mechanisms: (1) the electrical excitation of the gaseous medium, (2) the collisional relaxation of energy in the gas, (3) the transport of thermal energy by gas flow, (4) the interaction of coherent radiation with the CO_2 molecules, and (5) the feedback of the coherent radiation by end mirrors. Considerable work has been done in these areas by many workers, particularly in conventional low pressure, low energy CO_2 devices. The object of developing the present model was to extend previous treatments to include continuous operation, the temperature dependence of the collisional relaxation processes, the electric field dependence of the electrical excitation, and the effects of water vapor and gas flow. The basic model is the one which has been successful in simulating pulsed CO_2 lasers.[15] However, it was modified to include the gas flow properties and to model the continuous operation of the COFFEE laser. The complete COFFEE CO_2 laser kinetics model is described in the following sections.

3.1.2 General Description of the Model

The basic premise of the COFFEE CO_2 laser kinetics model is that the vibrational modes of the molecules can be considered as completely separate energy reservoirs which interact by electronic and molecular collisions and by photon emission or absorption. Each mode is assumed to be in local Boltzmann equilibrium due to rapid intramode vibrational-vibrational (VV) relaxation. Thus, the energy content of each vibrational mode is characterized by its own Boltzmann temperature and is described by its own rate equation.

37

The fraction of the input electrical power which excites the various vibrational modes and electronic levels has been determined by Lowke et al.[16] from electron energy distribution function computations in CO_2 laser mixtures. These fractions are computed as a function of E/N, where E is the electric field and N is the total number density of the gas. In general, the value of E/N in the discharge is a function of position downstream and its value at any position was determined from the value of the electric field calculated from the measured glow voltage and from the total number density calculated from the specific heat rate equation, assuming that the pressure is constant throughout the laser cavity. The experimental values of the current density were used to obtain the input electrical power.

From the theoretical models one is able to predict the proper temperature dependence of the vibrational-vibrational (VV) and vibrational-translational (VT) collisional relaxation rate constants. However, existing theories yield quite poor values for the magnitude of these rates. Consequently, the theoretical models were used to provide a three-parameter expression for the temperature dependence of these rate constants, and this expression was fitted to measured values at three different temperatures. Relaxation rates for which no experimental measurements are available were estimated on the basis of physical arguments. Most of the rates involving water must be estimated in this fashion. Water was included in this model because its relaxation rates are extremely high and exhibit anomalous temperature behavior. Thus, even very small amounts of water vapor will have a significant effect on the results. On the other hand, hydrogen has not been included because its relaxation rates are at least eight times slower than those of water vapor and because the concentration of hydrogen was never allowed to become very large.

As the gas temperature increases in the gas flow direction, the gas flow velocity increases and the number density decreases. These changes are directly proportional to the temperature or its inverse and were included in the model. Although these changes are important, the collisional rates are also dependent on the gas temperature and in many cases exhibit large changes for small temperature variations. Thus, it

is necessary to consider the nonstationary equation of thermal conductivity to determine the gas temperature as a function of the downstream position (all gas properties are assumed to be constant within any cross-section perpendicular to the gas flow direction). The model employs the specific heats of the gas components at constant pressure and includes the three major sources of gas heating: energy defect heating from VV collisional transitions, intermode heating from VT collisional transitions, and gas heating from the electrical discharge. The loss of electrical input energy by electronic excitation followed by photon emission was also included.

The total radiation intensity is the sum of the spontaneous radiation intensity not collimated by the cavity mirrors and the spontaneous plus stimulated radiation intensity which is collimated by the cavity mirrors. The collimated radiation intensity was calculated from the rate equation which defines the laser gain. Included were the effects of spontaneous emission, constant input radiation intensity (in case the laser is used as an amplifier), mirror and cavity losses. Doppler, natural, and pressure broadening of the linewidth were also included. The fractional populations of the rotational levels were considered in computing the stimulated emission transition rates.

As just described, the computation proceeds as shown in Fig. 3:1. The experimental values of the electric field, E, and current density, j, as a function of downstream position, x, were used to determine the electron excitation rate coefficients and the input power values. This information was used in the laser kinetics model to calculate the gas temperature, T, and many other laser parameters, taking into consideration the discharge and laser cavity dimensions as well as the optics design, initial gas flow velocity, temperature, and pressure. The collisional rate coefficients determine the collisional excitation and relaxation. The environmental changes a molecule experienced as it flowed through the discharge cavity were incorporated in the laser kinetics model. The result was the determination of the gas flow velocity, gas density, gas temperature, vibrational temperatures, gain, output power, and output efficiency as a function of the downstream position. The basic rate equations used in this model are described in the next section.

39

```
                        ┌──────────┐
                        │   E, j   │
                        └──────────┘
                             │ f ( x )
                             ▼
┌──────────────────┐  f ( E/N)  ┌──────────────┐  f ( Tg )  ┌──────────────────┐
│ Electron Excitation │─────────│ LASER KINETICS │─────────│    Collisional    │
│  Rate Coefficients  │         │     MODEL      │         │  Rate Coefficients │
└──────────────────┘         └──────────────┘         └──────────────────┘
                                    │ f ( x )
                                    ▼
                        ┌──────────────────┐
                        │   Gas Density    │
                        │  Flow Velocity   │
                        │  Temperatures    │        ▭ = Input
                        │     Gain         │        ▭ = Model
                        │    Power         │        ▱ = Output
                        │  Efficiency      │
                        └──────────────────┘
```
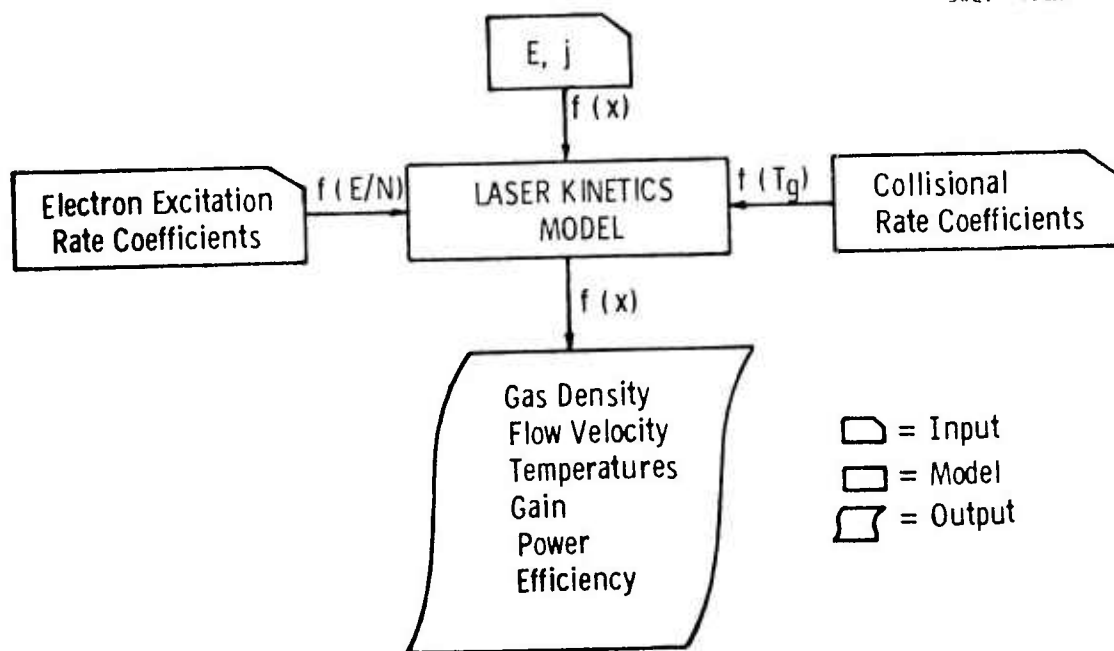
Fig. 3:1 Basic flow diagram of the COFFEE CO_2 laser kinetics model computations.

40

3.1.3 The Rate Equations

From the basic premise of separate energy reservoirs for each vibrational mode, the rate equations can be derived by introducing the following approximations:

1. Translational and rotational motions are so tightly coupled that their energy contents are in Boltzmann equilibrium with each other at the kinetic gas temperature T.

2. Only the bending mode of H_2O (WBM) interacts with the vibrational levels of CO_2 and N_2; the other two H_2O vibrational modes, lying considerably higher in energy, do not exchange significant amounts of vibrational energy with CO_2 and N_2.

3. The WBM can be represented as a perfect simple harmonic oscillator (SHO) with an infinite number of equally spaced energy levels,[17] since only the lowest levels of the H_2O bending mode are appreciably occupied at the temperatures of interest.

4. The N_2 vibrational mode (NVM), the CO_2 asymmetric stretch mode (ASM), the CO_2 symmetric stretch mode (SSM), and the doubly degenerate CO_2 bending mode (BM) can be represented as perfect simple harmonic oscillators with an infinite number of equally spaced energy levels,[18] as their lower-lying energy levels exhibit nearly uniform spacings.

5. The intramode VV relaxation is so rapid that each vibrational mode is in local Boltzmann equilibrium and can be characterized by its own Boltzmann temperature.

6. The anharmonicities in the ASM and SSM are large enough to shift the wavelengths of transitions between the 0n1 and 1n0 energy levels ($n \geq 1$) away from the 00^01 to 10^00 transition wavelength, and out of the wavelength region for which there is appreciable overlap of the linewidths. This wavelength shift and the small occupancies of the upper energy levels permit one to restrict the stimulated emission to the $00^01 - 10^00$ transition.

7. The resonator cavity wavelength discrimination is sufficient to suppress stimulated emission at 9.6 μm.

8. Spontaneous emission and particle diffusion rates are sufficiently small that these processes can be neglected. (However, spontaneous emission is included in the gain equation to provide the initial radiation which is amplified by the laser whenever it is used as an oscillator.)

9. The gas pressure is constant in time, and molecular dissociation can be neglected.

The model is considerably simplified by averaging over all spatial dependencies transverse to the direction of flow and by restricting the laser emission to a single vibrational-rotational transition within the 10.4 μm band. The former simplification restricts the resonator configuration to be plane-parallel. In addition to these approximations, it is assumed that transitions into or out of the doubly degenerate bending mode occur only when the energy transfer involves either one or the other bending mode.

It is further assumed that the application of the Landau-Teller selection rules[19] for vibrational level transitions is valid for collisional interactions between modes, and that the dependence of transition probabilities on vibrational quantum numbers in multiple quanta exchanges may be calculated from the one-dimensional exponential repulsion model of Schwartz, Slawsky, and Herzfeld.[20] For brevity, the latter model is called the SSH theory.

The specific interactions considered in the model are illustrated in Fig. 3:2 for the usual $CO_2:N_2:He:H_2O$ gas composition. Included in the model are three VT, six VV, one stimulated emission, and five electrical excitation processes. The model also included all inverse transitions determined from the principle of detailed balance. These interactions include all those known to be important. The inclusion of water vapor (0.25%) introduces interactions which have not been included in previous models. The stated relaxation times are typical for a 1:7:20 mixture at 280 Torr pressure.
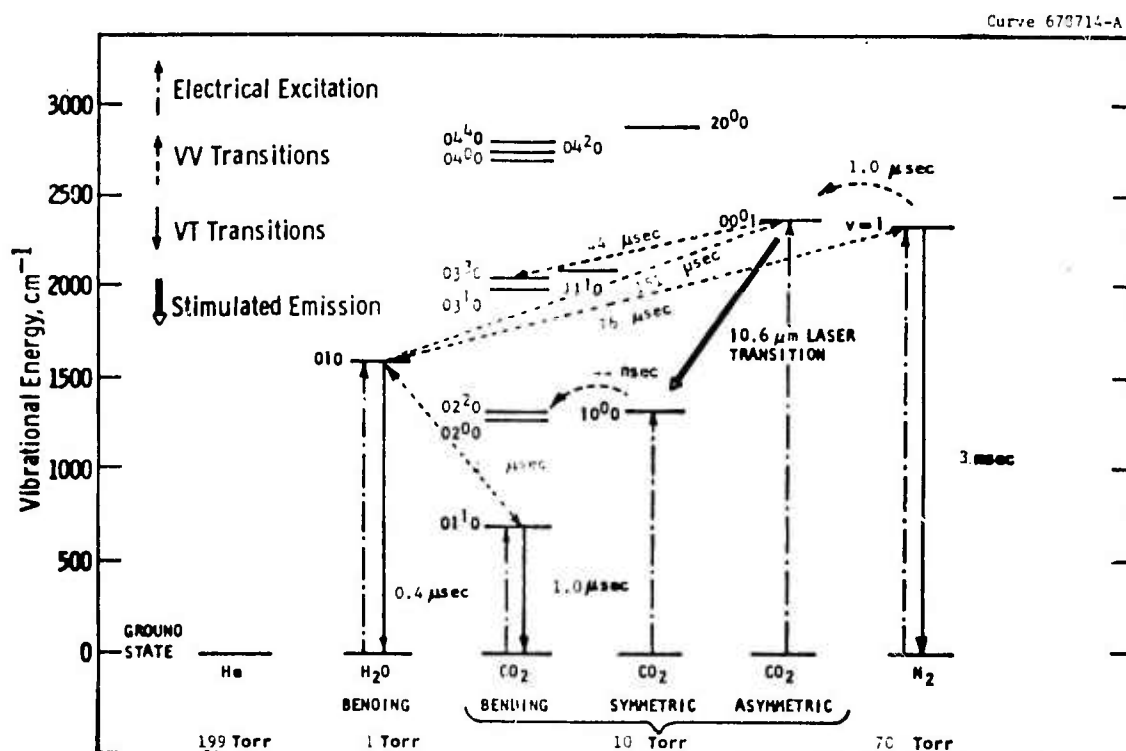
42

Fig. 3:2 Vibrational modes of molecules important in
          CO_2 laser mixtures

43

The energy content of each vibrational mode is described by a temperature: T_n for the NVM, T_w for the WBM, T_a for the ASM, T_s for the SSM, and T_b for the BM. The interactions in Fig. 3:2 generate a flow of energy between the vibrational modes. The application of the aforementioned assumptions to these interactions leads to a rate equation for the Boltzmann factor associated with each of the five vibrational modes.[21] The inclusion of a rate equation for the kinetic gas temperature T and one for the coherent light intensity completes the model. The result is a harmonic oscillator, six-temperature Boltzmann equilibrium model described by the following seven simultaneous differential equations:

$$\frac{\dot{a}}{(1-a)^2} = R_{an}\left[\frac{An-a}{(1-n)(1-a)}\right] + R_{aw}\left[\frac{Fw-a}{(1-w)(1-a)}\right] + R_{ab}\left[\frac{Cb^3-a}{(1-b)^3(1-a)}\right]$$

$$- (1-a)(1-s)(1-b)^2 \ \Gamma + U_a \tag{3:1}$$

$$\frac{\dot{s}}{(1-s)^2} = R_{sb}\left[\frac{Bb^2-s}{(1-b)^2(1-s)}\right] + (1-a)(1-s)(1-b)^2 \ \Gamma + U_s \tag{3:2}$$

$$\frac{2\dot{b}}{(1-b)^2} = -3R_{ab}\left[\frac{Cb^3-a}{(1-b)^3(1-a)}\right] - 2R_{sb}\left[\frac{Bb^2-s}{(1-b)^2(1-s)}\right] - R_{bw}\left[\frac{Gb-w}{(1-w)(1-b)}\right]$$

$$+ 2R_b\left[\frac{\bar{b}-b}{(1-b)}\right] + U_b \tag{3:3}$$

$$\frac{\dot{n}}{(1-n)^2} = -R_{na}\left[\frac{An-a}{(1-n)(1-a)}\right] + R_{nw}\left[\frac{Dw-n}{(1-n)(1-w)}\right] + R_n\left(\frac{\bar{n}-n}{1-n}\right) + U_n \tag{3:4}$$

$$\frac{\dot{w}}{(1-w)^2} = -R_{wa}\left[\frac{Fw-a}{(1-w)(1-a)}\right] - R_{wn}\left[\frac{Dw-n}{(1-n)(1-w)}\right] + R_{wb}\left[\frac{Gb-w}{(1-w)(1-b)}\right]$$

$$+ R_w\left(\frac{\bar{w}-w}{1-w}\right) + U_w \tag{3:5}$$

44

$$[f_c C_c + f_n C_n + f_h C_h + f_w C_w]\dot{T} = (E_n R_{na} - E_a R_{an}) \left[\frac{An-a}{(1-n)(1-a)}\right] + (E_w R_{wa} - E_a R_{aw}) \left[\frac{Fw-a}{(1-w)(1-a)}\right]$$

$$+ (3E_b - E_a)R_{ab} \left[\frac{Cb^3 - a}{(1-b)^3(1-a)}\right] + (2E_b - E_s)R_{sb} \left[\frac{Bb^2 - s}{(1-b)^2(1-s)}\right]$$

$$+ (E_b R_{bw} - E_w R_{wb}) \left[\frac{Gb - w}{(1-w)(1-b)}\right] + (E_w R_{wn} - E_n R_{nw}) \left[\frac{Dw - n}{(1-n)(1-w)}\right]$$

$$- 2E_b R_b \frac{[\bar{b} - b]}{(1-b)} - E_n R_n \left(\frac{\bar{n}-n}{1-n}\right) - E_w R_w \left(\frac{\bar{w}-w}{1-w}\right)$$

$$+ jEF_e - (E_a U_a + E_b U_b + E_s U_s + E_n U_n + E_w U_w) \tag{3:6}$$

$$\dot{I}'_{\gamma J} = (\alpha_{\gamma J} - \beta_{\gamma J})cI'_{\gamma J} + \varepsilon_{\gamma J} cP_{\gamma J} + K''cI_o \tag{3:7}$$

where

$$\dot{a} \equiv v \frac{da}{dx} \tag{3:8}$$

In the last expression v is the gas flow velocity and x is the downstream distance from the laser cavity entrance. These rate equations agree in essence with those derived by Lyon,[22] by Granek,[23] and by Harrach and Einwohner.[24] The individual symbols are explained in Appendix A, Nomenclature.

The collisional relaxation terms contain a factor $R_{\alpha\beta}$ for VV relaxation of the α mode due to collisions with molecules of species β. Similarly the factor R_α describes VT relaxation of the α mode. In Eq. (3:3) the first and third factors of 2 arise from the double degeneracy of the CO_2 bending mode. The factor of 3 arises from the exchange of one ASM equation for three BM quanta, while the second factor of 2 arises from the exchange of one SSM quantum for two BM quanta. All other energy exchanges involve one quantum transitions. Similar reasons explain the

45

multiplicative factors of 2 and 3 in Eq. (3:6). Each collisional relaxation rate constant was given by a three-parameter temperature-dependent expression which was fitted to the measured values given in the work of Taylor and Bitterman,[25] or estimated on the basis of physical arguments. The details of this parameterization and temperature plots of the 24 rate constants used in the laser kinetics model are given in Appendix B, Collisional Relaxation.

The percentage of the input electrical power which excites the various vibrational modes and electronic levels was calculated from the Boltzmann equation as a function of E/N by Lowke et al.[16] By separating the combined vibrational levels according to their degeneracies, the results given in Fig. 3:3 were obtained for a 1:7:20:0.07 mixture of $CO_2:N_2:He:H_2O$. Excitation of the water vibrational mode at concentrations below 1% is too low to be considered. The curves indicate that an E/N value of about 2×10^{-16} V-cm^2 is near optimum for the electrical excitation of the nitrogen. The electrical pumping rates of the various vibrational modes are denoted by U_α in the rate equations and are easily derived from Fig. 3:3. The details of the derivation are given in Appendix C, Electrical Excitation.

The gas temperature was determined from the nonstationary equation of thermal conductivity, Eq. (3:6). The bracketed term on the left-hand side of the equation contains the specific heats of the gas components at constant pressure weighted by their respective molar densities. The first three lines on the right-hand side contain the energy defect heating terms from VV transitions, while the fourth line contains the VT heating terms. The first term of the last line arises from gas heating by the discharge. This term is modified by a factor F_e which accounts for the portion of electronic excitation which directly heats the gas rather than relaxing through photon emission. The following set of terms in parentheses subtracts that portion of the electrical discharge energy which goes directly into vibrational excitation. A detailed explanation of this equation is given in Appendix D, Gas Heating.
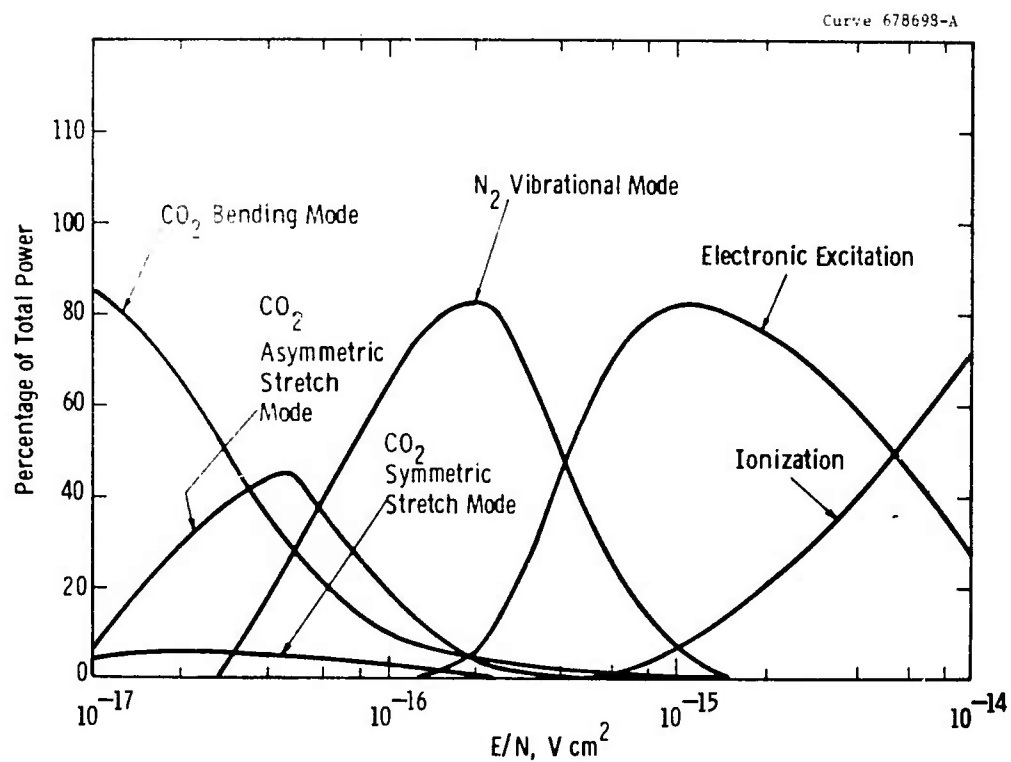
46

Fig. 3:3 Percentage of electrical input power transferred
to vibrational modes, electronic levels, and
ionization for a 1:7:20 mixture of $CO_2:N_2:He$.

47

The equations and terms described thus far are sufficient to accurately describe the small-signal gain. However, if there is significant stimulated emission present, the stimulated emission rate Γ in Eqs. (3:1) and (3:2) and the gain Eq. (3:7) must also be considered. The latter equation describes the radiation intensity $I'_{\gamma J}$ collimated by the resonator mirrors where the subscript specifies the particular vibrational-rotational transition being considered. This radiation is the result of stimulated emission and is the final output of the laser. The first term on the right-hand side arises from the net gain of the medium where $\alpha_{\gamma J}$ is the total gain and $\beta_{\gamma J}$ is the averaged loss per unit length. The averaged loss includes all mirror losses, including mirror transmissivities, and scattering losses within the gas medium. This loss term is frequently called the cavity gain[26] and is the gain at which a steady state laser will operate. The second term on the right-hand side accounts for the spontaneous emission which initiates the laser process, and the last term represents irradiation of the laser medium by an external source of intensity I_o, in the event that the gain medium is employed as an amplifier driven by an external laser oscillator. The stimulated emission rate is fully explained in Appendix E, Stimulated Emission, and the calculation of the radiation intensity is described in Appendix F, Radiation Intensity.

The harmonic oscillator, six-temperature Boltzmann equilibrium laser kinetics model is described fully by these seven simultaneous differential equations. This system of equations was integrated numerically in constant integration steps by the Euler method[27] to obtain the behavior of the laser quantities as a function of their downstream location. A typical computer calculation took 40 minutes on the U-1106 computer for a laser cavity 20 cm wide. The laser cavity was considered to have a rectangular cross-section and to be at least as large as the discharge region (see Fig. 3:4). The mirrors were assumed to be plane-parallel rectangular mirrors along the sides of the discharge region and large enough to assure that the entire discharge region was part of the resonant cavity. These assumptions simplify the model but are not fundamental limitations. The solution of these equations yielded considerable information about the operation of the CO_2 COFFEE laser, including
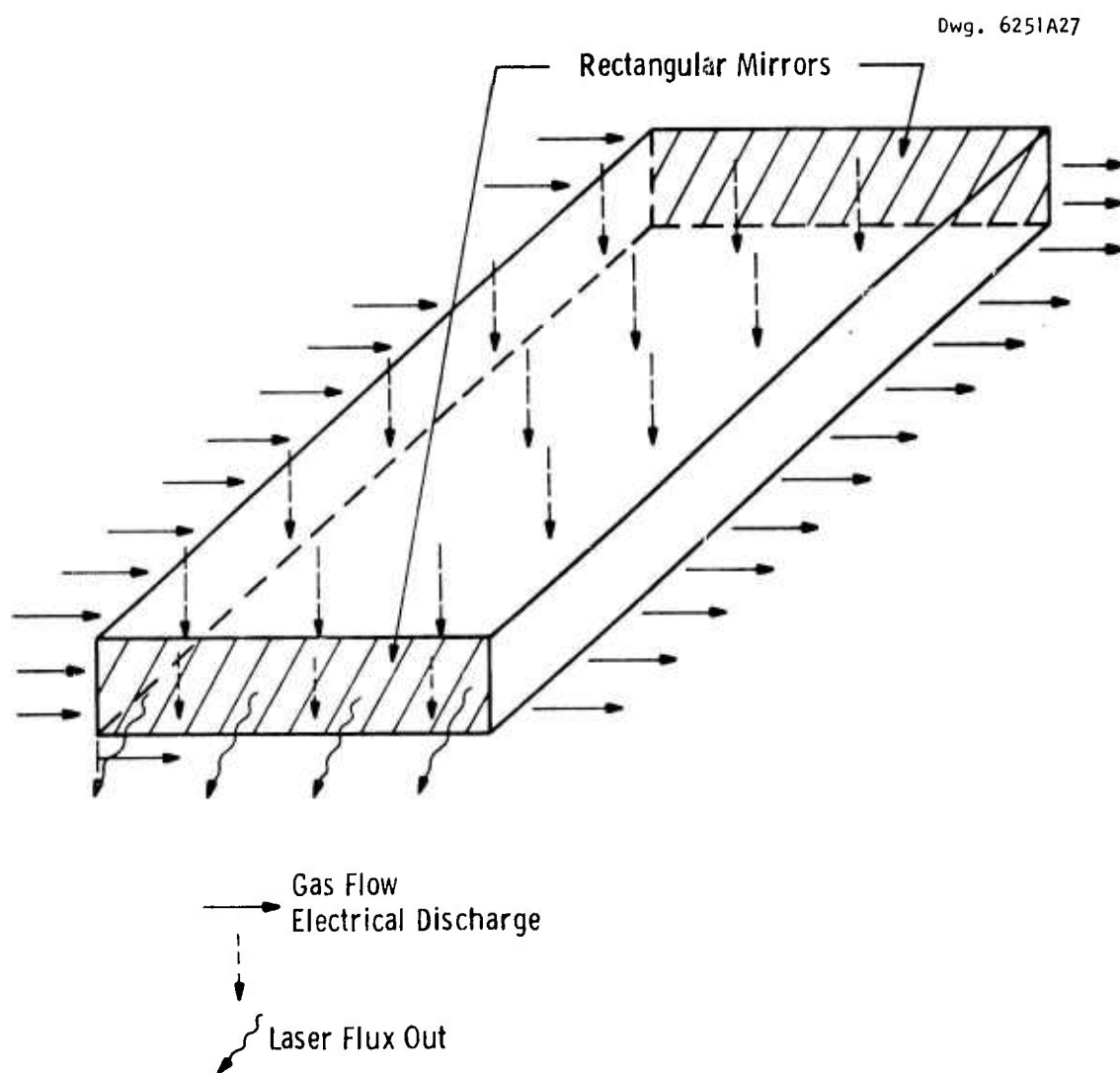
48

Dwg. 6251A27

Fig. 3:4 Schematic diagram of the laser cavity.

49

the small-signal gain and laser output power. Examples of the information obtained from these calculations and how this information has enhanced our understanding of the COFFEE laser operation are given in the next section.

3.1.4 Results

A good method for testing a laser kinetics model and computer code is to compare the theoretical calculations with the measured values for typical causes. However, care must be taken to include significant amounts of all the gas components and to include all significant collisional relaxation processes. The case must also be in a regime where the experiment can be monitored accurately and reliably. The conditions chosen were a 280 Torr, 1:7:20 laser mixture of $CO_2:N_2:He$ with 2 Torr of H_2 in a laser cavity 11 cm along the gas flow direction, 10 cm long (in the direction between the mirrors), and having an 8 cm gap between the electrodes (i.e., a laser cavity volume, V, of about 1 ℓ). The small-signal gain was measured for these conditions for a total electrode current of 1.0A and 1.5A with entering flow velocities of 149 and 148 m/sec, respectively.

The steady-state electric field and current density distributions measured for total currents of 1.0A and 1.5A are shown in Figs. 3:5 and 3:6. The interelectrode current density associated with each cathode pin was determined by measuring the current to each pin and assuming that the current spreads uniformly to occupy a 1 cm^2 area which corresponds to half of the distance to the next pin in each direction (pin density = 1 pin/cm^2). The current density and electric field are arbitrarily taken to be zero 0.5 cm before and after the discharge region as defined by the cathode. This cutoff procedure may be slightly too abrupt, but it shouldn't affect the general results. The pin currents were experimentally adjusted to increase with downstream distance, as the electric field decreased, in an attempt to keep a constant input power density into the gas.
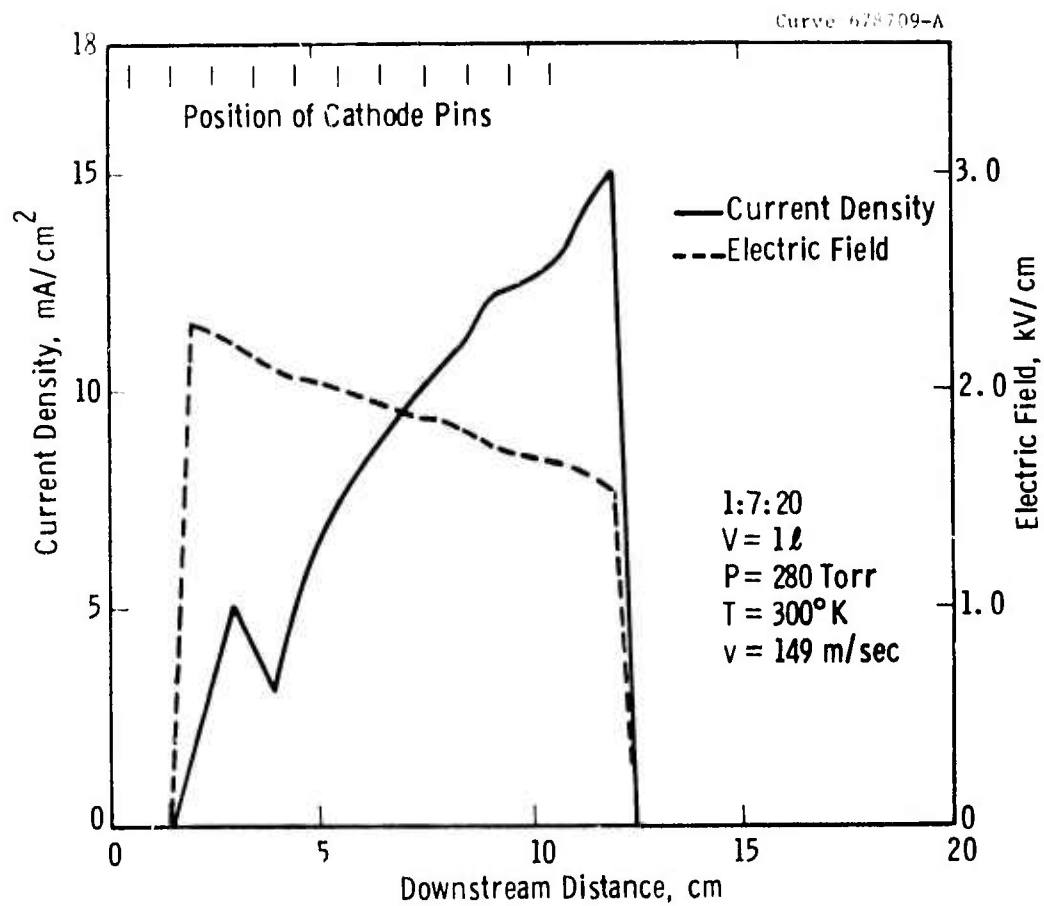
Fig. 3:5 Measured current density and electric field for
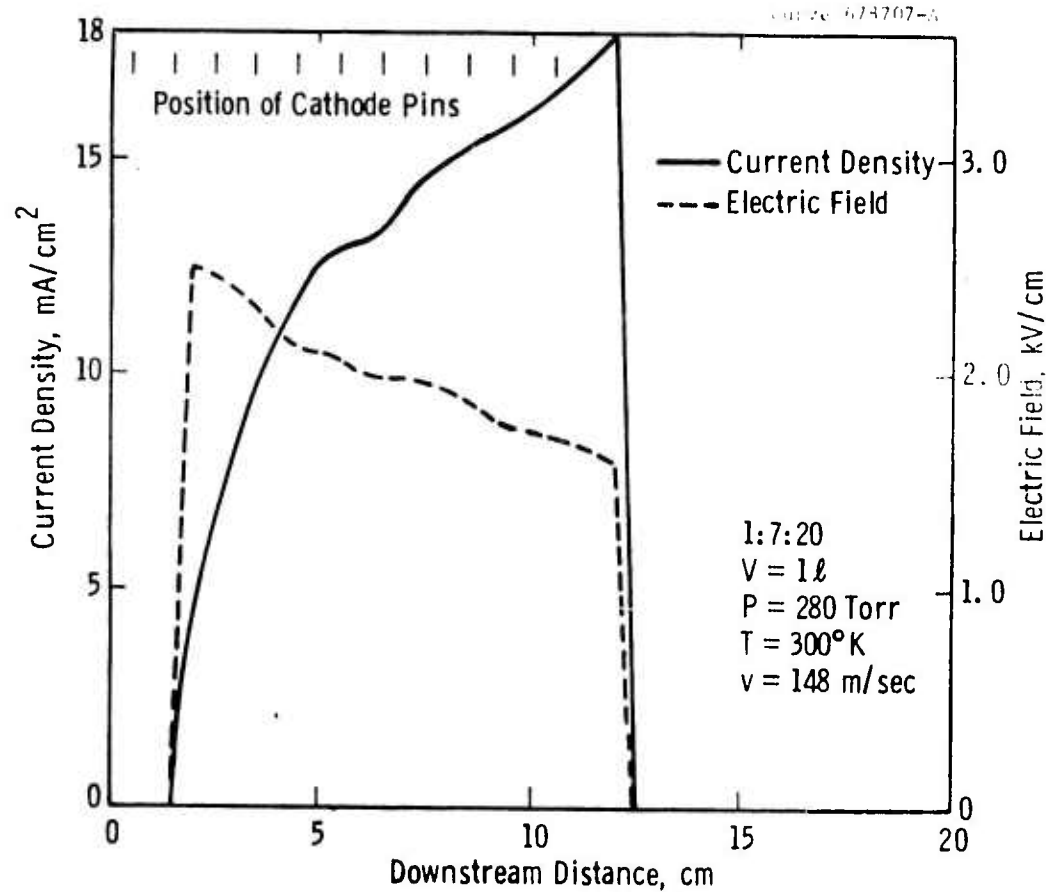a current of 1.0 A.

51

Fig. 3:6 Measured current density and electric field for
a current of 1.5 A.

52

The current density and electric field distributions shown in Figs. 3:5 and 3:6 are for the midplane between the cathode pins and the anode plate where the small-signal gain was measured. These distribution plots were purposely shifted 1.5 cm downstream from the x origin (x = 0 at 0.5 cm upstream from the first row of pins) in order to match the location of the calculated peak gain with that of the measured peak gain (see Figs. 3:7 and 3:8). The relative locations of the rows of pins are shown in the figures. The shift at the midplane in the distributions can be explained by a vector combination of the ion drift velocity and the gas flow velocity. A simple calculation predicts a 2 cm displacement in the flow direction of the glow discharge at the midplane which agrees reasonably well with the 1.5 cm shift required to match the calculated and measured gain distributions. (See Section 2.3.)

The measured current density and electric field distributions allow two cases to be calculated: the small-signal case when mirrors are not present and the large-signal case when mirrors are present. In the former case detailed experimental measurements of small-signal gain were taken at 1.0A and 1.5A for comparison purposes. However, in the latter case experimental measurements with laser output were not made because the discharge module was only 10 cm long. Nevertheless, it was informative to predict the laser performance using the current density and electric field distributions measured at 1.5A. For these lasing calculations the assumed cavity length was 140 cm and the cavity width and electrode gap were kept at 11 cm and 8 cm, respectively, giving a cavity volume of about 12 ℓ and total currents of 14A and 21A corresponding to the 1.0A and 1.5A currents of the smaller cavity. The mirrors were assumed to be plane-parallel sheet mirrors which formed the two ends of the cavity (sides of flow channel), with one mirror having a transmissivity of 0% and the other 15%. The absorption and scattering losses were taken to be 1.5% at each mirror and 0.01% cm^{-1} within the gaseous discharge.

The small-signal gain results for the P(22) transition are shown
in Figs. 3:7 and 3:8. The calculated small-signal gains are obviously
too high if no water vapor is included in the gas mixture, whereas they
agree very well with the experimental values when the gas mixture is
assumed to contain 0.25% water vapor, i.e., a 1:7:20:0.07 gas mixture
of CO_2:N_2:He:H_2O. The theoretical and experimental values agree
particularly well in the region of peak gain where the experimental values
are most accurate. We will therefore use 0.25% water vapor in the
theoretical calculations.

In Fig. 3:7 the bump in the gain curve for x between 3 and 4
cm is a result of the dip in the current density distribution shown in
Fig. 3:5. This slight dip for the 1A case resulted from using the row
ballast resistance values which were optimized for 1.5A operation.
Typical collisional decay times for the 1.5A test are given in Fig. 3:2
and were considerably shorter than those exhibited in Figs. 3:7 and 3:8.
The apparent difference between these results is easily explained by an
examination of the basic rate Eqs. (3:1-3:5). The decay times in
Fig. 3:2 are the reciprocals of the collisional transition rates R_α and
$R_{\alpha \beta}$ whereas the decay times exhibited in Figs. 3:7 and 3:8 are the result
of the entire terms in the rate equations, i.e., they include the effects
of back rates and reduced transition probabilities due to elevated
vibrational temperatures which increase the populations of the upper
energy levels. However, the decay times given in Fig. 3:2 effectively
show that water vapor decreases the small-signal gain by depopulating
the excited nitrogen more effectively, relative to other depopulation
mechanisms, than it does the CO_2 bending mode.

The large-signal gain results in Figs. 3:7 and 3:8 follow the
small-signal gain until the onset of lasing (at 6.5 cm for the 14A case
and at 4.5 cm for the 21A case). At that location the gain falls to a
cavity gain value of 0.074% cm^{-1} as determined by the assumed cavity
losses. Finally, at x = 12.0 cm the gas leaves the discharge region;
lasing ceases, and the remaining gain decreases exponentially due to
collisional deactivation. The large-signal gain calculation thus predicts
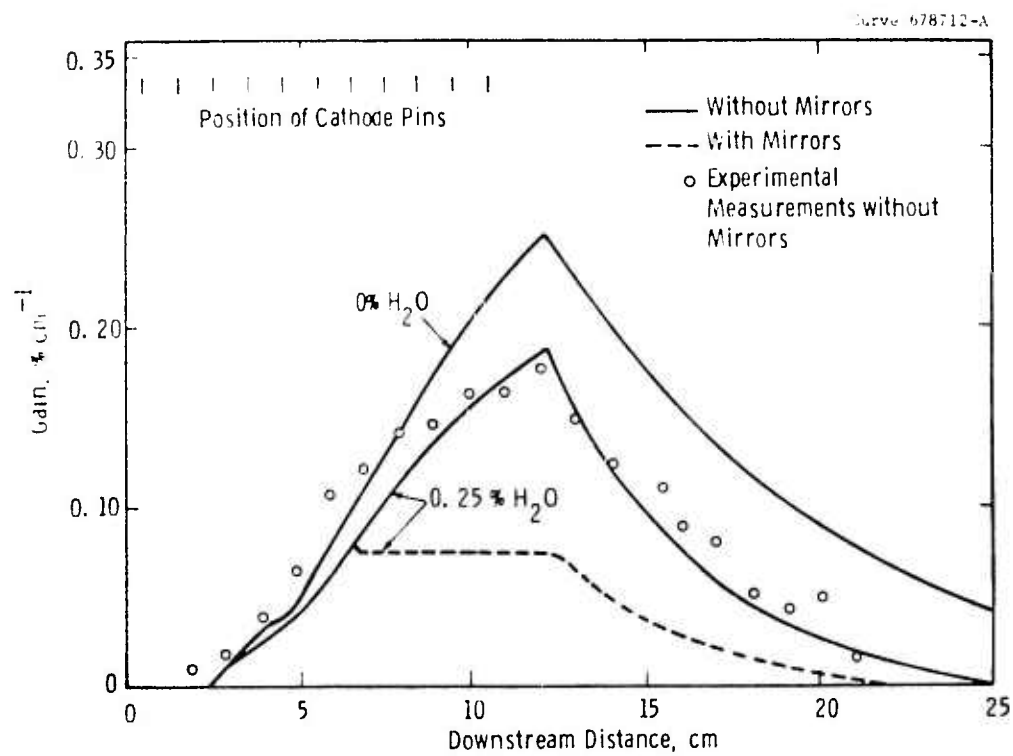
54

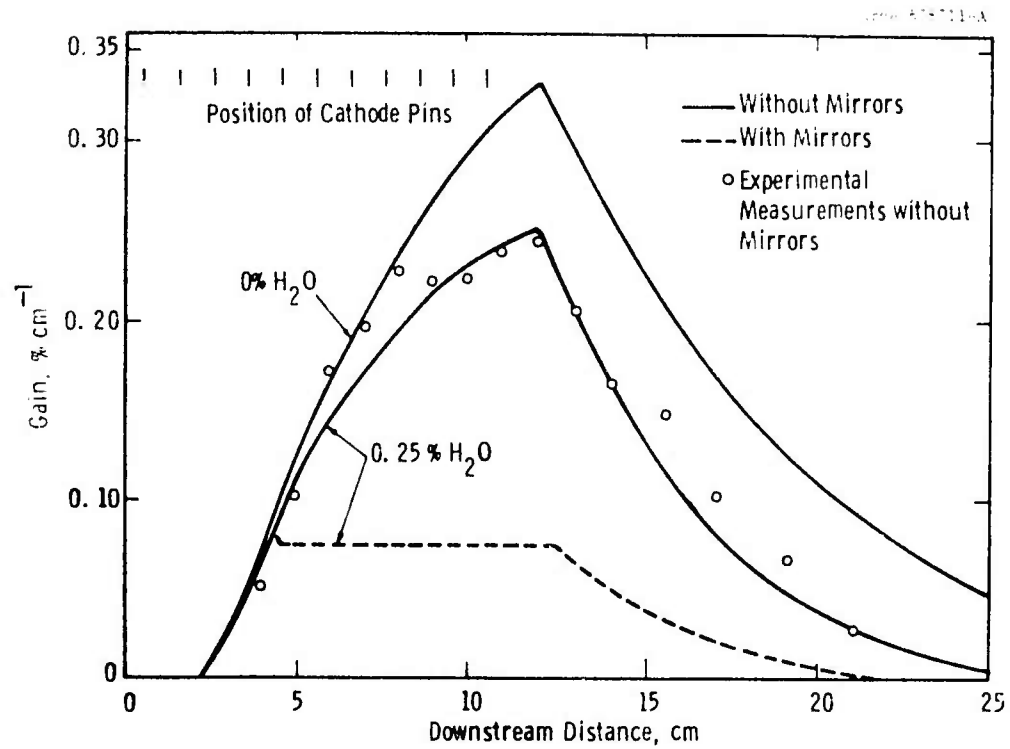Fig. 3:7   Computed variation of gain for a current of 1.0 A.

Fig. 3:8 Computed variation of gain for a current of 1.5 A.

laser output extending from $x = 6.5$ cm to 12.0 cm for the 14A case and from $x = 4.5$ cm to 12.0 cm for the 21A case. The shorter lasing interval for the 14A case is expected from the lower electrical pumping rate; that is, it takes longer and, therefore, more distance to achieve the same amount of pumping as for a current of 21A. However, the shutoff of the lasing radiation generally occurs at the same location because the gain is at the cavity threshold value (gain = losses) irrespective of the current value. Any small decrease below this threshold gain, in this instance due to rapid fall-off of discharge current, means that the gas becomes primarily on absorptive medium for the lasing radiation, thereby quickly dissipating the laser radiation. These predicted performance features appear to be quite reasonable and provide a good basis for guiding future lasing experiments.

Although the theoretical and experimental small-signal gain values agree well, a discrepancy is apparent when the two gas mixes are compared. The total pressure was 280 Torr in both cases; however, the theoretical model assumed that the gas mixture contained 0.7 Torr H_2O and no H_2, whereas in the experiments 2.0 Torr H_2 and no H_2O were added to the initial gas mixture. This discrepancy may be better understood by comparing the peak gains calculated as a function of H_2O concentration with the peak gains measured as a function of H_2 concentration as shown in Fig. 3:9. (For brevity only the 1.5A or 21A case, unless stated otherwise, will be considered in the remainder of this section.) The experimental value at 0% H_2 has not been included in the straight line fit to the experimental data because it was measured with fresh gas (the gas had not yet been recycled many times) in a cool system whereas the other measurements were made with old gas (the gas had been recycled many times) in a warm system. The gain of fresh gas was always higher than that of old gas. The extrapolated peak gain at 0% H_2, as shown by the dotted lines, corresponds to 0.15% H_2O. This suggests that the experimental gas mixtures always contained a background impurity H_2O concentration of 1.5%, a value which is not unreasonable. However, the calculated and measured small-signal gain values agreed best when 0.25%
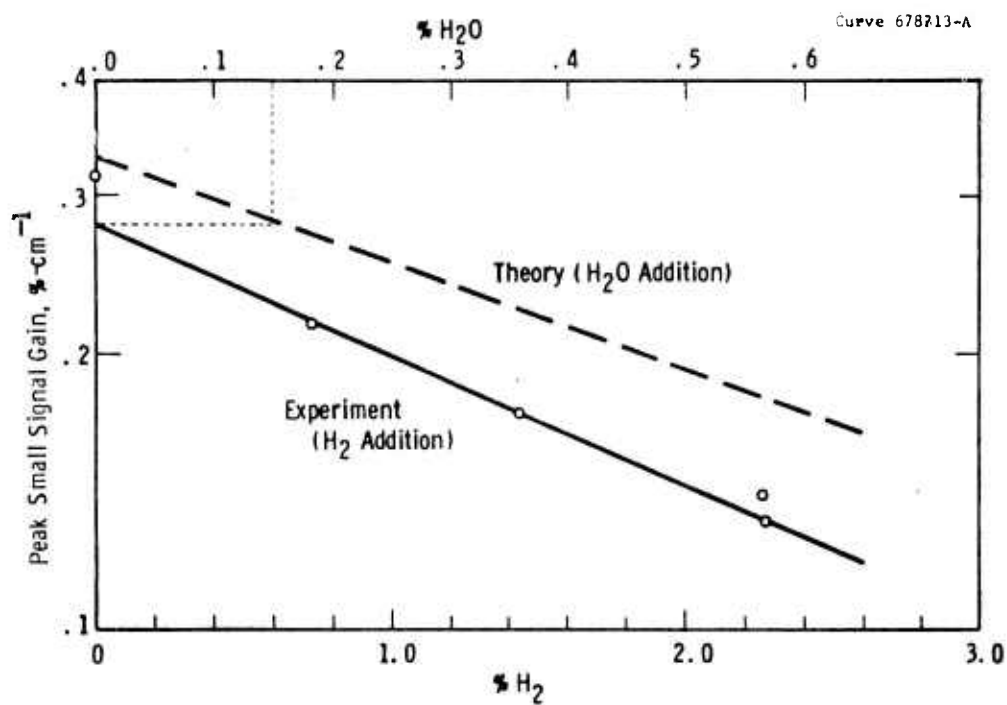
57

Fig. 3:9   Small-signal gain as a function of hydrogen and
           water vapor concentration at 280 Torr gas pressure
           and 1.5 A discharge current.

H_2O was included in the theoretical model. The need for assuming a larger H_2O concentration can be explained either by assuming that the collisional relaxation rates of H_2O and H_2 are simply scalable, or by assuming that a chemical reaction occurs whereby some of the H_2 is converted to H_2O. If the background H_2O concentration is 0.15%, Fig. 3:9 shows that 3.2 times as much H_2 is needed to produce the same effect as a given amount of H_2O. On the other hand, a comparison of the measured relaxation rates[25] shows that H_2O is 8.0 times more effective than H_2 in relaxing the CO_2 asymmetric stretch mode to the CO_2 bending mode, which, compared to competing mechanisms, is the most important process for the small-signal gain. Although the numbers are admittedly approximate, they seem to indicate that the results in Figs. 3:7 and 3:8 cannot be achieved by a simple scaling of the H_2 and H_2O relaxation rates.

The other possible explanation is that part of the H_2 was chemically converted to H_2O. By assuming a background of 0.15% H_2O, this requires that an additional 0.1% H_2O was produced by chemical conversion. This implies that 14% of the H_2 concentration in the experimental gas underwent chemical conversion to H_2O, and that the remaining H_2, because of its lower collisional relaxation rates, had no significant effect on the laser kinetics. A 14% conversion factor is reasonable and gives strong support to the hypothesis that important chemical reactions occur in the gas flowing through the discharge.

To be efficient a laser must have good pumping properties. One such desirable property is to have a uniform electrical power density deposited into the gas (due to gain spikes and gas temperature effects downstream, a constant input power density may not be the optimum design, but it is still a good design). The measured power density distribution with no mirrors is shown in Fig. 3:10 for the 1.5A case in which the row ballast resistors were chosen to produce a uniform input power density. The resulting $j \cdot E$ distribution was very uniform in the downstream direction through the optical cavity. This illustrates one of the unique features of the COFFEE laser electrical excitation concept.
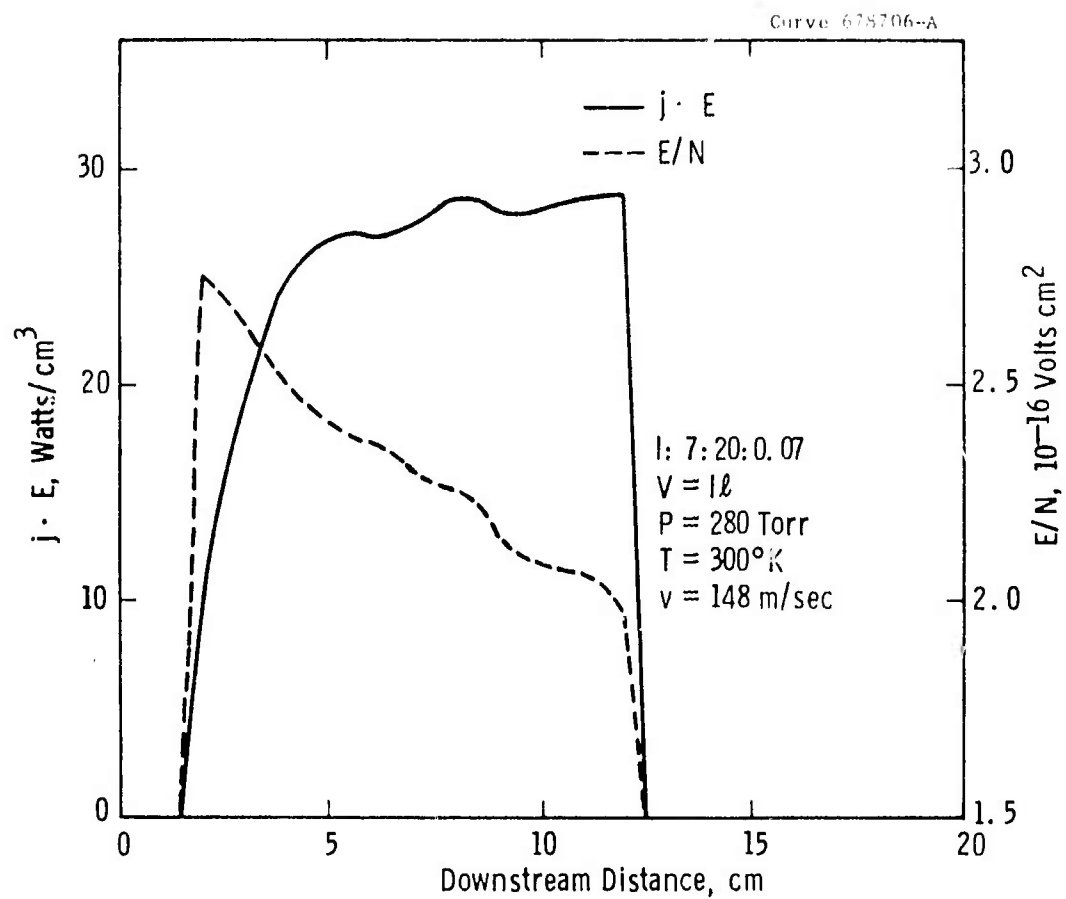
Fig. 3:10 Electrical power density and E/N variation
during small-signal gain measurements for
a current of 1.5 A.

Another important pumping property is to operate at the value of E/N for which maximum power is deposited in the proper molecular excitations. Reference to Fig. 3:3 shows that for a 1:7:20 gas mixture, the optimum E/N value for the N_2 excitation is 2.0×10^{-16} V-cm^2. By using the experimental values of electric field (see Fig. 3:6) and calculating the value of N as the gas flows downstream and its temperature increases, the E/N values can be determined as a function of x as shown in Fig. 3:10. The COFFEE laser clearly operates very near the optimum value with 75 to 83% of the electrical power being deposited in the N_2 vibrational mode. This operating condition is better than that of non-flowing CO_2:N_2:He:H_2O self-sustained electrical discharges where the predicted E/N value must be a constant 3.0×10^{-16} V cm^2 with 68% of the electrical power being deposited in the N_2 vibrational mode.

The combination of uniform power density deposition and excellent E/N operating values means that the COFFEE laser operates at near optimum pumping efficiencies throughout the optical cavity. Although the currents and electric fields were measured during the small-signal gain experiments, the addition of mirrors should have a minor effect, and the basic conclusion of near optimum pumping efficiencies should remain valid.

The gas temperature is important because the collisional relaxation processes are strongly dependent upon it. The temperature distributions with and without mirrors are shown in Fig. 3:11 where a typical starting temperature of 300°K is assumed. (The gas flow velocity is proportional to the gas temperature and therefore Fig. 3:11 is also a plot of the flow velocity when 300°K is replaced by 148 m/sec and 340°K is replaced by 170 m/sec). The presence of mirrors markedly increases the gas temperature in the region of electrical excitation between x = 1.5 and 12.0 cm and decreases the temperature farther downstream. These features are easily understood by examining the interactions diagrammed in Fig. 3:2. In the small-signal case there are no significant 10.6 µm lasing transitions, and the relaxation of the CO_2 asymmetric mode to the CO_2 bending mode is by slow VV interactions. However, in the large signal case there are significant lasing transitions to the CO_2 symmetric mode which is closely coupled to the CO_2 bending mode. Thus in the electrical
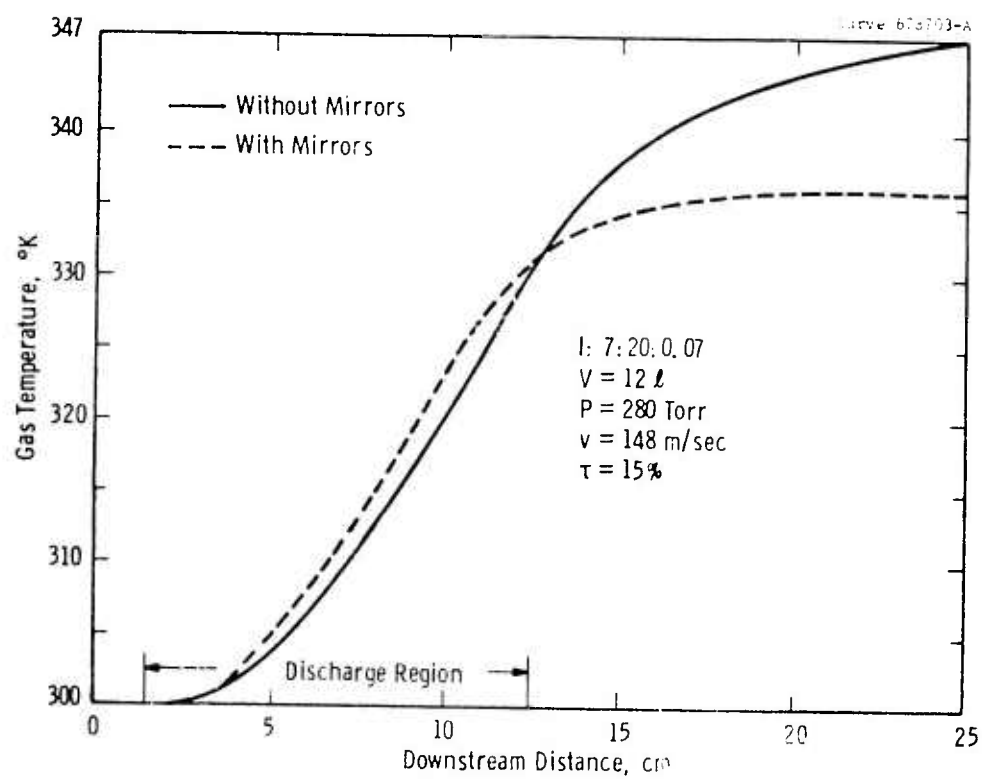
61

Fig. 3:11 Gas temperature variation with and without
mirrors.

62

excitation region, gas heating by VT relaxation of the CO_2 bending mode is low in the small-signal case and high in the large-signal case. In other words, the increased gas temperature is caused by the increased VT relaxation of the CO_2 bending mode. Eventually, however, the gas temperature in the small-signal case must exceed that in the large-signal case since the laser radiation energy in the latter case is not available to heat the gas.

The three sources of gas heating are VT and VV relaxation and direct heating by the electrical discharge. The first two sources occur by molecule-molecule collisions, whereas the latter source occurs by electron-molecule collisions. The contributions to the gas heating from these three sources are shown in Figs. 3:12 and 3:13. In both case the VV heating is small but understandably larger in the small-signal case, where VV relaxation is the only interaction between the asymmetric and bending modes of CO_2. The electrical discharge contribution is a function of only the current and voltage distributions, and is, therefore, the same for both cases. The VT relaxation collisions give the largest contribution, which is the same for the two cases until the laser output is initiated at $x = 4.5$ cm. As explained in the previous paragraph, the laser radiation effectively increases the CO_2 bending mode VT relaxation, thereby heating the gas. This effect is clearly seen in these two figures.

The vibrational mode Boltzmann temperatures for the small and large-signal cases are plotted in Figs. 3:14 and 3:15. As expected, the CO_2 asymmetric mode and N_2 vibrational mode are in close equilibration as are the H_2O bending mode and the CO_2 symmetric stretch and bending modes. In fact, the latter three modes are in such close equilibration that their temperatures cannot be separated in the figures. In Fig. 3:15 the absence of any significant vibrational temperature increase in the region of lasing radiation from $x = 4.5$ to 12.0 cm indicates that the pumping power deposited into the N_2 vibrational mode and the CO_2 asymmetric stretch mode is being effectively removed by the laser cavity flux before it can increase the Boltzmann temperatures. This is a clearly desirable characteristic of a good laser.
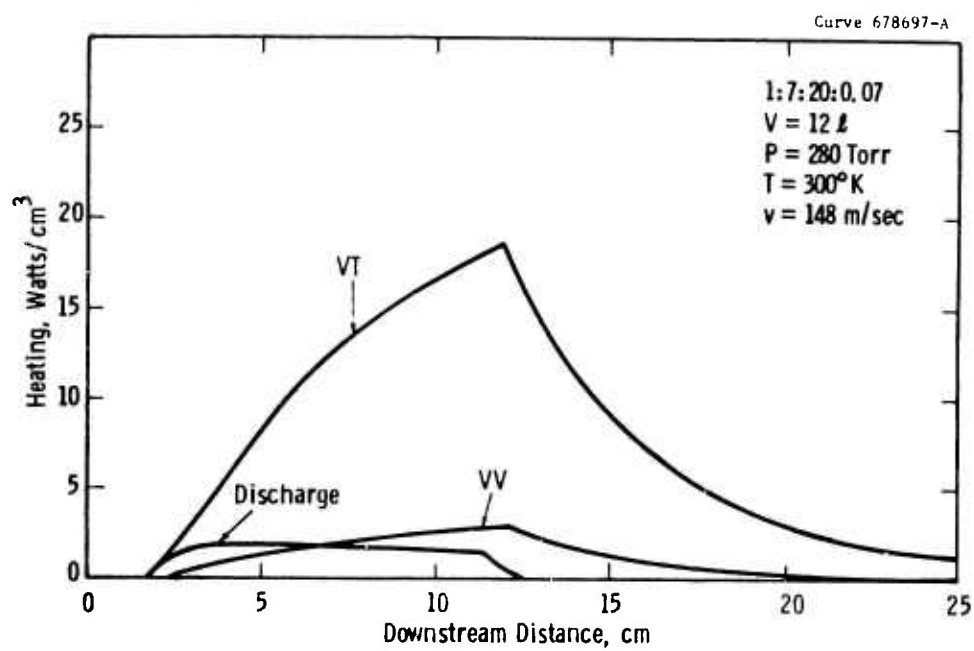
63

Fig. 3:12 Contributions to gas heating when mirrors
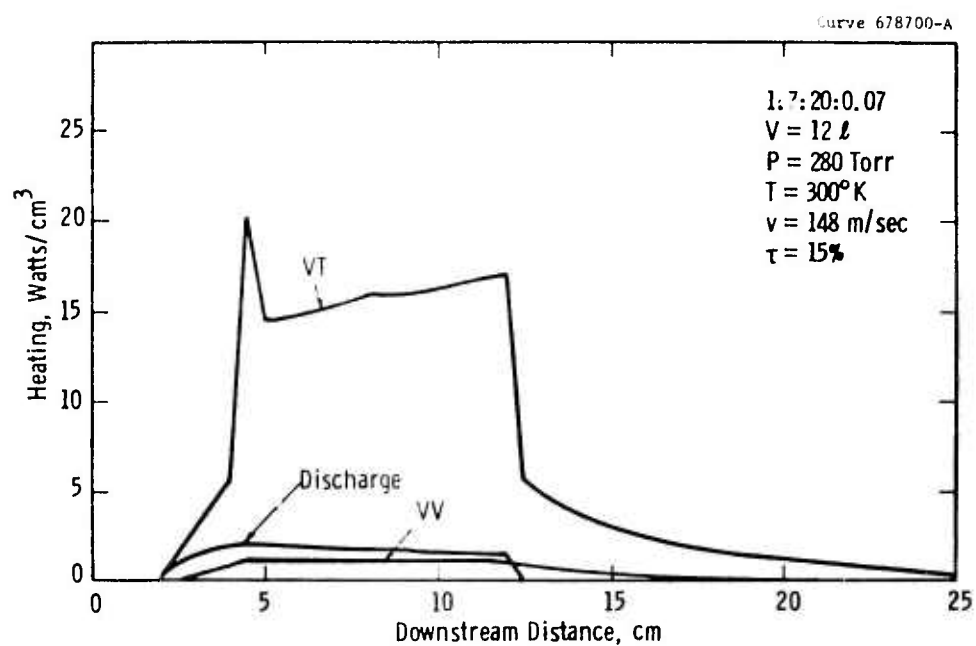are not present.

Fig. 3:13   Contributions to gas heating when mirrors
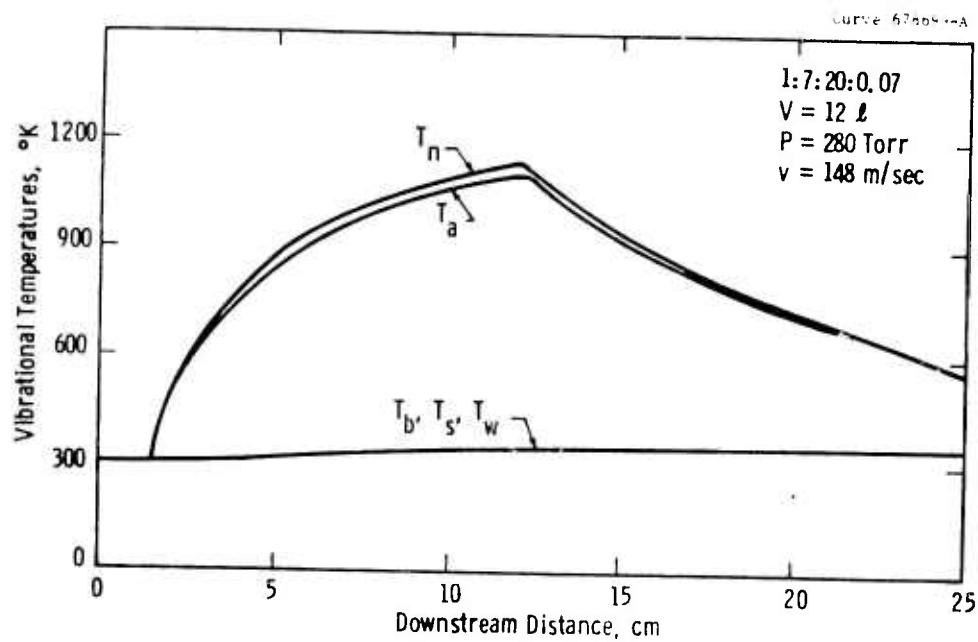   are present.

Fig. 3:14 Vibrational temperatures when mirrors are not present.
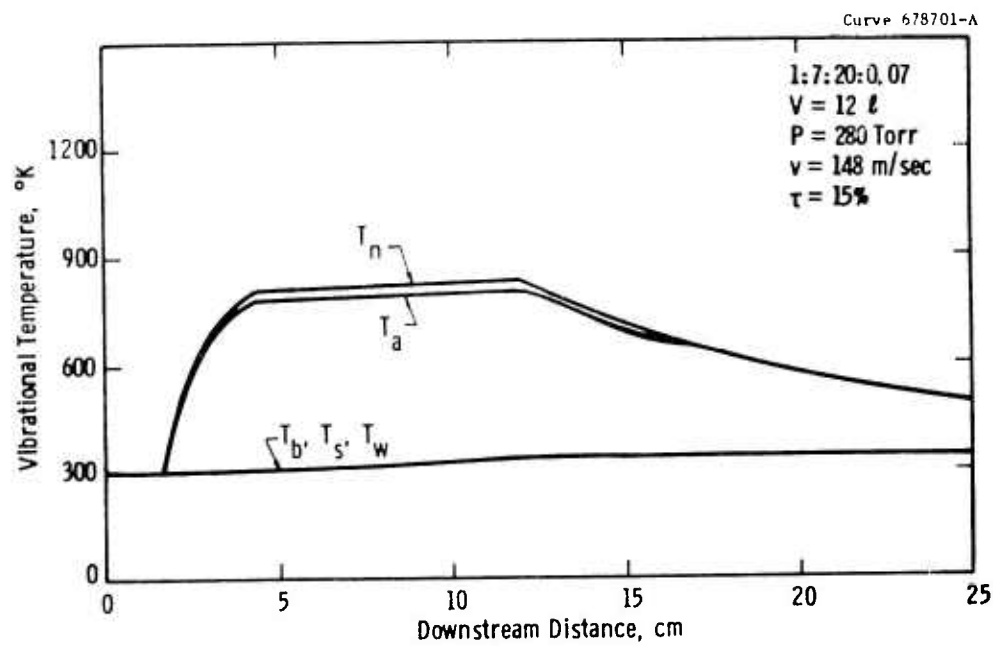
Fig. 3:15 Vibrational temperatures when mirrors are present.

67

Although the Boltzmann temperatures for the N_2 vibrational mode and the CO_2 asymmetric stretch mode are the important parameters in the laser kinetics model and are related to the amount of energy stored in the gas, a more directly meaningful quantity is the total energy density stored in these two modes which can be theoretically extracted at 10.6 µm, assuming one photon for each vibrational quantum. This quantity is plotted in Fig. 3:16. The small-signal case shows that the gas is still being effectively pumped at 12 cm although not as efficiently as at 4 cm where the slope is higher. The large-signal case shows, as in the previous figure, that in the region of lasing radiation, the pumping power deposited in the N_2 vibrational mode and in the CO_2 asymmetric stretch mode is being effectively removed by the laser cavity flux before it can increase the stored energy density. From this figure it can be determined that 14.1 kW of theoretically extractable radiation power remains in the gas beyond the region of electrical excitation, although all of this energy can never be extracted in a real laser.

The integrated output efficiency and power are shown in Fig. 3:17. The final output power of 45.4 kW is at an efficiency of 15.2% but the efficiency and output power are both increasing at the end of the electrical excitation region. This indicates that the COFFEE laser's output power and efficiency can be increased by simply extending the excitation region beyond the present 11 cm. This is also seen in Fig. 3:11 which shows that the present COFFEE laser is not temperature limited since the 335°K is well below the 450°K at which the laser performance starts to degrade due to collisional deactivation. Furthermore, the 14.1 kW of theoretically extractable output power which remains in the gas past the excitation region (see Fig. 3:16) is virtually independent of the excitation region size and is difficult to recover experimentally. Thus, an excitation region extended in the flow direction lowers the relative power loss in the gas leaving the excitation region, thereby increasing the efficiency.
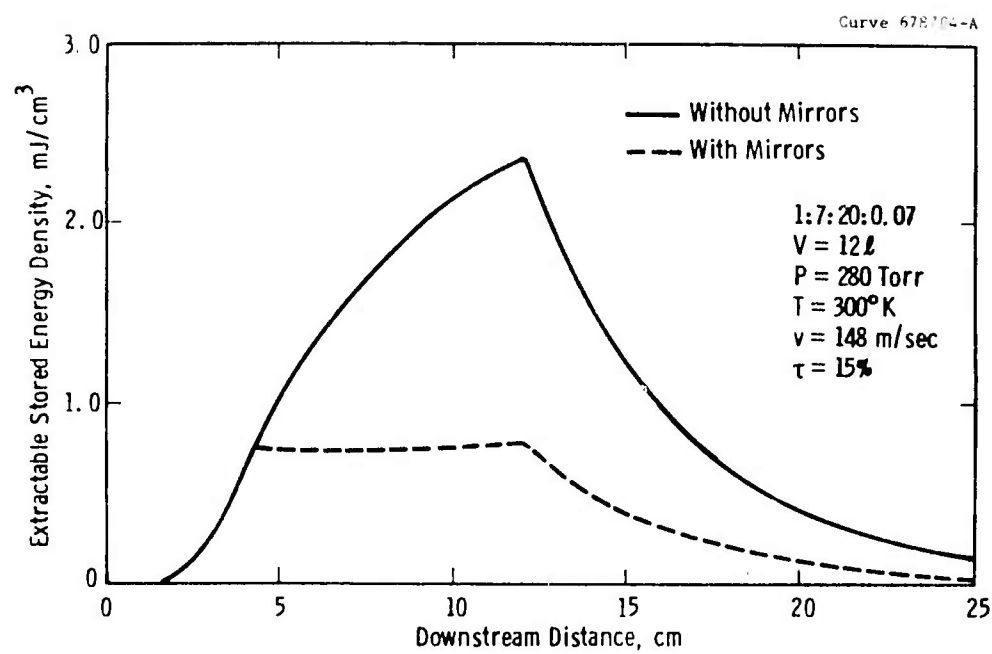
Curve 678704-A

Fig. 3:16   Extractable stored energy density with and
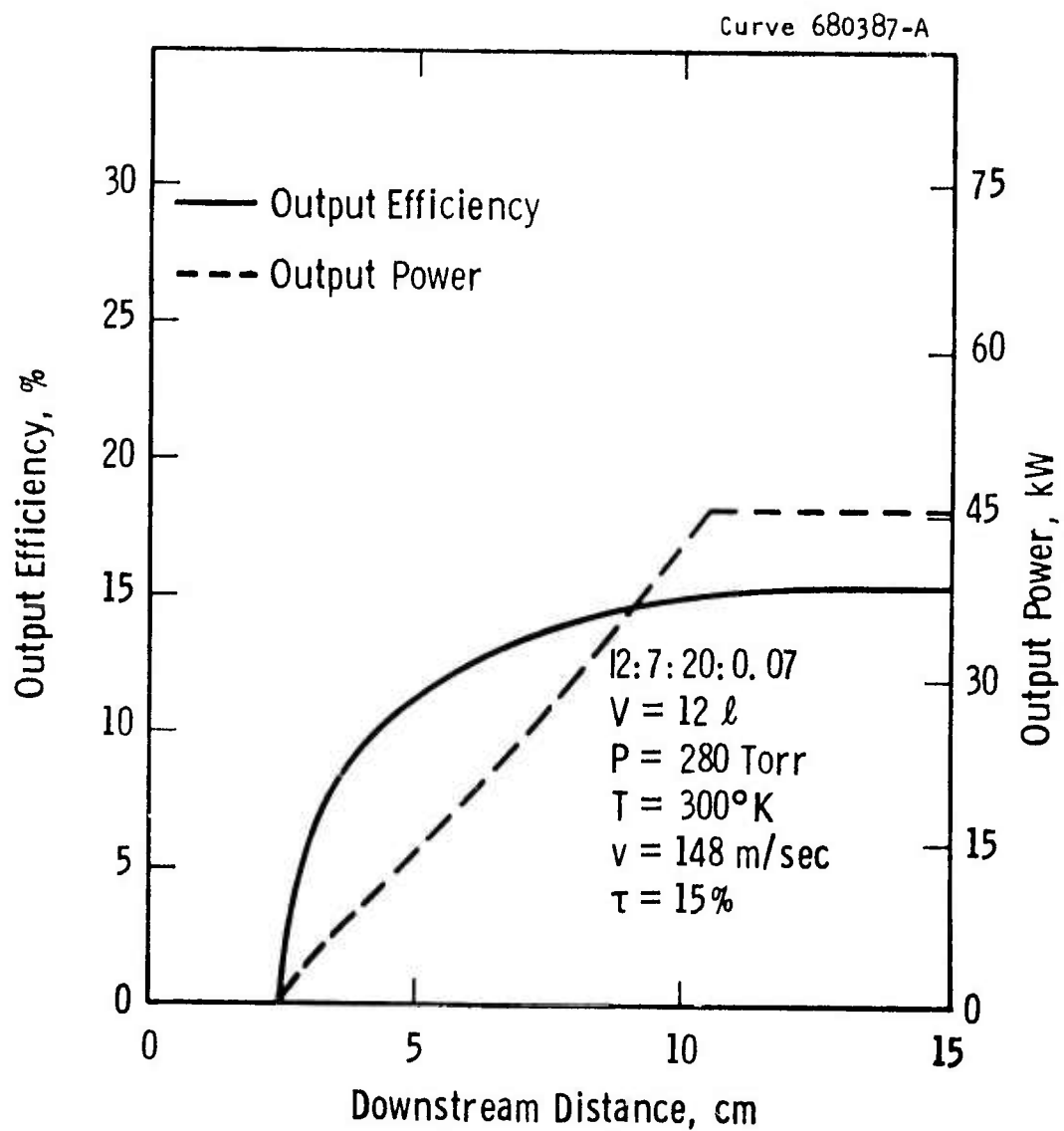   without mirrors.

69

Fig. 3:17   The calculated output power and efficiency for
a current of 21 amps.

70

The laser output intensities for both the 14A and 21A cases
are shown in Fig. 3:18. The output shows a gain spike at the onset of
the laser radiation region which occurs much farther downstream in the
14A case due to the lower electrical pumping rate. Of course the gain
spike is very narrow, thereby containing very little power, and will only
be seen in an oscillator with plane-parallel mirrors. The radiation
intensity increases beyond this gain spike until the electrical excitation
is abruptly ended at 12.0 cm. Combined with plane-parallel sheet mirrors
which are as high and as long as the electrical excitation region
(8 x 11 x 140 cm), these results predict a power output of 45 kW at 15.2%
electrical to optical output efficiency for the 21A case, and a power
output of 21 kW at 11.4% output efficiency for the 14A case.

All the results given heretofore are for a total pressure of
280 Torr, but this value may not be the optimum pressure. The output
efficiency and power dependence on the pressure is shown in Fig. 3:19
for the 14A case. The efficiency has a peak of 16.6% at 90 Torr and
decreases to 10.7% at 300 Torr. At high pressures the efficiency
decreases very slowly while the output power continues to increase at a
large rate. Thus, an efficient laser using the 1:7:20 gas mixture
should operate at 90 Torr and a high power laser should operate at high
pressures.

All of these results are for mirror transmissivities of 0% and
15% with absorption and scattering losses of 1.5% at each mirror. The
output power and efficiency depend on the mirror transmissivity and this
dependence is shown in Fig. 3:20 for a current of 21A. These results are
obtained by changing only the transmissivity of the 15% mirror. A rather
broad peak occurs between 10% and 15% which indicates that the previous
results in this section are for the near optimum laser output coupling
of 15%.

A laser should operate with a radiation intensity within the
cavity which is sufficiently large to depopulate the upper laser level
by stimulated emission as quickly as it is populated (although a steady-
state population may exist). The previous results for vibrational
temperatures and extractable stored energy show that the COFFEE laser is

71
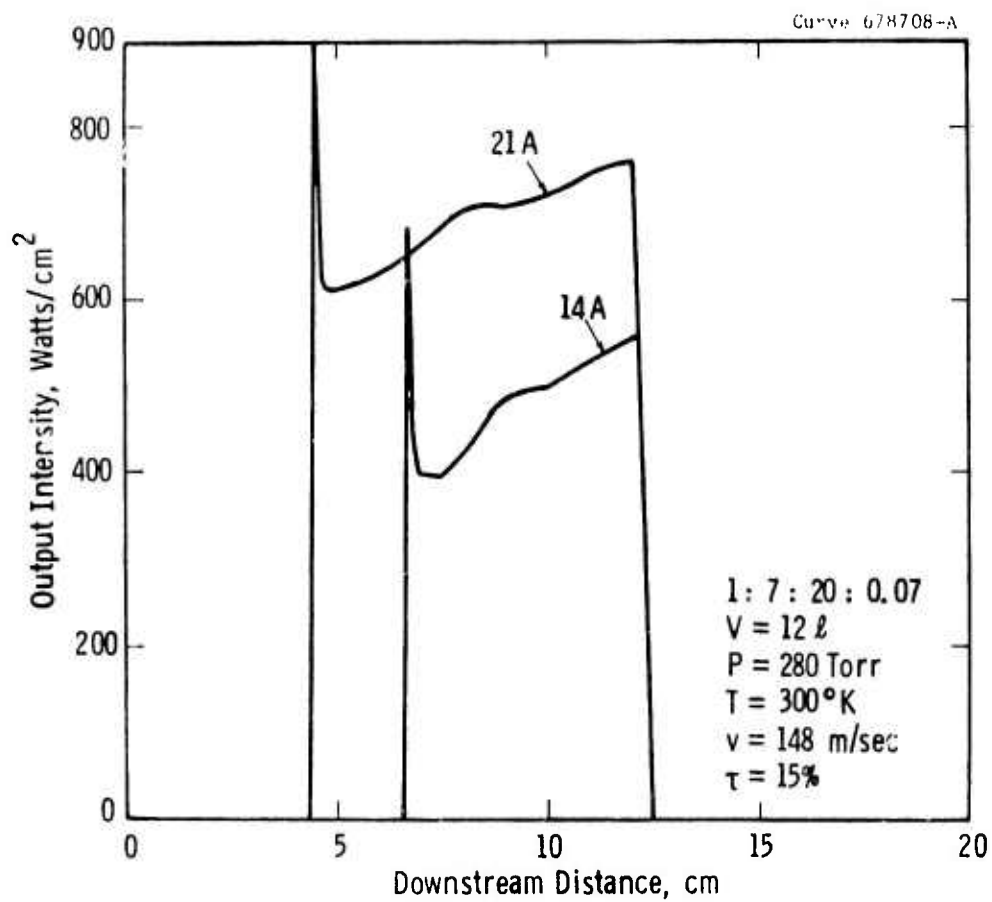
Fig. 3:18 Calculated laser output intensities for currents
of 14 and 21 A.
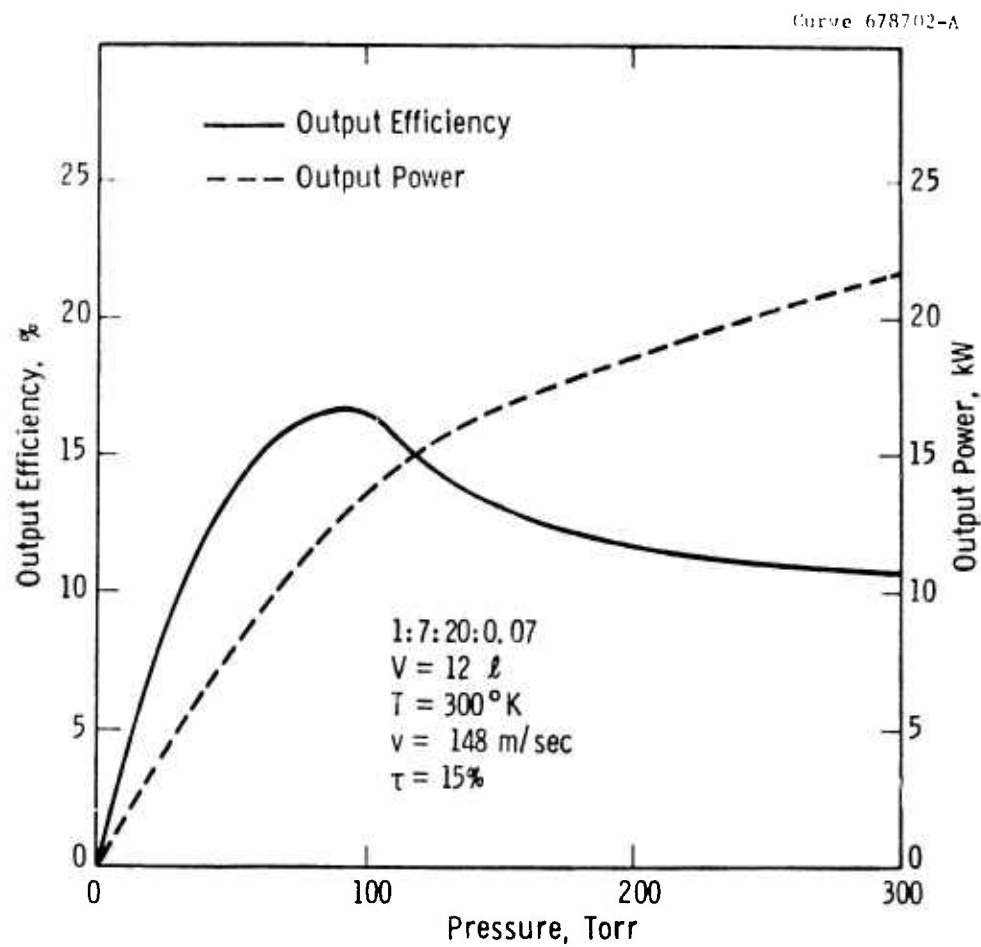
Fig. 3:19 The calculated pressure dependence of the output
power and efficiency for a current of 14 A.

Curve 678710-A
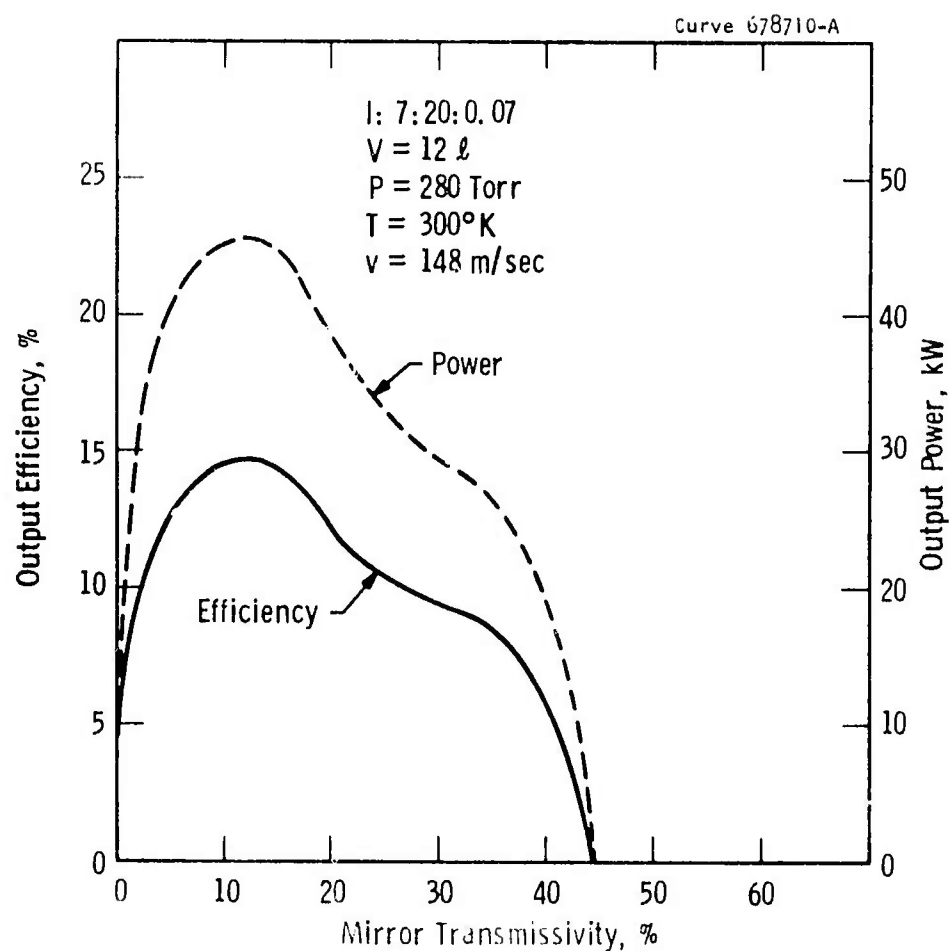
Fig. 3:20 The mirror transmissivity dependence of the
calculated output power and efficiency for
a current of 21 amp.

74

Curve 678705-A

I: 7:20:0.07
V = 12 ℓ
P = 280 Torr
T = 300°K
v = 148 m/sec
τ = 15%
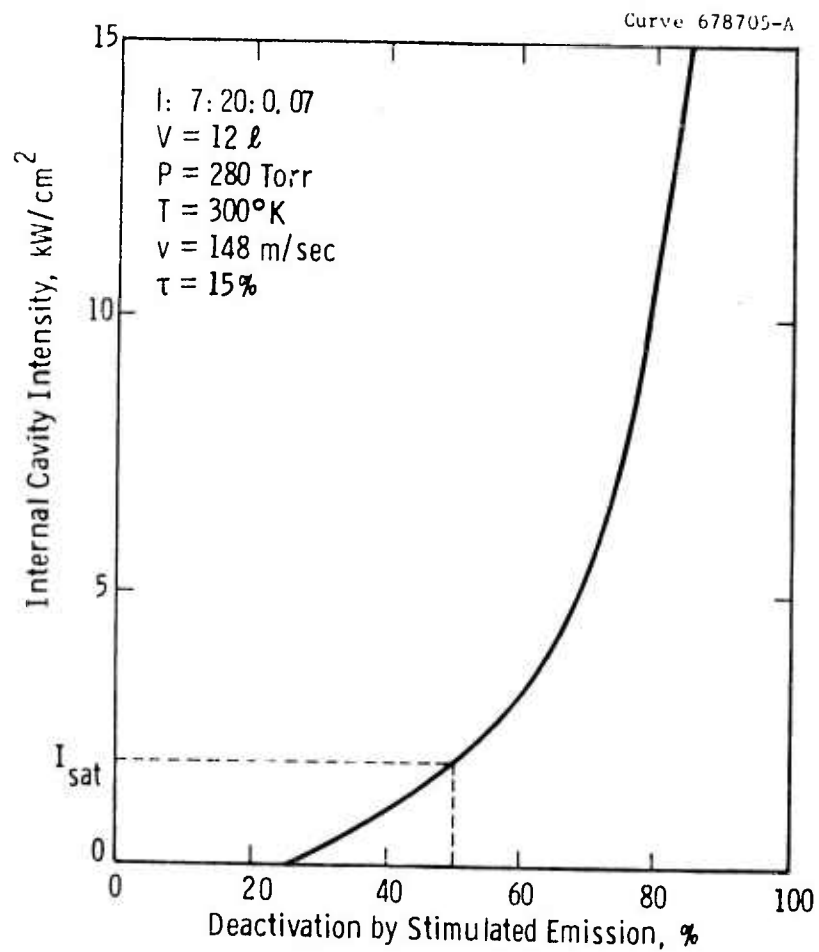
Fig. 3:21 The cavity flux dependence of the stimulated emission deactivation of the CO_2 asymmetric stretch mode for a current of 21 amp.

75

indeed operating within this region. Another check on this condition is to compare the intracavity radiation intensity with the saturation radiation intensity, l_{sat}. The latter intensity is that intensity which reduces the cavity gain to one-half of the small-signal gain. By assuming that the lower laser level depopulation is independent of the stimulated emission rate, l_{sat} is that intensity at which the deactivation rate of the upper laser level by stimulated emission is exactly equal to the deactivation rate by molecular collisions.[28] The stimulated emission deactivation rate relative to the collisional deactivation rate is given in Fig. 3:21 as a function of the intracavity intensity. This figure shows that for the given conditions the saturation intensity for the COFFEE laser is 1.75 kW/cm^2, which is indeed much smaller than the calculated operating intracavity intensity of 8.3 kW/cm^2 for the 21A case.

The examples in this section illustrate the utility of the CO_2 COFFEE laser kinetics computer code and demonstrate the excellent agreement of the theoretical small-signal gains with the experimental values. This code can be used either to explain experimental observations, or to develop and optimize a laser design which must meet specific application requirements.

3.1.5 Summary

A harmonic oscillator, six-temperature Boltzmann equilibrium model of the $CO_2:N_2:He:H_2O$ COFFEE laser system was developed and tested. The model includes the gas temperature dependence of the gas flow velocity, molecular densities (assuming constant pressure), and the VV and VT collisional relaxation rates. In addition, the E/N dependence of the electrical excitation rates was included as well as the effects of gas flow and external mirrors. All important sources of gas heating were incorporated, including direct gas discharge heating, VT relaxation, and intermode VV energy defect heating. The only experimental data needed by this model are the current density and electric field distribution in the downstream direction, the gas mixture, the flow velocity and gas temperature at the entrance of the laser cavity, and the geometrical design of the laser cavity.

The model is quite general and can be applied to most CO_2 gas
flowing laser systems of present interest. However, its use is restricted
to electrical excitation and stimulated emission rates slower than the
intramode relaxation times (∿50 nsec), to systems in which thermal
diffusion is unimportant, to pressures less than 100 atm, and to gas
temperature above freezing points (∿200°K) but below dissociation levels
(∿5000°K). Furthermore, the basic assumption of Boltzmann equilibrium
invalidates the model at high radiation intensities or very low CO_2
concentrations.[29]

Computer predictions were compared with measurements of the
P(22) small-signal gain in a 280 Torr, 1:7:20 flowing gas mixture with
2.0 Torr H_2 at total discharge currents of 1.0A and 1.5A. In addition,
these same conditions were modeled with external resonators included
and the optical cavity theoretically lengthened to 140 cm, although no
corresponding experimental energy extraction measurements were available
for comparison. The most important results obtained from these computer
calculations are:

1. The model gives accurate predictions. The six-temperature
model predicts values of the P(22) small-signal gain which agree very well
with the values measured over the entire cavity. The agreement is
particularly good near the peak gain where the experimental measurements
are the most accurate.

2. Chemical minority species are important. The good
agreement between theory and experiment was achieved by assuming that
the laser gas contained an initial background concentration of 0.15% H_2O
and that 14% of the H_2 was chemically converted to H_2O.

3. The gas is very efficiently pumped. The power deposition
into the gas was very uniform throughout the cavity, and the operating
value of E/N was always close to the optimum value for efficient pumping,
with 75 to 83% of the electrical power being deposited in the N_2
vibrational mode.

4. The upper laser level is efficiently depopulated. The
intracavity radiation intensity was about five times larger than the

saturation intensity of 1.8 kW/cm^2. This assures that the depopulation of the upper laser level is primarily by stimulated emission rather than by collisional relaxation.

5. The COFFEE laser is efficient and powerful. At a pressure of 280 Torr in a 8 x 11 x 140 cm cavity an output power of 45 kW is predicted with an efficiency of 15%. Furthermore, the output efficiency peaks at a pressure of 90 Torr, whereas as the output power peaks at a pressure above 300 Torr.

6. The COFFEE laser can be easily scaled. The predicted exit temperature for the 8 x 11 x 140 cm cavity is only 336°K which indicates that the laser cavity can be appreciably extended in the downstream direction before the laser performance would degrade significantly by collisional deactivations increased by temperatures above 450°K.

These results form a firm foundation for future work. The tests of the computer program and six-temperature model verify their applicability for CO_2 COFFEE laser kinetic simulations and recommend their use for system modeling and prediction. However, detailed comparisons with experiments under lasing conditions are required for further verification, and a better understanding of the hydrogen to water conversion is desirable. With these reservations the CO_2 COFFEE laser kinetics program can be employed for systematic variations of parameters to establish optimum operating conditions, to explain experimental observations, or to design the next generation COFFEE laser,

3.1.6 Conclusions

Three general conclusions can be drawn from the laser kinetics model calculations:

1. The six-temperature model can accurately predict and explain the performance of CO_2 COFFEE lasers.

2. Efficient (15%), high-power (45 kW) COFFEE lasers can be built by simply increasing the present optical cavity length to 140 cm.

3. Appreciably more efficient and powerful COFFEE lasers can be built by extending the excitation region in the downstream direction.

3.2 V-I CHARACTERISTICS

The COFFEE laser excitation scheme uses a continuous self-sustained glow discharge in high-pressure CO_2 laser gas mixtures. The voltage-current characteristics of the glow govern the power into the discharge while the operating E/N controls the laser excitation efficiency as described in Section 3.1. It is important, therefore, to determine what factors govern these parameters.

The operating E/N of a glow discharge is that value which leads to a steady state balance between the rates of all the electron generation and loss mechanisms. The analysis of Lowke, Phelps, and Irwin[16] shows that for a volume controlled discharge

$$j/N = (eW^2/\gamma)(\alpha-a)/N \qquad (3:9)$$

where j is the current density, N is the neutral gas density, e is the electron charge, W is the electron drift velocity, γ is the recombination loss rate, α is the ionization coefficient, and a is the attachment coefficient. Equation (3:9) expresses j/N as a function of E/N through the dependencies calculated by Lowke et al. of W, α/N, and a/N on E/N. The curves in Fig. 3:22 were drawn for Eq. (3:9) using three representative gas mixtures. For low values of j/N two limits are shown. The broken curves correspond to the case of an attachment dominated glow while the solid curves correspond to a recombination controlled glow. Gases such as CO_2, H_2O and O_2 are known to produce electron loss by attachment.[6] For example, dissociative attachment by CO_2 to form CO and O^- leads to electron loss. Certain gas additives[57-59] may act to suppress attachment and lower the operating E/N at a given j/N. This can result in higher laser excitation efficiencies. The operating E/N will become recombination-controlled at high current densities since recombination losses increase as the square of the current.
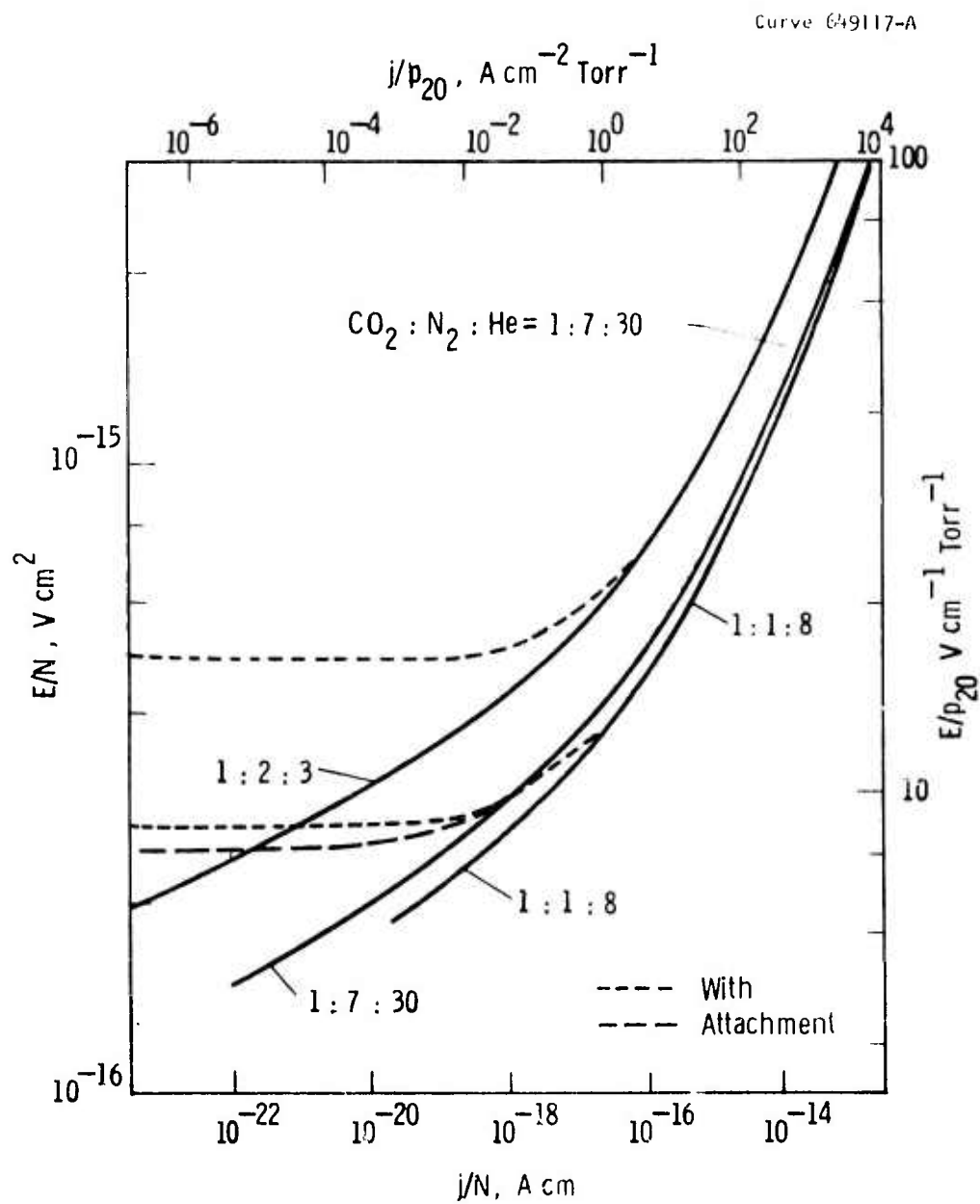
Fig. 3:22 Predicted E/N-j/N characteristics assuming there is a volume controlled glow with $\gamma = 10^{-7}$ cm^3 sec^{-1}.

The effect of varying the helium content in the laser mixture is shown in Fig. 3:23. If the proportion of helium is increased for a given E/N, the average electron energy is also increased because helium has none of the inelastic vibrational losses that are present in nitrogen and carbon dioxide. Thus, electron energies sufficient to excite the upper laser level occur at lower E/N for the 1:7:30 mixture than for the 1:7:0 mixture where helium is absent. At first glance one might try to optimize the mixture for maximum efficiency by varying the helium content. However, it is seen from Fig. 3:23 that the change in E/N for maximum efficiency and the change in operating E/N are approximately the same. It appears, therefore, that the addition of helium has no significant influence on the effective laser excitation efficiency for a self-sustained glow discharge of interest.

The COFFEE laser operates in the current regime ($j/N < 10^{-19}$ A-cm) where attachment appears to dominate the discharge. Figure 3:24 shows calculated values of α/N and a/N as a function of E/N for three gas mixtures.[57] An attachment dominated self-sustained discharge will operate at the E/N value where $\alpha = a$. Similar calculations for a 1:7:20 mixture of CO_2:N_2:He predict an operating E/N of 3.0×10^{-16} V-cm^2, which is independent of achievable operating current densities. This agrees to first order with the experimental results obtained.

There are, however, a number of discrepancies which this simple model does not explain. Figure 3:25 shows the predicted and derived E/N distributions as a function of downstream distance in the discharge for a typical set of operating conditions. For an attachment dominated discharge in a given gas composition one would expect the operating E/N to be a constant independent of downstream distance. The derived E/N values were calculated from the measured E values using the laser kinetics code to determine the N distribution as described in Section 3.1. Near the upstream portion of the discharge the agreement was within 10%. However, the operating E/N dropped almost 40% as the laser gas flowed downstream through the discharge, which is presently unexplained by the model. If the discharge were recombination controlled,
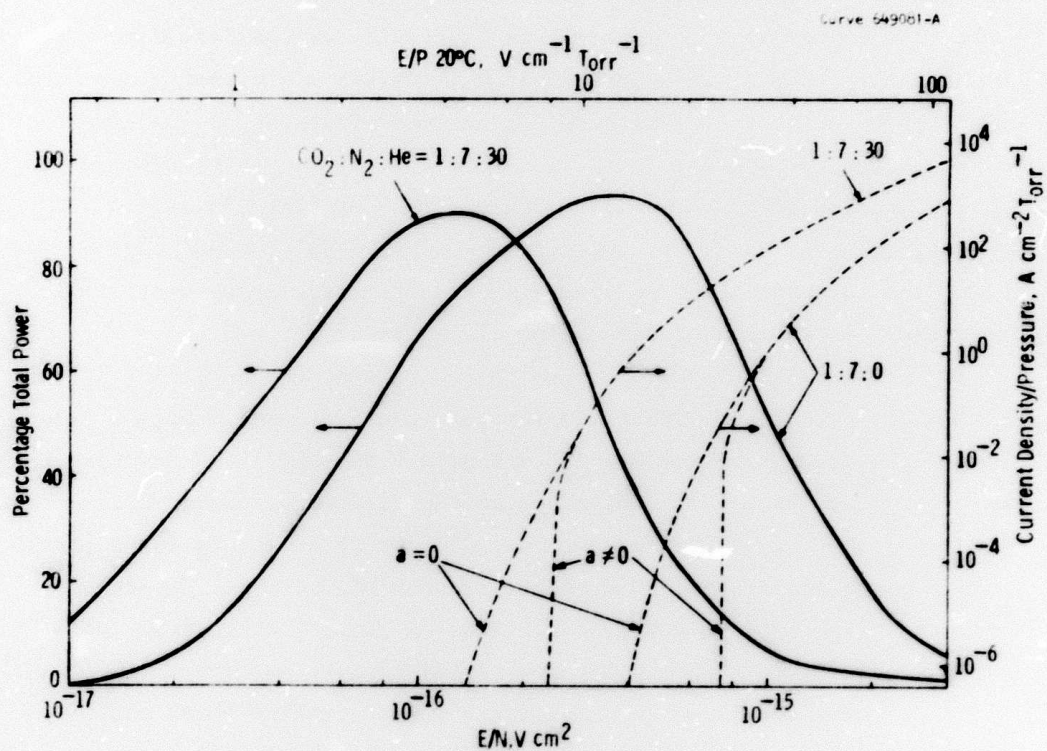
Fig. 3:23 Solid curves show calculated excitation efficiency based on excitation levels coupled to the upper laser level. Broken curves show calculated V-I characteristics for two laser mixtures.
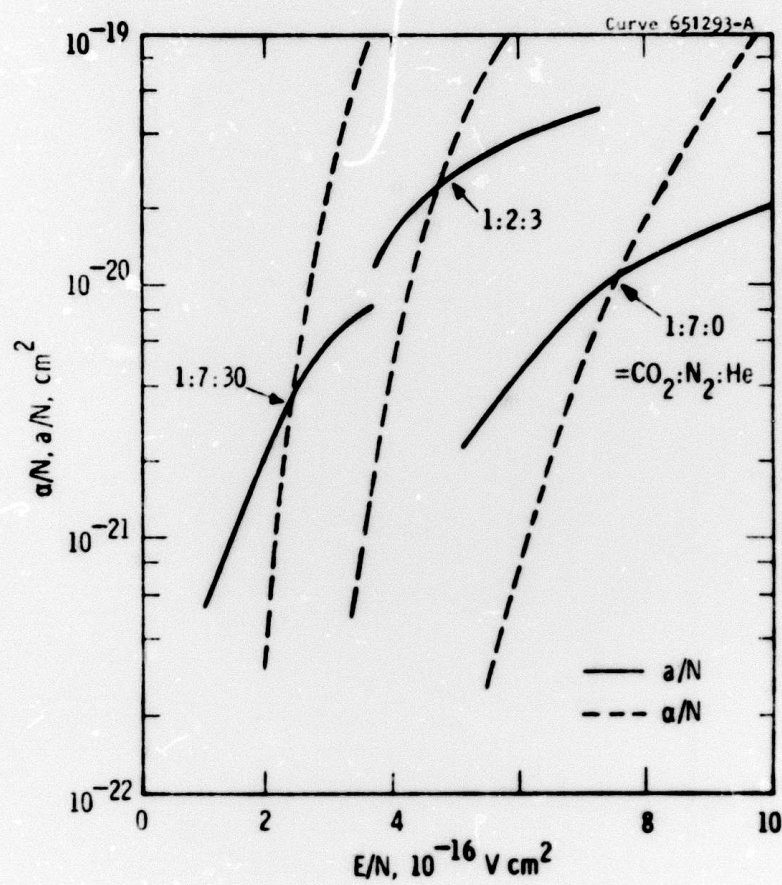
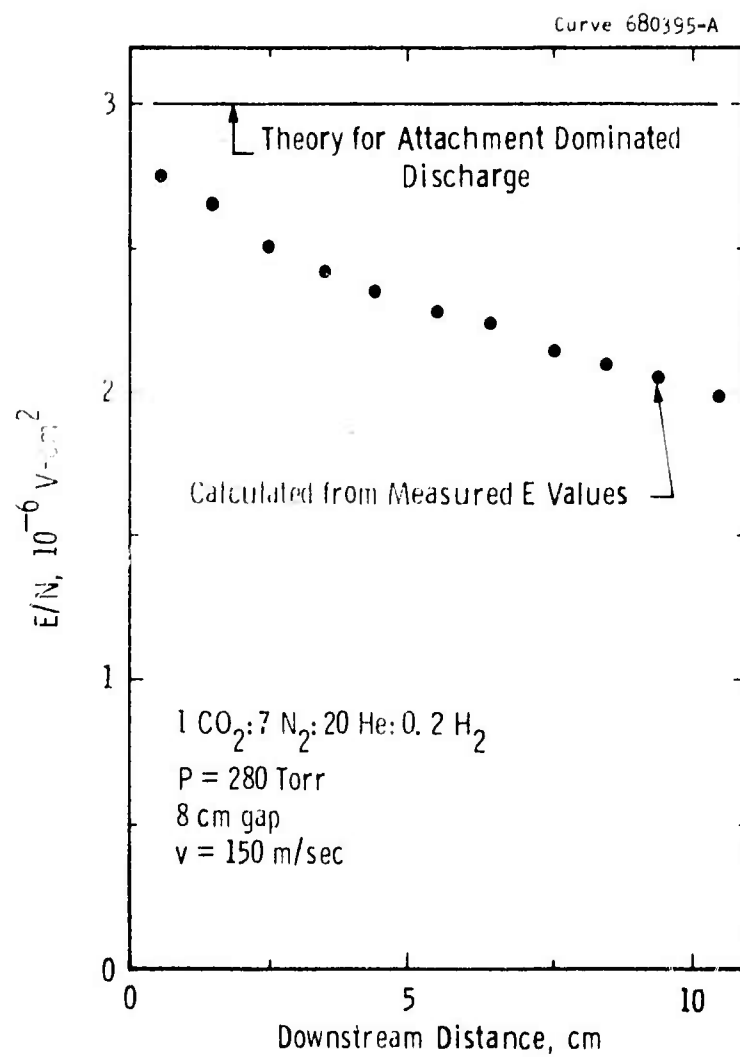Fig. 3:24 Calculated values of α/N and a/N as a function of E/N for the mixtures indicated.

Fig. 3:25 E/N distribution for 1.5 A in 8 x 11 x 10 cm discharge.

84

E/N would be expected to increase in the downstream direction because the current density rose (see Fig. 3:3). It is not possible to explain a variation of this magnitude on the basis that the discharge may be bending more at an upstream location than at a downstream location. It appears that something is created in the upstream portion of the discharge which is carried downstream by the flow and effectively lowers the operating E/N. For example, various transient minor molecular species may be created by the upstream portion of the discharge which subsequently alter the attachment-detachment rates downstream.[60] Such processes have not been modeled yet.

Two other parametric dependencies have been observed for E/N, as shown in Figs. 3:26 and 3:27, which are not fully explained at present. The data in these two figures are typical of results obtained under many operating conditions with two different experimental devices.[60] The E/N values are from the upstream portion of the discharge where gas heating corrections to N did not have to be taken into account. Figure 3:26 shows that E/N has a slight discharge current dependence. However, the E/N dependence on gas flow velocity shown in the two figures is surprisingly large. For example, doubling the gas velocity increased E/N by ∿50%. Again, this cannot be explained quantitatively by discharge deflection models. Obviously more work is needed in this area.

In summary, it should be noted that the relatively simple glow discharge model does give a good first order prediction of the operating E/N. In addition, the operating range of E/N (Fig. 3:25) coincides with the optimum values required for efficient laser excitation (Fig. 3:3).
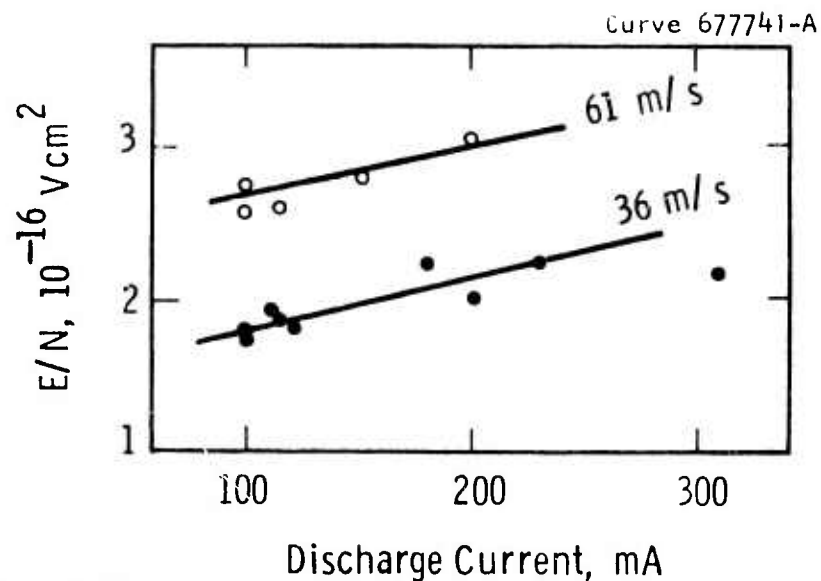
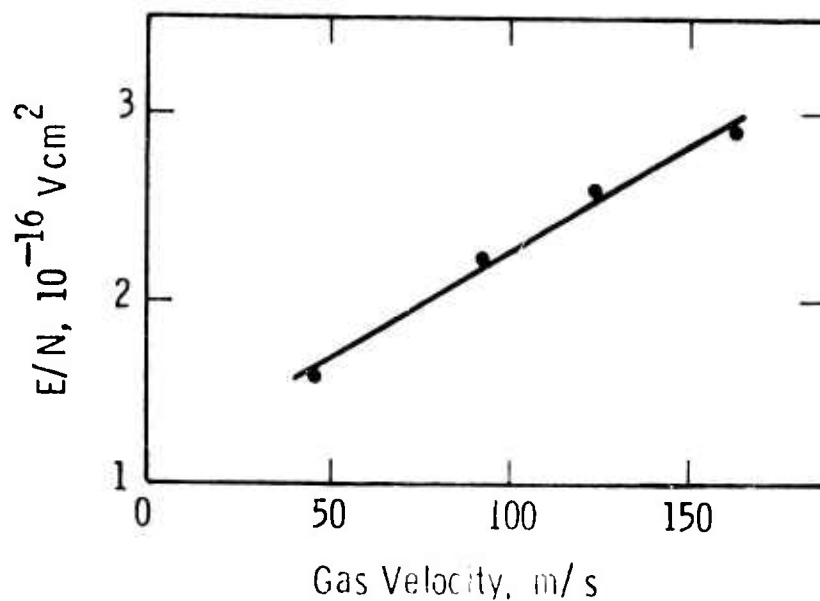Fig. 3:26 Variation of E/N with transverse gas velocity
and discharge current, for $1CO_2:7N_2:20He:1H_2$.

Fig. 3:27 Variation of E/N with transverse gas velocity,
for $1CO_2:7N_2:30He$.

4. HIGH POWER LASER DEVELOPMENT

One of the main objectives of this study was to demonstrate the feasibility of developing multi-kilowatt devices using the COFFEE laser excitation technique. The discharge scaling experiments described in Section 2 and the modeling studies described in Section 3 clearly demonstrate that it is feasible to build high-power COFFEE lasers. In anticipation of this result, a parallel effort to construct a 25 kW proof of scalability test laser was started. During this reporting period a new compact closed-cycle flow facility was built as shown in Fig. 4:1. The tank is 6 feet in diameter and approximately 8 feet long. Flow rates up to 7000 ℓ/sec are attainable with operating pressures from 50 to 760 Torr. Heat exchangers and an external DC power supply (in back room of Fig. 4:1) are also available along with the control console shown.

Preliminary tests using an existing electrode assembly were performed. The maximum usable aperture for this assembly was 2 x 5 cm with a 140 cm active path length along the optical axis. Up to 6 kW of output power was obtained from this discharge volume using hole-coupled optics. The conversion efficiency was $\sim$10% with $\sim$4 W/cm^3 being extracted from the discharge volume. Calculations using the kinetics code described in Section 3 indicate that the extraction efficiency of the simple optical cavity was only 70%.

Future plans include the installation of a new electrode assembly with a 10 x 10 cm aperture in the flow system. An unstable resonator optical cavity will also be installed. Originally this work was to be performed as a Phase III continuation of Phase II work described in this report. However, the lack of funding has for the time being, delayed this continuation.
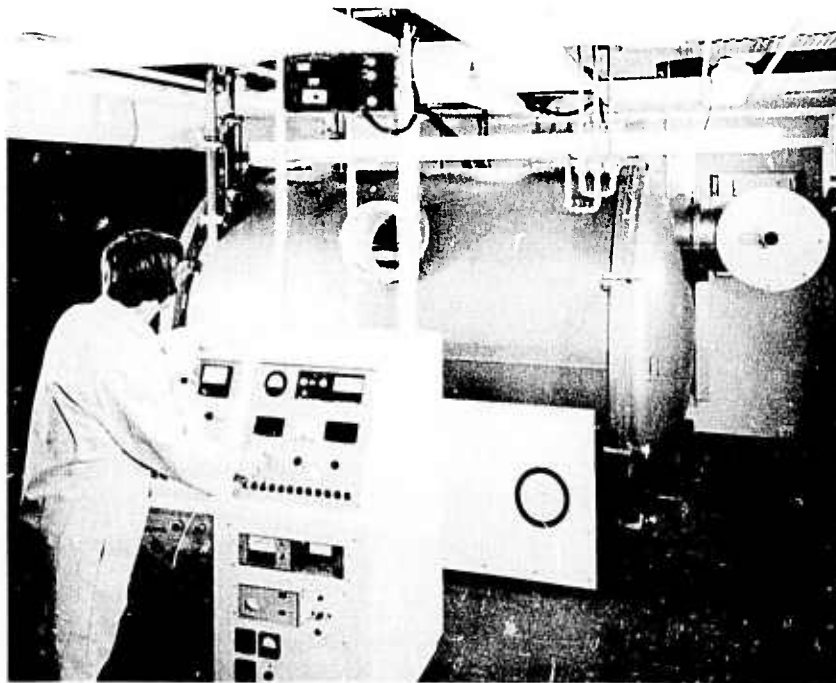
Fig. 4:1 Compact COFFEE laser facility for 25 kW scaling tests.

5. SUGGESTED FUTURE WORK

The scaling criteria for the COFFEE laser excitation scheme are developed to the point that simple, rugged, and compact high-power laser systems can easily be designed. There are a few areas, however, where additional information would be most useful. First, certain portions of the discharge physics need to be developed more fully. For example, the effects of transient minor molecular species and gas flow, as discussed in Section 3.2, on the operating E/N are poorly understood. Additional knowledge in this area would better insure controlled operation at the optimum E/N for efficient excitation. Furthermore, the glow-to-arc transition problems appear to be affected by the same processes. Any information which helps raise the arcing limit will result in increased specific input energy, input power density, efficiency, and power output.

Second, a large scale device should be built and tested, not only to assess the reliability of the scaling criteria, but also to determine if there are any major engineering problems which have to be overcome. Although no significant problems are anticipated, proof of scalability should be demonstrated.

Finally, the cavity extraction and beam quality problems, which tend to be inherent in all high-power cw devices, should be addressed more fully. The COFFEE laser has the unique feature that the input power is easily tailored in the transverse direction in order to match certain cavity extraction criteria. All this additional information will provide a better technology base for designing the next generation devices.

89

6. REFERENCES

1. S. A. Wutzke, J. L. Pack, G. L. Rogoff and J. J. Lowke, "CW Pin Discharge Laser," Phase I Final Technical Report under contract N00014-73-C-0318 (November 1973).

2. G. L. Rogoff, "Gas Heating Effects in the Constriction of a High-Pressure Glow Discharge Column," Phys. Fluids 15, 1931-1940 (1972).

3. G. L. Rogoff, "Initial Development of Glow-to-Arc Transition due to Electric Field Distortion," Bull. Am. Phys. Soc. 20, 234 (1975).

4. W. L. Nighan and W. J. Wiegand, "Causes of Arcing in CW CO_2 Convection Laser Discharges," (to be published in Appl. Phys. Lett. 25, 633 (1974)).

5. P. V. Avizonis, D. R Dean, and R. Grotbeck, Appl. Phys. Lett. 23, 375 (1973).

6. L. J. Denes, L. H. Taylor and R. W. Liebermann, "UV Initiated CO_2 Laser Research," Phase I Technical Report (Interim), AFWL Contract No. F29601-73-C-0121 (September 1974).

7. L. J. Denes and L. A. Weaver, Appl. Phys. Lett. 44, 4125 (1974).

8. E. F. Barker and A. Adel, Phys. Rev. 44, 185 (1933).

9. E. Arie, N. Lacome and C. Rossetti, Can. J. Phys. 50, 1800 (1972).

10. G. Herzberg, Molecular Spectra and Molecular Structure, Vol. II, Infrared and Raman Spectra of Polyatomic Molecules, (Van Nostrand, Princeton, N.J., 1964), p. 395.

11. G. Herzberg, ibid, p. 508-9.

12. E. R. Murray, C. Kruger and M. Mitchner, Appl. Phys. Lett. 24, 180 (1974).

13. R. L. Leonard, Appl. Optics 13, 1920 (1974).

14. S. Singer, IEEE J. Quant. Electr. QE-10, 829 (1974).

15. L. J. Denes, L. H. Taylor, L. A. Weaver and R. W. Lieberman, ibid.

16. J. J. Lowke, A. V. Phelps and B. W. Irwin, "Predicted Electron Transport Coefficients and Operating Characteristics of CO_2-N_2-He Laser Mixtures," J. Appl. Phys. _44_, 4664 (1973).

17. N. G. Basov, A. N. Oraevskii and V. A. Schcheglov, "Production of a Population Inversion in Molecules of a Working Gas Mixed with a Thermally Excited Auxiliary Gas," Sov. Phys.--Technical Phys. _15_, 126 (1970).

18. A. Messiah, _Quantum Mechanics 1_, North Holland Publishing Co., Amsterdam (1961).

19. L. Landau and E. Teller, "Zero Theorie die Schalldispersion," Phys. Z. Sowjetunion _10_, 34 (1936).

20. R. N. Schwartz, Z. I. Slawsky and K. F. Herzfeld, "Calculation of Vibrational Relaxation Times in Gases," J. Chem. Phys. _20_, 1591 (1952).

21. D. L. Lyon, "Comparison of Theory and Experiment for a Transversely Excited High-Pressure CO_2 Laser," IEEE J. Quantum Electron. _QE-9_, 139 (1973).

22. D. L. Lyon, "Collisional Relaxation Mechanisms Governing Operation of High-Pressure CO_2 Lasers," Ph.D. Thesis, Dept. of E.E., MIT (1972).

23. H. Granek, "Study of Long Pulse High Energy Amplification at 10.6 μm," Project Report LTP-21, MIT Lincoln Laboratory (1973).

24. R. J. Harrach and T. H. Einwohner, "Four-Temperature Kinetic Model for a CO_2 Laser Amplifier," Report No. UCRL-51399, Lawrence Radiation Laboratory (1973).

25. R. L. Taylor and S. Bitterman, "Survey of Vibrational Relaxation Data for Processes Important in the CO_2-N_2 Laser System," Rev. Mod. Phys. _41_, 26 (1969).

26. D. H. Douglas-Hamilton, "AERL Kinetics Handbook," Air Force Weapons Laboratory (1974).

27. P. Henrici, _Elements of Numerical Analysis_, John Wiley and Sons, New York (1964).

28. W. W. Rigrod, "Saturation Effects in High-Gain Lasers," JAP _36_, 2487 (1965).

29. A. L. Hoffman and G. C. Vlases, "A Simplified Model for Predicting Gain, Saturation, and Pulse Length for Gas Dynamic Lasers," IEEE J. Quantum Electron. $\underline{QE-8}$, 46 (1972).

30. K. A. Herzfeld and T. A. Litovitz, Absorption and Dispersion of Ultrasonic Waves, Academic Press, New York (1959).

31. E. E. Nikitin, "On the Calculation of the Probability for Vibrational Excitation of Molecules During Collisions," Optics and Spectr. $\underline{6}$, 93 (1959).

32. Y. V. Stupochenko, S. A. Losev, and A. I. Osipov, Relaxation in Shock Waves, Springer-Verlag, New York (1967).

33. J. R. MacDonald, "Rate Coefficients for Vibrational Energy Transfer in Rapid Expansions of Carbon Dioxide-Nitrogen Mixtures," SU-IPR Report No. 394 (1970).

34. K. Bulthuis and G. J. Ponsen, "On the Relaxation of the Lower Laser Level of CO_2," Chem. Phys. Letters $\underline{14}$, 613 (1972).

35. R. D. Sharma, "Kinetics of Equilibration of 1388 cm^{-1} Vibrational Level of CO_2," J. Chem. Phys. $\underline{49}$, 5195 (1968).

36. C. K. Rhodes, M. J. Kelly and A. Javan, "Collisional Relaxation of the $10°0$ State in Pure CO_2," J. Chem. Phys. $\underline{48}$, 5730 (1968).

37. E. E. Stark, "Measurement of the $10°0-02°0$ Relaxation Rate in CO_2," Appl. Phys. Lett. $\underline{23}$, 335 (1973).

38. K. Bulthuis, "Laser Power and Vibrational Energy Transfer in CO_2 Lasers," J. Chem. Phys. $\underline{58}$, 5786 (1973).

39. W. A. Rosser, E. Hoag and E. T. Gerry, "Relaxation of Excess Populations in the Lower Laser Level CO_2 $(100)^*$," J. Chem. Phys. $\underline{57}$, 4153 (1972).

40. L. B. Evans, "Vibrational Relaxation in Moist Nitrogen," J. Acoust. Soc. Am. $\underline{51}$, 409 (1972).

41. L. J. Denes and J. J. Lowke, "V-I Characteristics of Pulsed CO_2 Laser Discharges," Appl. Phys. Lett. $\underline{23}$, 130 (1973).

42. B. F. Gordietz, N. N. Sobolev, V. V. Sokovikov and L. A. Shelepin, "Population Inversion of the Vibrational Levels in CO_2 Lasers," IEEE J. Quantum Electron. $\underline{QE-4}$, 796 (1968).

43. F. Daniels and R. A. Alberty, _Physical Chemistry_, John Wiley and Sons, New York (1955).

44. D. R. Stull and H. Prophet, _JANAF Thermochemical Tables_, 2nd Ed., U. S. Department of Commerce, NSRDS-NBS37 (1971).

45. E. H. Kennard, _Kinetic Theory of Gases_, McGraw-Hill Book Co., New York (1938).

46. G. L. Rogoff, ibid

47. J. J. Lowke, A. V. Phelps and B. W. Irwin, ibid.

48. W. Band, _An Introduction to Quantum Statistics_, D. Van Nostrand Co., New York (1955).

49. G. Herzberg, ibid.

50. L. H. Taylor, L. A. Weaver and L. D. Pleasance, "Four Gas Lasers Dynamic Models," Westinghouse Research Report 73-1C8-SHOWA-R1 (1973).

51. E. T. Gerry and D. A. Leonard, "Measurement of 10.6 μ CO_2 Laser Transition Probability and Optical Broadening Cross Sections," Appl. Phys. Letters $\underline{8}$, 227 (1966).

52. E. R. Murray, C. Kruger and M. Mitchner, ibid.

53. T. W. Meyer and C. K. Rhodes, 1973 IEEE/OSA Conference on Laser Engineering and Applications, Washington, D. C. (unpublished).

54. J. C. Slater, _Quantum Theory of Atomic Structure I_, McGraw-Hill Book Co., New York (1960).

55. B. diBartolo, _Optical Interactions in Solids_, John Wiley and Sons, New York (1968).

56. W. V. Smith and P. P. Sorokin, _The Laser_, McGraw-Hill Book Co., New York (1966).

57. L. J. Denes and J. J. Lowke, Appl. Phys. Lett. $\underline{23}$, 130 (1973).

58. F. C. Fehsenfeld, E. E. Ferguson, and A. L. Schmeltckopf, J. Chem. Phys. $\underline{45}$, 1844 (1966).

59. J. L. Moruzzi and A. V. Phelps, J. Chem. Phys. $\underline{45}$, 4617 (1966).

60. R. V. Babcock, Westinghouse Research Memo 74-1C2-LASER-M1 (1974).

7. APPENDICES

APPENDIX A

NOMENCLATURE FOR SECTION 3.1

Boltzmann Factors

T = gas kinetic temperature

T_α = vibrational temperature of α vibrational mode

$a = e^{-\theta_a/T_a}$

$b = e^{-\theta_b/T_b}$

$n = e^{-\theta_n/T_n}$

$s = e^{-\theta_s/T_s}$

$w = e^{-\theta_w/T_w}$

$\bar{b} = e^{-\theta_b/T}$

$\bar{n} = e^{-\theta_n/T}$

$\bar{w} = e^{-\theta_w/T}$

Characteristic Temperatures

θ_α = characteristic temperature of α vibrational mode

$\theta_a = 3380°K$

$\theta_n = 3354°$

$\theta_w = 2295°$

$\theta_s = 1997°$

$\theta_b = 960°$

$\theta_{wb} = \theta_w - \theta_b = 1335°$

$\theta_{aw} = \theta_a - \theta_w = 1085°$

$\theta_{nw} = \theta_n - \theta_w = 1059°$

$\theta_{ab} = \theta_a - 3\theta_b = 599°$

$\theta_{sb} = \theta_s - 2\theta_b = 147°$

$\theta_{an} = \theta_a - \theta_n = 26°$

θ_r = characteristic temperature of rotational mode = $0.556°K$.

94

Energy Defect Factors

$$A = e^{-\theta_{an}/T}$$
$$B = e^{-\theta_{sb}/T}$$
$$C = e^{-\theta_{ab}/T}$$
$$D = e^{-\theta_{nw}/T}$$
$$F = e^{-\theta_{aw}/T}$$
$$G = e^{-\theta_{wb}/T}$$

Gas Heating Factors

C_β = specific heat at constant pressure in joule $\deg^{-1}$ mole^{-1}.

$C_h = 20.79$

$C_n = 29.11$

$C_c = 29.11$

$C_w = 33.26$

E_α = characteristic energy density in joule cm^{-3}.

F_e = fraction of the electrical energy which is not lost by photon emission from electronically excited levels.

f_α = molar density in no. moles cm^{-3} of α species.

ζ = electronic heating factor--the fraction of the electronic excitation energy which heats the gas.

Radiation Intensities

$a_{i\gamma J}$ = loss per bounce at the ith mirror (including transmissivities).

$b_{\gamma J}$ = scattering loss per cm inside the gas.

$I_{\gamma J}$ = total light intensity in watts/cm^2.

$I'_{\gamma J}$ = collimated light intensity.

$I^u_{\gamma J}$ = uncollimated light intensity.

I_o = incident light intensity to be amplified by laser.

I_{out} = total light intensity out of the laser.

$K = V_u/A_u$ = uncollimated light conversion factor from power density to light intensity in cm.

$K'' = A_o/V_c$ = input light conversion factor from light intensity to power density in cm^{-1}.

95

$P_{\gamma J}$ = spontaneous emission power density in watts/cm^3.

$\alpha_{\gamma J}$ = total gain of gas medium in cm^{-1}.

$\beta_{\gamma J}$ = average cavity loss per cm (also called the cavity gain or threshold gain).

$\Delta n_{\gamma J}$ = population inversion density in cm^{-3}.

$\varepsilon_{\gamma J}$ = probability that a spontaneously generated photon is fed into the lasing mode.

$\tau_{i\gamma J}$ = transmissivity of the ith mirror.

Subscripts

a = asymmetric stretch mode (ASM) of CO_2.

b = bending mode (BM) of CO_2.

c = CO_2.

h = He.

n = N_2.

o = denotes value for the gas flowing into the discharge volume before that value is modified by the discharge or lasing action, i.e., the value at $x = 0$.

s = symmetric stretch mode (SSM) of CO_2.

w = H_2O.

Transition Rates

Collisional

A', B', C' = parameterization constants for reaction rate constants.

$D' = \theta_{\alpha\beta}/2$ = constant used in reaction rate constant.

$k_{\alpha\beta}$ = reaction rate constant in cm^3 per β particle per second.

N_α = no. of α particles cm^{-3} (Note that $N_a = N_b = N_s = N_c$).

N = total number of density of gas in particles cm^{-3}.

R_α = VT transition rate in no. of transitions per second.

$R_{\alpha\beta}$ = VV transition rate due to collisions between α and β particles.

Electrical

E = electric field in V/cm.

I = discharge current in A.

j = discharge current density in A cm^{-2}.

U_α = electrical pumping term in sec^{-1}.

V = voltage drop across the discharge in volts.

W_α = power density entering the α mode in W cm^{-3}.

γ_α = fraction of electrical power density which excites the α vibrational mode, electronic levels (α=e), or ionizes the gas (α=i).

Stimulated Emission

A_{21} = spontaneous transition probability rate between upper and lower laser levels in sec^{-1}.

B_G = Gaussian bandwidth in cm^{-1} (full linewidth at half maximum).

$B_{\gamma J}$ = Lorentzian bandwidth in cm^{-1} (full linewidth at half maximum).

$f_{\gamma J}$ = photon flux in photons sec^{-1} cm^{-2}.

J' = rotational quantum number of upper laser level (must be odd).

J = rotational quantum number of lower laser level (must be even).

M = CO_2 mass in amu.

$n_{\gamma J'}$ = population density of upper laser level in particles cm^{-3}.

$n_{\gamma J}$ = population density of lower laser level in particles cm^{-3}.

P = denotes P branch transition (J_{upper} = J-1).

$Q_{\gamma J}$ = common rotational factor of the stimulated emission factor.

R = denotes R branch transition (J_{upper} = J+1).

$S_{21}^{\gamma J}$ = stimulated transition probability rate in sec^{-1}.

β_J = fraction of molecules in the Jth rotational level.

γ = P or R = specifies branch for rotational transition.

Γ = stimulated emission term in sec^{-1}.

$\Gamma_{\gamma J}$ = stimulated emission factor.

μ_{ci} = reduced mass of species CO_2 and i in amu.

97

$\bar{\nu}_o$ = laser radiation wave number in cm^{-1}.

$\phi_{\gamma J}(0)$ = value of line shape factor at line center in cm.

$\sigma_{\gamma J}$ = stimulated emission cross-section in cm^2.

$\sigma_{c\alpha}$ = optical broadening cross-section.

$$\sigma_{cn} = 91 \ \overset{\circ}{A}{}^2$$
$$\sigma_{ch} = 25 \ \overset{\circ}{A}{}^2$$
$$\sigma_{cc} = 130 \ \overset{\circ}{A}{}^2$$
$$\sigma_{cw} = 73 \ \overset{\circ}{A}{}^2$$

$\tau_{\gamma J}$ = Lorentzian lifetime in seconds.

Laser Cavity

The following relations (in cgs units) pertain to the geometrical design of the laser cavity and are easily derivable. A plane-parallel laser cavity with a rectangular discharge is assumed. The mirrors are assumed to be rectangular and plane-parallel.

x = downstream distance from the entrance to the laser cavity.

v = gas flow velocity in cm sec^{-1}.

L = distance between the mirrors.

V_{dis} = $WH\ell$ = volume of the gas discharge.

ℓ = length of discharge along a line joining the mirror centers.

W = length of discharge perpendicular to the line joining the mirror centers and along the direction of the gas flow.

H = length of discharge between the electrodes, and the height of the mirrors.

A_o = cross-sectional area of input radiation intensity.

V_u = V_{dis} = total volume from which the uncollimated radiation originates.

A_u = $2\ell(W+H)$ = enclosing area of discharge volume through which the uncollimated radiation escapes.

V_c = V_{dis} = total volume of gas which contains all the lasing radiation.

98

Constants

$$k = 1.38054 \times 10^{-16} \text{ erg deg}^{-1}$$
$$k' = 1.38054 \times 10^{-23} \text{ joule deg}^{-1}$$
$$h' = 6.6256 \times 10^{-34} \text{ joule sec}$$
$$c = 2.997925 \times 10^{10} \text{ cm sec}^{-1}$$
$$e = 1.60210 \times 10^{-19} \text{ coulombs}$$
$$\pi = 3.141593$$
$$N_o = 6.02252 \times 10^{23} \text{ particles mole}^{-1}$$
$$W = 1.65979 \times 10^{-24} \text{ gm amu}^{-1}$$

APPENDIX B

COLLISIONAL RELAXATION

The collisional exchange of energy between molecules in different vibrational states has been treated by the SSH theory,[20] which employs the Landau-Teller selection rules[19] for quantum transitions of simple harmonic oscillators. The dominant collisional interactions are depicted in Fig. 3:2. The A, B, C, D, F and G factors in the VV relaxation terms of Eqs. (3:1-6) account for the energy defects involved in the collisional interactions.

The double degeneracy of the CO_2 bending mode gives rise to the first and last two factors of 2 in Eq. (3:3). In keeping with the SSH theory approximations, only those collisional transitions are assumed to occur which involve one of the bending modes, independent of the other bending mode. The factor of 3 arises from the exchange of one ASM quantum for three BM quanta, while the second factor of 2 arises from the exchange of one SSM quantum for two BM quanta. All other VV energy exchanges involve one quantum in each mode.

The total VT transition rates (second^{-1}) are given by

$$R_b = \sum_\beta k_b^{(\beta)} N_\beta \qquad \beta = c,h,n,w$$

$$R_n = \sum_\beta k_n^{(\beta)} N_\beta \qquad\qquad\qquad (B:9)$$

$$R_w = \sum_\beta k_w^{(\beta)} N_\beta$$

where $k_\alpha^{(\beta)}$ is the reaction rate constant in cm^3 per particle β per second, and N_β is the number density of the particles. The sum is over all the gas components $\beta(c=CO_2, h=He, n=N_2, w=H_2O)$. The VV transition rates for intramolecular energy exchanges through collisions with other molecules are given by

100

$$R_{ab} = \sum_{\beta} k_{ab}^{(\beta)} N$$

$$R_{sb} = \sum_{\beta} k_{sb}^{(\beta)} N$$

<div align="right">(B:10)</div>

whereas the intermolecular VV transition rates are given by

$$R_{an} = k_{an} N_n \qquad\qquad R_{na} = k_{na} N_a$$

$$R_{aw} = k_{aw} N_w \qquad\qquad R_{wa} = k_{wa} N_a$$

$$R_{bw} = k_{bw} N_w \qquad\qquad R_{wb} = k_{wb} N_b$$

$$R_{nw} = k_{nw} N_w \qquad\qquad R_{wn} = k_{wn} N_n$$

<div align="right">(B:11)</div>

In these expressions

$$k_{\alpha\beta} = k_{\beta\alpha}$$

<div align="right">(B:12)</div>

and the a, b, and s subscripts denote the ASM, BM, and SSM of the CO_2 molecule. The particle densities are specified by the laser operating conditions, and the reaction rate constants are derived from experimental measurements or estimated.

Qualitatively, collisional relaxation rate constants are fairly well understood both theoretically and experimentally. However, quantitatively the theory is inadequate and the experiments are frequently very difficult to perform. Nonetheless, many relevant rate constants have been measured. For these reasons the theory is used to give a parameterized equation for the temperature dependence which is then fitted to available measurements.

Collisional theory[30-32] states that the parameterized temperature behavior of VV and VT collisional rate constants is given by

$$k = \frac{A'x^2}{1 + F'x^3} e^{-B'x + C'x^2 + D'x^3}$$

<div align="right">(B:13)</div>

101

where

$$x = T^{-1/3}$$

and the A', B', C', D', and F' are parameterization constants. Actually, D' is fairly well determined to be

$$D' = \frac{1}{2} \theta \qquad (B:14)$$

where θ is the energy defect of the exothermic collisional transition. Since the temperature dependence of Eq. (B:13) is dominated by the terms in x in the exponent, a reasonable simplification is to take

$$F' = 0 \qquad (B:15)$$

Equation (B:13) was fitted to experimentally measured values at three different temperatures by using Eqs. (B:14) and (B:15). This fit then determined the values of A', B' and C' and the collisional rate constants used in the laser kinetics code.

This fitting procedure can be used in two different ways. If B' and C' are positive and have reasonable values, then the theory upon which Eq. (B:13) is based is probably valid. In this case

$$A' \propto \mu^{7/6} \qquad (B:16)$$

$$B' \propto \mu^{1/3} \qquad (B:17)$$

$$C' \propto \epsilon^{1/2} \mu^{1/6} \qquad (B:18)$$

where μ is the reduced mass of the colliding particles and ϵ is the Lennard-Jones intermolecular potential energy parameter.[32] These equations can then be used to scale known rate constants for an estimate of unknown rate constants. On the other hand, if B' or C' is negative or unreasonably valued, Eq. (B:13) can be used simply as a mathematical fitting expression, and scaling is invalid.

102

A critical evaluation of available rate constants shows that Taylor and Bitterman[25] have assembled the most reliable set of experimental measurements. All relevant VT rate constant parameters can be derived from this reference and are given in Table B:1.

The VT rate constants for the relaxation of the BM are shown in Fig. B:22. Water clearly exhibits anomalous behavior in that its rate constant for emptying the lower laser level (since the BM and SSM are tightly coupled) is highest at low temperatures.

The VT rate constants for the relaxation of the NVM are shown in Fig. B:23. The relaxation by CO_2 was scaled (see Eqs. (B:16-18)) from the experimental results for relaxation by N_2. Water is clearly the most effective relaxant of N_2. Since this relaxation competes with the VV pumping of CO_2 by excited N_2, high concentrations of H_2O should be avoided when possible. On the other hand, H_2O itself can pump CO_2 by VV collisional interactions, although the pumping is less efficient. Clearly the H_2O concentration plays an important role in CO_2 laser kinetics, particularly in the lower temperature range.

The only measured VT rate constant for the relaxation of the WBM is that due to other H_2O molecules. The result is plotted in Fig. B:24. However, the data points (Fig. 10 in Ref.25) separate into two groups which have such a large spread that even the sign of the slope at 500°K is uncertain. The values themselves should not be trusted outside the temperature range of 300 to 600°K. The other rate constants have been estimated by scaling, and by arbitrarily reducing the peak values to provide consistency with the abnormally rapid deactivation by H_2O itself. This procedure can yield only order-of-magnitude estimates at best, and is employed as a matter of necessity until better experimental values are available. In any event, the low concentration of H_2O in laser mixtures reduces the importance of accurate rate constants for H_2O deactivation processes.

TABLE B.1

VT Rate Constant Parameters for $k_i^{(\alpha)}$.

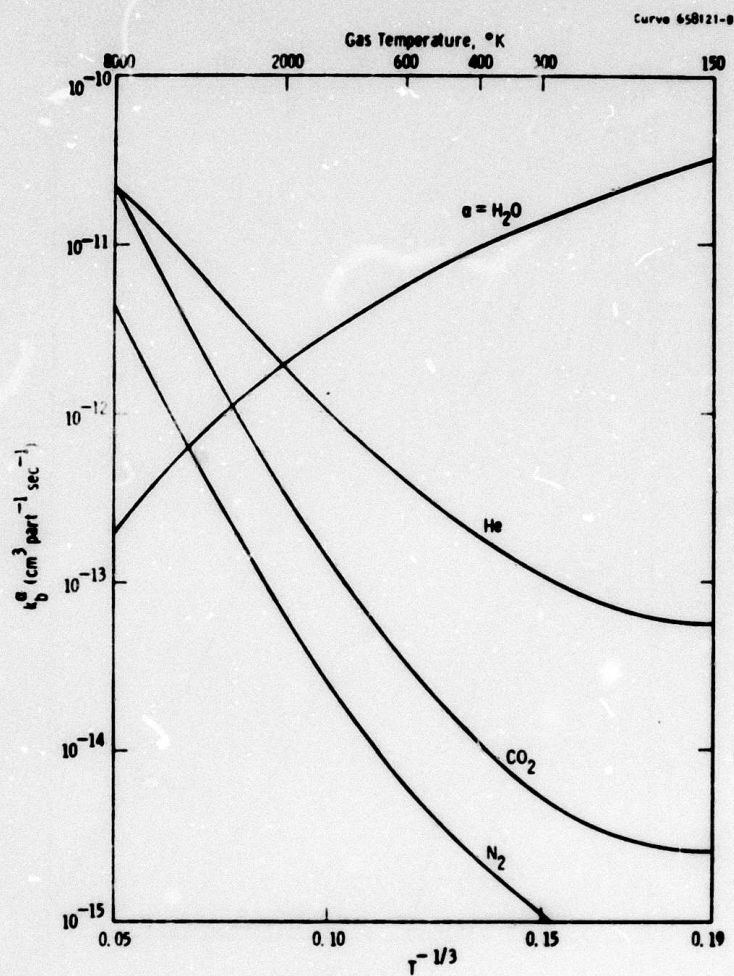| i	α	A'	B'	C'	D'	Source*
b	CO_2	4.99 (-05)	191	348	480	TB
	N_2	9.68 (-06)	192	358	480	TB
	He	2.67 (-06)	121	149	480	TB
	H_2O	7.93 (-12)	- 58	-267	480	TB
n	CO_2	1.09 (-03)	276	- 42	1677	ES
	N_2	8.03 (-04)	254	-646	1677	TB
	He	4.44 (-07)	116	-350	1677	TB
	H_2O	6.56 (-05)	123	-386	1677	TB
w	CO_2	1.24 (-19)	-308	-1446	1147	ES
	N_2	1.19 (-17)	-315	-1856	1147	ES
	He	5.18 (-18)	-240	-1111	1147	ES
	H_2O	7.59 (-15)	-268	-1468	1147	TB

*TB = Taylor and Bitterman[25]

ES = Estimated

Fig. B-22 The VT relaxation rate constants for the CO_2 bending mode.
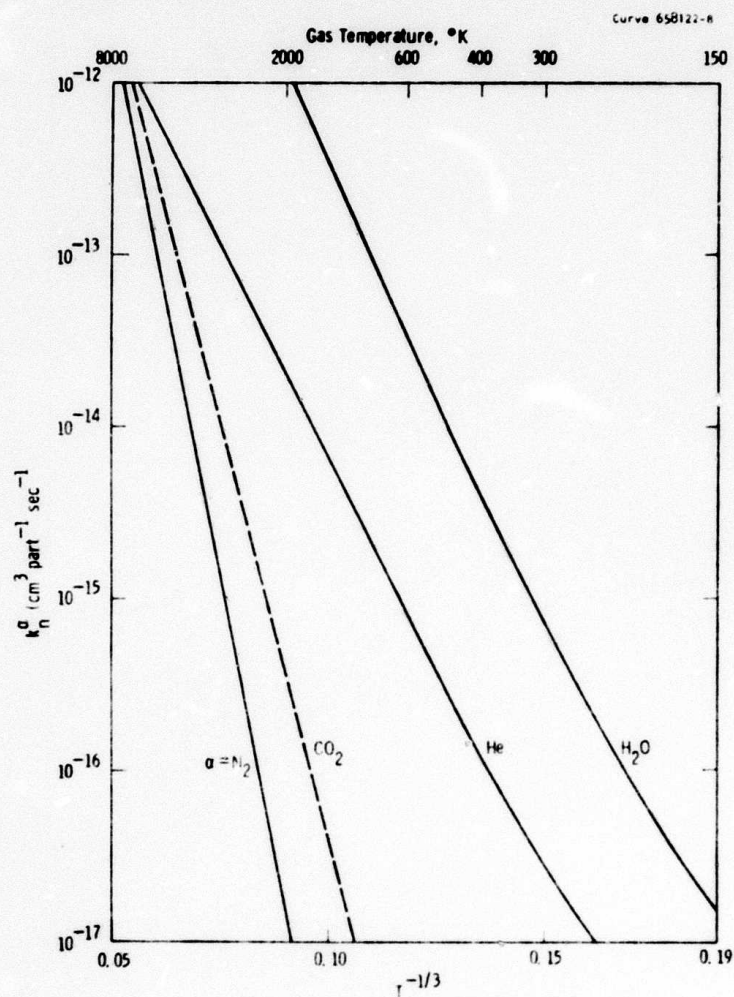
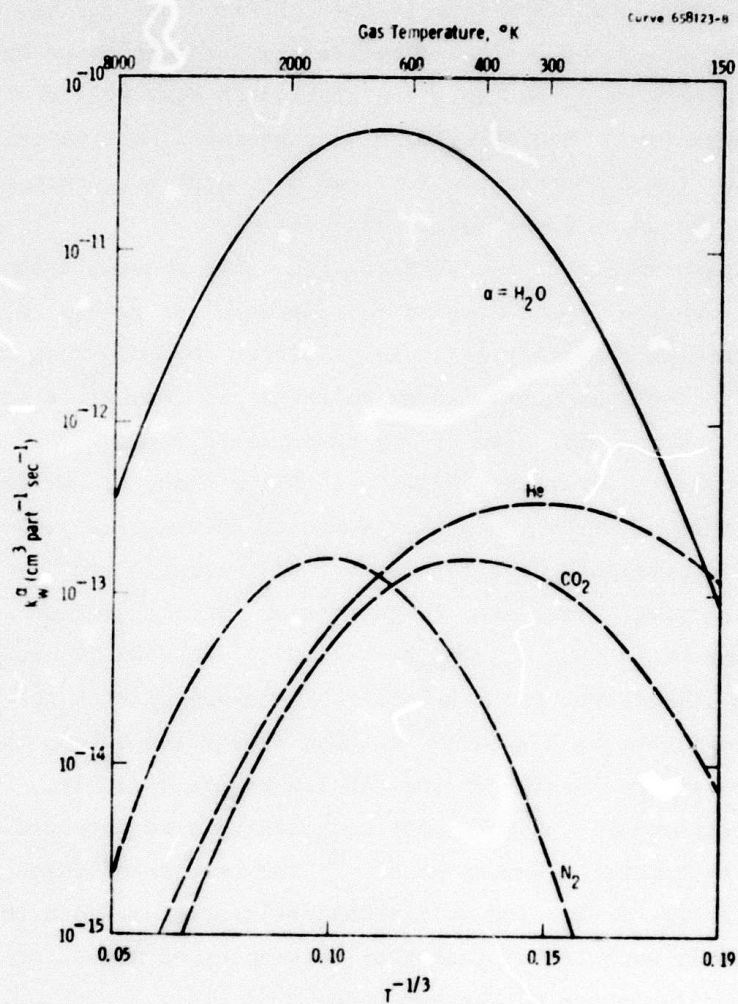Fig. B:23 The VT relaxation rate constants for the N_2 vibrational mode.

106

Fig. B.24 The VT relaxation rate constants for the H_2O bending mode.

Taylor and Bitterman[25] have also compiled the best set of experimental measurements for VV rate constants. The relevant VV rate constant parameters are given in Table B.2. Unfortunately, the VV rate constant in which helium is the collision partner has not been measured, but it can be estimated by scaling the results of MacDonald[33] for argon. These rate constants are plotted in Fig. B:25 where the anomalous behavior of H_2O is evident once again. The high values of H_2O indicate that the H_2O concentration should be kept low since it efficiently depopulates the upper laser level.

Measurements of the VV relaxation rate constants between the SSM and BM have been the source of considerable controversy since implied rates of emptying the lower laser level differ by more than an order of magnitude.[22] The values implied by Bulthuis and Ponsen[34] were at 500°K which precludes the deduction of any temperature dependence. However, the main problem is that the values are thirty times slower than those deduced by Sharma[35] from the measurements of Rhodes, Kelly, and Javan.[36] More recent experiments have been easier to interpret and have verified the more rapid rate constant. In particular, Stark[37] has measured the rapid relaxation by CO_2, N_2, and He at 400°K. Although Stark gives no temperature dependence, these values can be combined with the temperature dependence measured by Bulthuis[38] for the relaxation by CO_2 (the Bulthuis measurements give values which are too low to use directly). The relaxation by H_2O is estimated by again employing Bulthius's temperature dependence with the measurement of Rosser et al.[39] The results of these estimates are shown in Fig. B:26. The collisional relaxation between the SSM and BM is obviously much faster than that between other modes, as expected from the near resonance of the two modes.

The intermolecular VV relaxation rate constants are shown in Fig. B:27. The k_{an} values are taken from Taylor and Bitterman,[25] whereas the k_{nw} values are taken from Taylor and Bitterman[25] at high temperatures and from Evans[40] at low temperatures. The values for k_{aw} are estimated by scaling k_{an} by the reduced masses only. Attempts to measure k_{bw} have been

108

TABLE B.2

VV Rate Constant Parameters for $k_{ij}^{(\alpha)}$ and k_{ij}

i	j	α	A'	B'	C'	D'	Source*
ASM	BM	CO_2	1.45 (-02)	298	830	300	TB
		N_2	5.12 (-02)	330	952	300	TB
		He	3.24 (-02)	330	952	300	ES
		H_2O	2.50 (-12)	- 48	-270	300	TB
SSM	BM	CO_2	3.26 (00)	304	974	74	ES
		N_2	1.50 (00)	304	974	74	ES
		He	1.76 (00)	304	974	74	ES
		H_2O	2.30 (00)	304	974	74	ES
ASM	NVM[+]	--	4.07 (-10)	368	115	13	TB
ASM	NVM**	--	1.19 (03)	602	2895	13	TB
ASM	WBM	--	8.00 (-04)	215	430	542	ES
BM	WBM	--	7.93 (-14)	- 58	-267	668	ES
NVM	WMB	--	9.57 (-04)	226	442	530	TB

*TB = Taylor and Bitterman[25]

 ES = Estimated

[+]Valid below 1000°K

**Valid above 1000°K

109
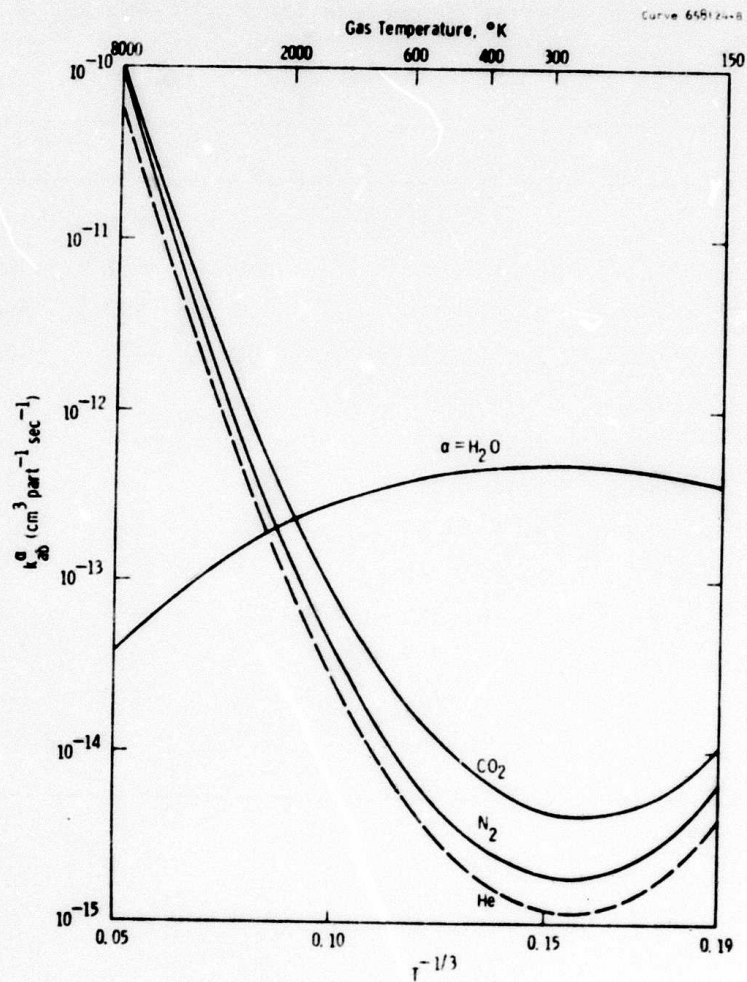
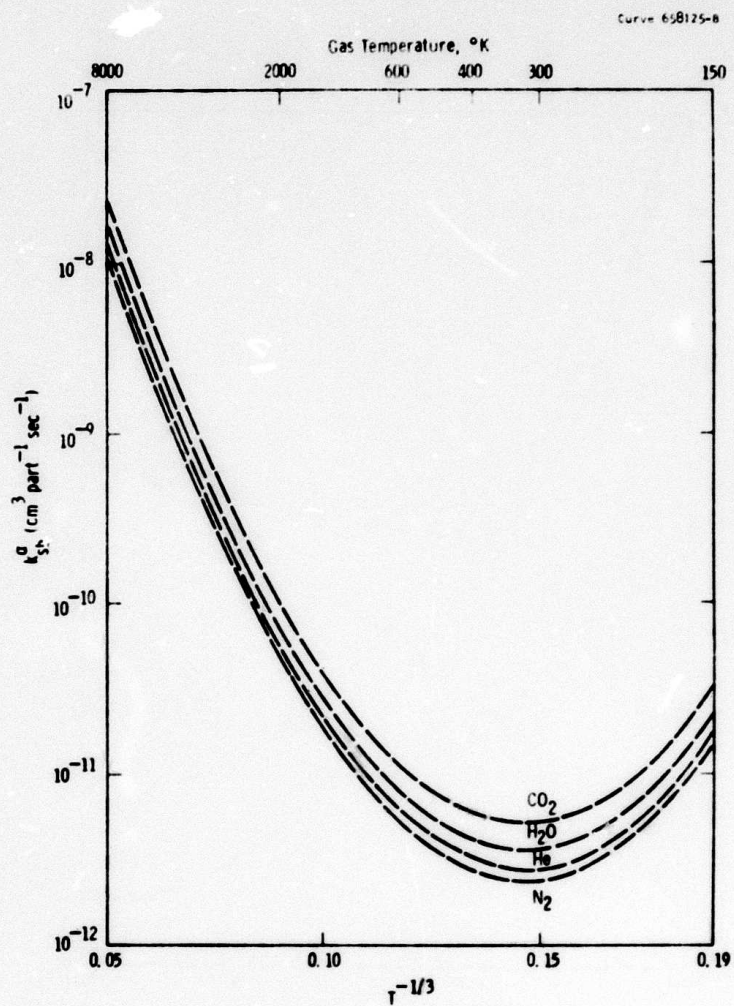Fig. B:25 The VV relaxation rate constant between the ASM and the BM.

110

Fig. B:26 The VT relaxation rate constants between the
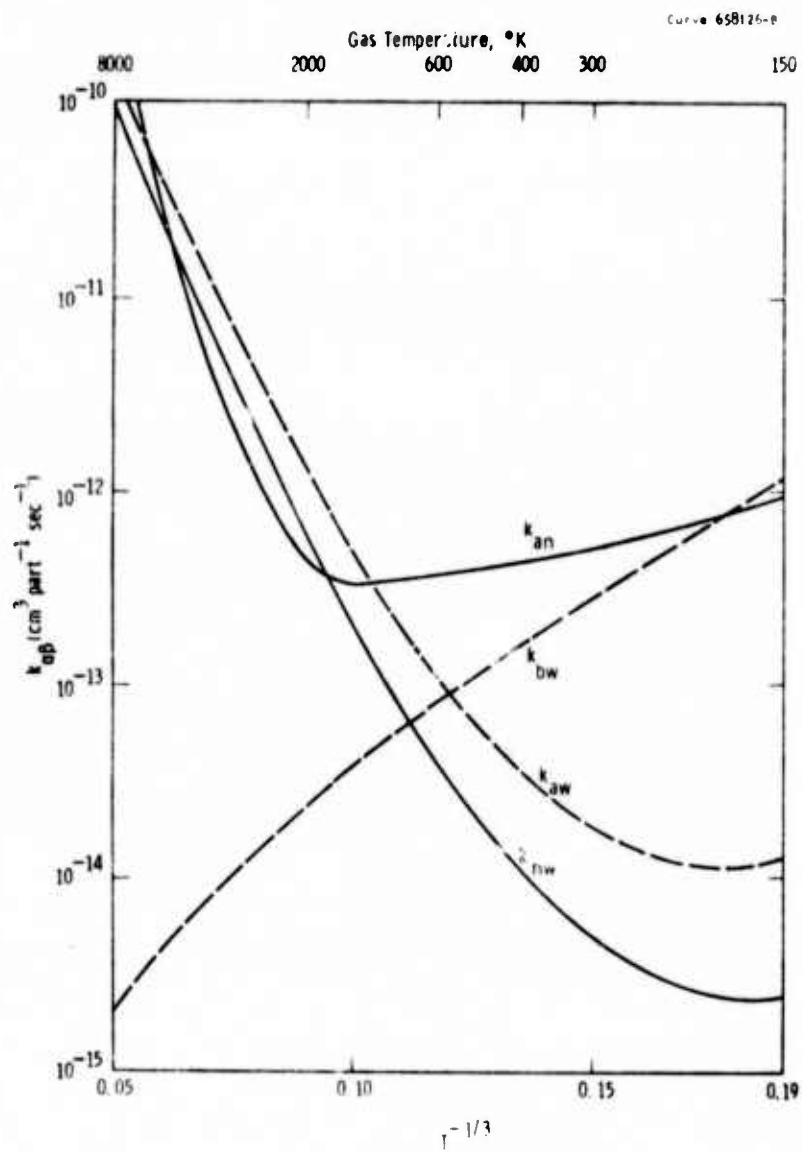   SSM and the BM.

111

Fig. B:27 Intermolecular VV relaxation rate constants.

unsuccessful, probably because this process is masked by the $k_b^{(w)}$ VT process; k_{bw} was arbitrarily assumed to be 0.01 $k_b^{(w)}$. The results in Fig. B:27 indicate that water is desirable at low temperatures but undesirable at high temperatures, and that nitrogen pumps the carbon dioxide more efficiently at low and high temperatures than it does at intermediate temperatures.

The results of this section clearly show that much experimental work remains to be done in the determination of VT and VV rate constants. Data is especially lacking on all interactions which involve water. This deficiency is unfortunate because the temperature dependence of water rates is known to be anomalous and the rates abnormally high, and hence unscalable with present theoretical models. Moreover, small concentrations of water are known to have significant effects upon the behavior of CO_2 laser devices.

APPENDIX C

ELECTRICAL EXCITATION

The electrical pumping rates are easily determined from Fig. 3:3. The total electrical power density into the discharge is given by the product of the discharge current density j and the electric field E across the discharge as measured experimentally.[41] The electrical power density entering the α vibrational mode is given by

$$W_\alpha = \gamma_\alpha jE \qquad (C:19)$$

where γ_α is the fraction of electrical power density which enters the α vibrational mode (plotted as a percentage in Fig. 3:3). The transition rate U_α into a particular mode is given by the power density input W_α, divided by the energy level spacing $k'\theta_\alpha$ and the number of α molecules per unit volume traveling in the flow direction:

$$U_\alpha = W_\alpha / k'\theta_\alpha N_\alpha \qquad (C:20)$$

evaluated at the location x. This expression is the electrical pumping term contained in the basic rate Eqs. (3:1-6), and is valid provided that (1) the change in the discharge parameters as the gas flows downstream occurs at a slower rate than the electron-neutral inelastic collision rates, (2) at any given downstream location the discharge is spatially uniform in the plane defined by line of sights between the mirrors and between the electrodes, i.e., the plane perpendicular to the direction of flow, and (3) all molecules are in the ground state of internal energy.[22] These conditions are satisfied in most CO_2 lasers.

114

A quantity of interest related to the electrical excitation is the maximum extractable stored energy density in the laser, which is defined in joule cm^{-3} as

$$E_s = (\frac{\nu_o}{\nu_a}) E_a + (\frac{\nu_o}{\nu_n}) E_n \tag{C:21}$$

$$E_\alpha = N_\alpha k' \theta_\alpha \tag{C:22}$$

where θ_α is the characteristic temperature of the α mode, E_a and E_n are the characteristic energy densities for the CO_2 asymmetric mode and the N_2 vibrational mode respectively, and the ν's are the appropriate frequencies. This definition is realistic if the equilibration of the set of rotational levels belonging to a given vibrational level is instantaneous—usually a good approximation. Within this approximation, all the rotational levels associated with a vibrational level participate in a given vibrational-rotational transition.[24] Equation (3:21) can be expressed in terms of the Boltzmann factors as

$$E_s = h'c\bar{\nu}_o \left[\frac{a}{1-a} N_c + \frac{n}{1-n} N_n\right] \tag{C:23}$$

where $\bar{\nu}_o$ is the wave number of the laser radiation. This expression is the total energy density stored in CO_2 asymmetric stretch mode and in the N_2 vibrational mode which can be extracted at 10.6 μm, assuming one photon for each vibrational quantum.

Stored energy densities in CO_2 lasers are very high and explain why they are so efficient and have such high output powers. However, stored energy is only half the story—it is worthless if it cannot be depleted by stimulated emission. This fact explains why it is difficult to optimize laser operation—a change in operating parameters may increase the stored energy density but decrease the stimulated emission depletion of that energy, or vice versa.

115

APPENDIX D

GAS HEATING

It is well known[42] that the kinetic temperature of the gas is important in molecular lasers. The collisional rates change as the gas temperature varies and as shown in Appendix B these rate changes can be very large. Furthermore, the flow velocity and gas density depend directly on the gas temperature. It is therefore imperative to determine the kinetic gas temperature.

Equation (3:6) is derived by applying the ideal gas low to the specific heat equation at constant pressure.[43] The left-hand side gives the heat energy per unit volume absorbed by the gas and is determined by the specific heats of the gas components, each component α weighted by its molar density:

$$f_\alpha = N_\alpha / N_o \qquad (D:24)$$

The specific heats of the gas components at constant pressure are given by[44]

$$C_h = 20.79$$

$$C_c = 29.11$$

$$C_n = 29.11 \qquad (D:25)$$

$$C_w = 33.26$$

in joules $\deg^{-1}$ mole^{-1}. These values are determined from the full excitation of the translational and rotational degrees of freedom of the molecule with no excitation of the vibrational degrees of freedom.[45] This is an excellent approximation in the gas temperature range encountered in CO_2 gas lasers.

116

The specific heats at constant pressure are certainly the values to use for the COFFEE laser, and are probably the best values for long pulse lasers where the gas has time to expand, and for high energy lasers where the rapid electrical heating of the gas causes a rapid expansion.[46] However, for very short pulses the gas does not have time to expand and the specific heats at constant volume should be used.[23]

As discussed above, the left-hand side of Eq. (3:6) describes the distribution of heat energy into the heat content of the molecules. The molecular kinetic energy is described by the gas temperature. The right-hand side describes the sources and sinks of the heating. There are three major sources of heating: energy defect heating from VV collisional transitions, gas heating from VT collisional transitions, and direct heating from the gas discharge. All three sources are included in the present model. However, heat sinks such as cold walls are not included. The latter approximation is valid as long as the flow velocity is not so low that thermal diffusion to the enclosure walls becomes important.

The energy defect heating terms from VV collisional transitions are given on the right-hand side of the first three lines of Eq. (3:6). The gas heating terms from VT collisional transitions are given on the fourth line of Eq. (3:6). In a typical COFFEE laser discharge VV heating is less than 10% of the total heating whereas VT heating is over 80% of the total heating (see Fig. 3:12 and 3:13).

The electrical energy density available to the gas is jE where the electric field E and current density j are measured quantities. However, not all of the electrical energy is available to heat the gas directly--a good portion of the electrical energy excites molecular vibrations rather than increasing the translational energy of the molecules. The vibrational excitation energy must therefore be deducted from the total electrical energy. Some of this vibrational excitation energy will eventually heat the gas through the VV and VT relaxation processes which have already been included. In the last line of Eq. (3:6),

117

the first term (without the factor F_e) is the electrical energy density available to the gas and the $E_\alpha U_\alpha$ terms enclosed in parentheses deduct the electrical energy density expended in vibrational excitation rather than in gas heating.

The factor F_e is the fraction of the electrical energy density which is not lost to the system through the electronic excitation of the CO_2 and N_2 molecules which then relax by photon emission, rather than by relaxing through collisions which heat the gas. Since not all electronically excited CO_2 and N_2 molecules relax by photon emission, the factor F_e can be written as

$$F_e = 1 - (1-\zeta)\gamma_e \qquad (D:26)$$

where γ_e is the fraction of the electrical energy which excites the gas into electronic levels (see Fig. 3:3) and ζ is the fraction of this excitation energy which heats the gas directly. The factor ζ is called the electronic heating factor, and $1-\zeta$ gives the fraction of the electronic excitation energy which escapes the laser system by high energy photon emission. Since the electronic heating factor is not included in other laser kinetic models, it will be examined in detail.

The electrical energy supplied to a $CO_2:N_2:He$ laser mixture is divided among elastic and rotational processes, vibrational and electronic level excitations, and ionization. The exact division depends on the relative concentrations of the gases and the operating values of E/N. For example, in a 1:7:20 laser mixture at an E/N value of 2×10^{-16} V-cm^2 (see Fig. 3:3), 83% of the electrical energy is deposited into the CO_2 00^01 level and the lowest eight vibrational levels of N_2, and the remaining 17% goes into elastic losses, rotational excitation, and the excitation of the CO_2 bending and symmetric stretch vibrations.[47] There is only 5% of the energy in electronic excitation or ionization.

At higher values of E/N significant percentages of the electrical energy will excite the CO_2 and N_2 electronically. As shown in Fig. 3:3, this percentage is near zero for $E/N = 1.0 \times 10^{-16}$ V-cm^2 but rises rapidly to 82% near 10^{-15} V-cm^2. For CO_2 lasers which operate at E/N values below 2.0×10^{-16} V-cm^2, it is clear from Fig. 3:3 that electronic excitation can be neglected and previous laser kinetics models are quite applicable

118

in this range, which includes most CO_2 lasers. Non-flowing, self-sustained 1:7:20 pulsed discharges normally operate at 3.0×10^{-16} V-cm^2 where electronic excitation cannot be neglected, whereas the COFFEE laser operates around 2.0×10^{-16} V-cm^2 where the electronic excitation is quite small. Thus the electronic heating factor cannot be neglected in pulsed self-ustained discharges but is relatively unimportant in the COFFEE laser. For this reason an accurate value of the electronic heating factor is not necessary and the empirical values of 0.40 will be taken since this value works so well for self-sustained discharge pulsed CO_2 lasers.[15]

The gas temperature as determined from these equations specifies the collisional relaxation rates as shown in Appendix B. In addition to these rates the gas temperature determines the gas flow velocity and number densities from the following equations:

$$v = (T/T_o)(v)_o \qquad\qquad (D:27)$$

$$N_\alpha = (T_o/T)(N_\alpha)_o \qquad\qquad (D:28)$$

where the o subscripts denote the value at the entrance to the laser cavity, i.e., at $x = 0$. These expressions indicate an important difference between constant pressure and constant volume solutions of the basic rate Eqs. (3:1-3:7). In the constant volume case the gas flow and number densities are constants whereas in the constant pressure case the basic rate equations must be updated by Eqs. (D:27-28) after each successful numerical integration. The COFFEE laser calculations assume that the pressure is constant.

APPENDIX E

STIMULATED EMISSION

The interaction between 10.6 μm radiation and excited CO_2 molecules leads to stimulated emission and absorption between the 00^01 and 10^00 levels. Stimulated transitions between higher lying levels are also permitted in the perfect simple harmonic oscillator approximation. However, these higher levels are sparsely populated at the temperatures of interest, and the anharmonicities actually present in the CO_2 molecule shift the wavelengths of these transitions into regions of low overlap between the linewidths. Thus only transitions between the 00^01 and 10^00 levels need be considered. Population changes due to photon-stimulated transitions between two vibrational-rotational levels are given by the relationships

$$\dot{n}_{\gamma J'} = n_{\gamma J} S_{12}^{\gamma J} - n_{\gamma J'} S_{21}^{\gamma J'} \qquad (E.29)$$

and

$$\dot{n}_{\gamma J} = -n_{\gamma J} S_{12}^{\gamma J} + n_{\gamma J'} S_{21}^{\gamma J'}$$

where $S_{12}^{\gamma J}$ and $S_{21}^{\gamma J'}$ are the stimulated absorption and emission transition rates respectively, J and J' are rotational quantum numbers of the lower and upper states respectively, and γ denotes either the P or R vibrational-rotational branch. In the case of CO_2 the zero spins of the identical nuclei exclude all odd values of J and all even values of J'. Thus

$$J' = J - 1 \text{ for } \gamma = P$$

$$J' = J + 1 \text{ for } \gamma = R \qquad (E.30)$$

are the only allowed rotational transitions between the 00^01 and 10^00 vibrational levels. Due to the changes in population required by Eq. (E:29) the ASM will lose $k'\theta_a$ joules and the SSM will gain $\kappa'\theta_s$ joules of energy for each photon emitted.

The population densities of the upper and lower laser levels can be written in terms of the Boltzmann factors as

$$n_{\gamma J'} = \beta_{J'}\, a(1-a)(1-s)(1-b)^2\, N_c$$

$$\tag{E:31}$$

$$n_{\gamma J} = \beta_J\, s(1-a)(1-s)(1-b)^2\, N_c$$

where β_J is the fraction of molecules in the Jth rotational level. This fraction[48] is given by

$$\beta_J = 2(2J+1)(\theta_r/T)e^{-J(J+1)\theta_r/T} \tag{E:32}$$

whenever the gas temperature is much greater than the characteristic rotational temperature θ_r, which is certainly valid for CO_2. The factor of 2 is the nuclear spin symmetry number.[49] Although the characteristic rotational temperature for the upper state is lower than the value for the lower state, the difference is only 0.8% and can be neglected.[49]

The stimulated emission and absorption transition rates are related by the principle of detailed balance:

$$S_{12}^{PJ} = \left[\frac{2J-1}{2J+1}\right] S_{21}^{PJ'}$$

$$\tag{E:33}$$

$$S_{12}^{RJ} = \left[\frac{2J+3}{2J+1}\right] S_{21}^{RJ}$$

where Eqs. (E:30) have also been used. By combining Eq. (E:29) through (E:33) and arranging the terms in the proper format, the stimulated transitions in the basic rate equations are obtained,[22] where

$$\Gamma = \Gamma_{\gamma J} \; S_{21}^{\gamma J} \qquad\qquad (E:34)$$

$$\Gamma_{PJ} = \left(a - e^{-2J\,\theta_r/T} \; s \right) Q_{PJ}$$

$$\Gamma_{RJ} = \left(a - e^{2(J+1)\theta_r/\Gamma} \; s \right) Q_{RJ} \qquad (E:35)$$

$$Q_{PJ} = (2J-1)(2\theta_r/T) \; e^{-J(J-1)\theta_r/T}$$

$$\qquad\qquad (E:36)$$

$$Q_{RJ} = (2J+3)(2\theta_r/T) \; e^{-(J+2)(J+1)\theta_r/T}$$

These equations show the difference between the P and R rotational branches.

The stimulated emission rates are given by the product of the photon flux f_{γ} at the appropriate wavelength and the stimulated cross section, $\sigma_{\gamma J}$:

$$S_{21}^{\gamma J} = f_{\gamma J} \; \sigma_{\gamma J} \qquad\qquad (E:37)$$

$$f_{\gamma J} = I_{\gamma J}/h' c\bar{\nu}_o \qquad\qquad (E:38)$$

$$\sigma_{\gamma J} = \phi_{\gamma J}^{(0)} A_{21}/8\pi c\bar{\nu}_o^{\;2} \qquad\qquad (E:39)$$

where $I_{\gamma J}$ is the total light intensity at the laser wave number $\bar{\nu}_o$, $\phi_{\gamma J}^{(0)}$ is the line shape factor at line center, and A_{21} is the spontaneous transition rate between the upper and lower laser levels. The spontaneous transition rate and laser wave number are very slightly dependent[50] on the value of γJ, and are .201 sec^{-1} and 944.287 cm^{-1} respectively for the common P(20) transition.[51-52]

At low pressures the line shape is inhomogeneous due to Doppler broadening and the normalized line shape function is Gaussian. The value at line center is given by the relationships

$$\phi_G^{(0)} = \sqrt{4 \ln 2/\pi} \; B_G^{-1} \qquad\qquad (E:40)$$

$$B_G = \bar{\nu}_o \sqrt{8kT(\ln 2)/MWc^2} \qquad\qquad (E:41)$$

where B_G is the Gaussian full linewidth at half maximum in wave numbers and M is the CO_2 mass in amu. At higher pressures the line is homogeneously broadened by collisions in addition to the homogeneous natural broadening of the transition. In this case the value of the line shape factor at line center is

$$\phi_L^{(0)} = (2/\pi) \; B_{\gamma J}^{-1} \qquad\qquad (E:42)$$

where $B_{\gamma J}$ is the Lorentzian full linewidth at half maximum:

$$B_{\gamma J} = \frac{1}{\pi c \tau_{\gamma J}} + \frac{1}{\pi c} \sum_{\substack{i= \\ c,n,h,w}} \sigma_{CO_2,i} \; N_i \sqrt{\frac{8kT/W}{\pi \mu_{CO_2,i}}} \qquad (E:43)$$

The reduced masses $\mu_{CO_2,i}$ are easily calculated, and the optical broadening cross sections $\sigma_{CO_2,i}$ have been measured[52] as 130, 91 and 25 $\overset{\circ}{A}^2$ for collisions with CO_2, N_2 and He respectively. The optical broadening cross section due to H_2O has not been measured, but can be estimated as being approximately the same as the 73 $\overset{\circ}{A}^2$ measured for Ne, which has a similar molecular weight.[53] The natural lifetime in Eq. (E:43) is determined by the sum of all transition rates which involve the upper or lower laser level:[54]

$$\frac{1}{\tau_{\gamma J}} = A_{21} + S_{21}^{\gamma J} + S_{12}^{\gamma J} + R_{an} \left(\frac{1+2An}{1-n}\right) + R_{aw} \left(\frac{1+2Fw}{1-w}\right) + R_{sb} \left(\frac{1+2Bb^2}{1-b}\right)$$

$$+ R_{ab} \left[\frac{1+2Cb^3}{(1-b)^2}\right] \qquad\qquad (E:44)$$

This expression does not include electrical excitation which is usually negligible relative to the sum of the other transition rates.

Although it is well known that either Gaussian or Lorentzian line shapes apply in most practical cases, it is desirable in computational models to have an expression, however approximate, which can be used throughout the entire pressure range. The Voigt profile[55] accurately describes the combination of Gaussian and Lorentzian profiles but is too cumbersome for the present purposes. Instead, one may employ a simple approximation which preserves normalization conditions and matches both Gaussian and Lorentzian expressions at the appropriate limits:

$$\phi_{\gamma J} = (\phi_C B_G^2 + \phi_L B_L^2)/(B_G^2 + B_L^2) \qquad\qquad (E:45)$$

which reduces at line center to

$$\phi_{\gamma J}^{(0)} = \left[\sqrt{\frac{4\ln 2}{\pi}} B_G + \frac{2}{\pi} B_{\gamma J}\right] / (B_G^2 + B_{\gamma J}^2) \qquad\qquad (E:46)$$

The expression can be used at all pressures and temperature to yield the stimulated emission transition rates, and to provide a good estimate of the Voigt profile over the transition range between pure Gaussian and Lorentzian line shapes.

APPENDIX F

RADIATION INTENSITY

The total radiation intensity $I_{\gamma J}$ which triggers stimulated emission is the sum of the spontaneous radiation intensity $I_{\gamma J}^{u}$ not collimated by the cavity mirrors, and the spontaneous plus stimulated radiation intensity $I_{\gamma J}'$ which is collimated by the cavity mirrors. That is,

$$I_{\gamma J} = I_{\gamma J}' + I_{\gamma J}^{u} \qquad (F:47)$$

The uncollimated light intensity is given by

$$I_{\gamma J}^{u} = K P_{\gamma J} \qquad K = V_u/A_{\cdot,} \qquad (F:48)$$

where K is the power density-to-light intensity conversion factor and $P_{\gamma J}$ is the spontaneous emission power density within the gas:

$$P_{\gamma J} = h'c\bar{\nu}_o A_{21} Q_{\gamma J} (1-s)(1-b)^2 a(1-a)N_c \qquad (F:49)$$

The geometric parameters used in constants such as K are easily derivable from the resonator cavity design, and are given in Appendix A.

The collimated light intensity is determined by Eq. (3:7) which is basically the equation for defining gain. The last term is the contribution from a constant input radiation intensity I_o to be amplified by the laser. This term is zero if the laser is used as an oscillator rather than an amplifier. The light intensity-to-power density conversion factor is given by

$$K'' = A_o/V_c \qquad (F:50)$$

where the geometric parameters are given in Appendix A.

125

Of the light generated by spontaneous emission only a very small fraction possesses the proper spatial mode for amplification by the resonator cavity. [56] This fraction is given by

$$\epsilon_{\gamma J} = \psi_{\gamma J}^{(0)} / (8\pi \bar{\nu}_o^2 V_c) \qquad (F:51)$$

Thus, the second term on the right side of Eq. (3:7) is the spontaneous emission which triggers the coherent stimulated emission amplified by the laser cavity.

The first term on the right-hand side of Eq. (3:7) is the net gain of the medium, given by the difference between the total gain $\alpha_{\gamma J}$ and the average cavity loss per unit length, $\beta_{\gamma J}$. The latter term is

$$\beta_{\gamma J} = b_{\gamma J} - \ln[(1-a_{1\gamma J})(1-a_{2\gamma J})(1-\tau_{1\gamma J})(1-\tau_{2\gamma J})]/2L \qquad (F:52)$$

where $b_{\gamma J}$ is the scattering loss per unit length inside the gas, L is the distance between the mirrors, $\tau_{i\gamma J}$ is the transmissivity and $a_{i\gamma J}$ is the total loss per bounce at the ith mirror. The mirror loss term includes scattering, absorption, and diffraction. The total gain is obtained from the product of the stimulated emission cross section and population inversion:

$$\alpha_{\gamma J} = \sigma_{\gamma J} \Delta n_{\gamma J} \qquad (F:53)$$

The population inversion is determined in Appendix E as

$$\Delta n_{\gamma J} = N_c \Gamma_{\gamma J} (1-s)(1-b)^2(1-a) \qquad (F:54)$$

This expression is positive for an amplifying medium (although the gain may not be above threshold) and negative for an absorbing medium.

Although the net gain determines the radiation intensity within the laser medium, the useful output is that light intensity transmitted by the end mirrors, namely

$$I_{out} = \frac{1}{2} \sum_{\gamma J} (\tau_{1\gamma J} + \tau_{2\gamma J}) I'_{\gamma J} \tag{F:55}$$

This is the final result desired from any laser kinetic model. The factor $\frac{1}{2}$ is necessary because at each mirror only half of the cavity flux is traveling toward the mirror.